Soliton interactions and bound states

David Foster

A Thesis presented for the degree of
Doctor of Philosophy

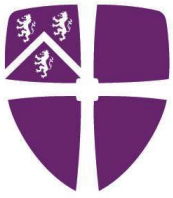

Centre for Particle Theory
Department of Mathematical Sciences
Durham University
UK

October 21, 2010

Dedicated to

My parents and Katie.

Soliton interactions and bound states

David Foster

Submitted for the degree of Doctor of Philosophy

October 21, 2010

Abstract

The research presented in this thesis is concerned with soliton interactions and bound states. We consider a non-topological soliton in $(1 + 1)$ dimensions and topological models in $(2 + 1)$ and $(3 + 1)$ dimensions.

In chapter 2 we consider Qballs, which are non-topological solitons, in $(1 + 1)$ dimensions. Here we note the semi-integrable behaviour of small-charge Qballs. This leads us to propose a possible mechanism to explain the two distinct oscillatory modes of a Qball breather. In chapter 3 we are interested in the $(2+1)$-dimensional baby-skyrme model, which is a lower-dimensional analogue of the Skyrme theory. We discover new chain-like bound-state minimum-energy solutions. We then analyse whether these solutions are the minimum-energy solutions on a cylinder, and then finally on the torus. In chapter 4 we discuss a new $(2 + 1)$-dimensional model containing a baby skyrmion coupled to a vector meson. This is an analogue of the $(3 + 1)$-dimensional Skyrme theory containing a vector meson. We use this lower-dimensional analogue to numerically justify the use of a rational map ansatz in the analysis of the $(3 + 1)$-dimensional skyrmion. Also we analytically prove why the baby-skyrme model, and the model containing a baby skyrmion stabilised by a vector meson, have very similar solutions. Chapter 5 discusses Hopf solitons. Instead of being lumps, Hopf solitons actually resemble loops of string. Their charge is related to the string's knotting and twisting. In this chapter we include an extra

mass term in the Skyrme-Faddeev theory; this gives solitons which are exponentially localised. We then explore the infinite-coupling case, which gives compact Hopfions. This chapter is part of an ongoing investigation. All of the original research results presented are my own results. This thesis is based on three publications [1–3]. Papers [1, 2] were written in collaboration, and I present my own results. Paper [3] is purely my own research.

Declaration

The work in this thesis is based on research carried out at the Centre for Particle Theory, the Department of Mathematical Sciences, Durham University, England. No part of this thesis has been submitted elsewhere for any other degree or qualification and it is all my own work unless referenced to the contrary in the text.

Acknowledgements

I would like to thank Prof. W. Zakrzewski and Dr. B. Piette for their guidance and encouragement.

Dr. D. Harland has been invaluable as a collaborator and for his help.

I would especially like to thank Prof. P.M. Sutcliffe for being an outstanding supervisor.

Contents

List of Figures

List of Tables

Chapter 1

Solitons in field theory.

There is a small class of nonlinear equations which have solitary, localized, lump-like solutions. These solutions are often referred to as soliton solutions. More precisely a soliton solution is a finite-energy solution of a nonlinear partial differential equation. Solitons tend to be stabilised by a conserved charge associated with the physical field theory. A soliton's energy density tends to be smooth and localized in a finite region of space. The nonlinear partial differential equation needs two main terms: a sharpening nonlinear term and a dispersive term. Soliton solutions capture the nonlinear nature of the relevant theory, making soliton dynamics a very rich and interesting topic. Nonlinear field theories, which possess soliton solutions as part of their energy spectrum, are of great interest in modern particle physics. Like in solitons can repel and scatter off each other; they can also attract to form bound states. The analysis of solitons necessitates a large expanse of mathematical techniques often amalgamating analytical, geometrical and sophisticated numerical techniques. These numerical techniques are usually very computationally intensive but, due to the recent advancements in computing power, we can now dynamically solve these highly nonlinear equations to a good order of accuracy.

Soliton solutions are not just interesting mathematically. They also occur in a wide

variety of field theories. Solitons are predicted to exist in cosmology as Q-balls [4]; in particle physics as magnetic monopoles [5] and in condensed matter physics as baby skyrmions [6], plus in many more field theories. Solitons are also found in superconductivity, fluid dynamics and nonlinear optics.

There are two main classes of soliton solutions, integrable solitons and numerically derived solitons. Integrable solitons tend to occur in 1-dimensional theories which have an infinite number of conserved charges. Also their governing differential equations can usually be expressed as a compatibility condition of an over determined linear system. This allows their form and dynamics to be analytically derived. The nonlinear differential equations, derived from larger dimensional and non-integrable theories, can only been solved using powerful numerical relaxation techniques.

1.1 Skyrme theory.

With the aim to outline two fundamental principals of solitons in field theory, namely Derrick's theorem and the finite energy criteria, it is efficient to work with an example model. The model of choice is the Skyrme theory [7] which is a $(3+1)$-dimensional nonlinear theory of pions. Skyrme's motivation was to create a field theory where the field's topological degree is identified with the baryon number. Hence the Skyrme theory is a topological field theory of the atomic nucleus. One of the most incredible parts of this theory is Skyrme's vision. He realised that under quantisation, of the rotationally symmetric skyrmion, it is possible to gain spin $1/2$ fermion states from the bosonic theory. The Skyrme theory can also be derived as a low energy effective field theory of Quantum Chromodynamics, in the large colour limit [8]. It is also found that at low energies the pion fields are the major contributors. We can best describe this theory using the Lagrangian

$$L = \int_{\mathbb{R}^3} \left(-\frac{1}{2}\mathrm{Tr}(R_\mu R^\mu) + \frac{1}{16}\mathrm{Tr}([R_\mu, R_\nu][R^\mu, R^\nu]) \right) d^3x, \tag{1.1.1}$$

where R_μ is the $su(2)$-valued current, $R_\nu = (\partial_\nu U)U^\dagger$, in terms of the $SU(2)$-valued field $U(\boldsymbol{x}, t)$. This theory is comprised of two main terms. It has a sigma term, $\mathrm{Tr}(R_\mu R^\mu)$, which is quadratic in derivatives and inherits its name from the $O(n)$-sigma model. The second term, $\mathrm{Tr}([R_\mu, R_\nu][R^\mu, R^\nu])$, is quartic in derivatives and refereed to as the Skyrme term. The field, $U(\boldsymbol{x}, t)$, is a solution of the associated highly nonlinear partial differential equation known in field theory as the Euler-Lagrange equation,

$$\partial_\mu \left(R^\mu + \frac{1}{4}[R^\nu, [R_\nu, R^\mu]] \right) = 0. \tag{1.1.2}$$

This highly nonlinear partial differential equation has no non-trivial known closed form solution. Skyrmion solutions have only been derived using substantial numerical techniques. Over the years there has been extensive research of the skyrmion model [9–19]. Multiple charged skyrmions have been found [9], where for topological charge greater than two the charge density is found to be a shell-like polyhedron. One of the major recent advances has been the discovery of the rational map ansatz [20]. This ansatz was motivated by the observed similarities between skyrmion and monopole solutions. It takes advantage of the Platonic structure of skyrmions, so the Skyrme field can be re-expressed as a radial profile function and an angular dependence. The angular dependence is specified by a rational map between Riemann spheres. This results in a significant reduction in complexity of the numerical minimisation scheme, to calculating a profile function and a rational map. Also the ansatz can be used to create approximate skyrmions, which have energy close to the global minimum. This is a very useful tool for speeding up 3-dimensional energy minimisation schemes, by removing a computationally expensive scattering process.

The polyhedral skyrmions, produced in the above pure Skyrme model, do not correlate with the existing understanding of the atomic nucleus; especially for larger mass numbers. Primarily it contradicts with the roughly homogeneous density of the

nucleus core. An extra term can be included in the Skyrme theory, known as a mass term, which gives rise to a pion tree level mass. This extra term causes the Skyrme model to favour a modular structure. They are composed of essentially unperturbed topological charge four skyrmions. This is in agreement with the alpha particle picture of the atomic nucleus. It also replicates some of the necessary symmetries needed to reproduce nuclear energy spectra under quantisation. Particularly for nuclei like ^{8}Be and ^{12}C which are known to be composed of alpha particles.
The Skyrme model gives the possibility of a more fundamental and mathematical understanding of the atomic nucleus. Especially when compared to more traditional phenomenological approaches.

1.2 Derrick's theorem.

One of the most fundamental criteria for solitons in field theory is a scaling argument known as Derrick's theory [21]. This theory is applicable to static theories defined in flat space. It states that under a spatial rescaling if there is no stationary point of the energy, as a function of the scaling, then there are no non-vacuum solutions of the associated Euler-Lagrange equation. This is best shown using the Skyrme theory example which has the associated static energy functional

$$E = \int_{\mathbb{R}^3} \left(-\frac{1}{2}\mathrm{Tr}(R_i R_i) - \frac{1}{16}\mathrm{Tr}([R_i, R_j][R_i, R_j]) \right) d^3x. \tag{1.2.1}$$

Under the spatial rescaling $x \mapsto \lambda x$ we can re-express the energy as

$$E(\lambda) = \frac{1}{\lambda} E_\sigma + \lambda E_S,$$

where E_σ is the contribution of energy from the sigma term and E_S is the contribution from the Skyrme term. In 3-dimensions the two terms scale in opposite ways. Therefore, any soliton solution will neither expand nor contract. This shows why

the Skyrme theory needs the extra quartic derivative Skyrme term. A static solution of the Euler-Lagrange equation, for a given topological charge, will have a minimum energy when $\lambda = 1$. Therefore, for the energy to be a stationary point the sigma term and the Skyrme term must contribute equally to the total energy, $E_\sigma = E_S$.

1.3 Finite energy criteria.

Physically sensible soliton solutions must have finite energy. In flat space this requires the field to smoothly attain the theories vacuum value at spatial infinity. This is needed so the theories energy density vanishes at infinity, which is required for the total energy to be finite. Due to the field having the same boundary value, at $r = \infty$, this gives rise to a one point compactification of the flat space $\mathbb{R}^n \cup \{\infty\}$. This is topologically equivalent to the surface S^n. Also if the field takes its value in a sphere, S^m, the field will then belong to the homotopy class $\pi_n(S^m)$. Therefore the field could have an associated topological degree, which in this thesis we refer to as the topological charge.

For finite energy, in the Skyrme example, we choose $U(|\boldsymbol{x}| \to \infty) = 1_2$. This allows a one-point compactification of the domain, $\mathbb{R}^3 \cup \{\infty\} \sim S^3$. Also, it is well known that the group manifold of $SU(2)$ is S^3. Hence the Skyrme field at fixed time is a map

$$U(\boldsymbol{x}, t) : S^3 \to S^3. \tag{1.3.1}$$

Therefore the field, $U(\boldsymbol{x}, t)$, can be assigned an element of to the homotopy class $\pi_3(S^3) = \mathbb{Z}$. So there is an integer topological degree associated with the map $U(\boldsymbol{x}, t)$. For skyrmions we refer to the topological degree as the topological charge B. A point worth noting is that a field configuration with topological charge B_1 cannot be smoothly deformed into a field configuration with topological charge $B_2 \neq B_1$. This shows that for differing topological charges the solution spaces are not smoothly connected and hence topological charge is always conserved.

There are also non-topological soliton models which are stabilised by the conservation of a non-integer Noether charge. Qballs for example, are stabilised by a conserved $U(1)$ Noether charge. Again, in this non-topological case, the Noether charge is conserved under evolution of the Euler Lagrange equation.

1.4 Elementary concepts.

All of the theories discussed in this thesis originate from classical physical field theories. Therefore they can all be defined by an action which has associated Noether currents. The action also has an associated energy functional, which is manifested as an invariance of time transformation. This means all of the theories are physically interesting. Also we shall be using natural units, where the speed of light $c \equiv 1$. We shall now define some of the notation used in the remainder of this thesis. We denote a point in the smooth n-dimensional physical space M as $x_i \in M$, where the Latin index indicates spacial coordinates $(x_1, ..., x_n)$. We shall also define the space-time coordinates as $x_\mu \in M \times \mathbb{R}$. Where $x_0 = t$ and the Greek indices resemble spacial dimensions plus one time dimension $(x_0, ..., x_n)$. All the physical space-times are Minkowski with metric $g_{\mu\nu} = \text{diag}(1, -1, ...)$ and we make use of the Einstein summation convention throughout. Also we shall denote the complex conjugate of the field ψ as $\bar{\psi}$.

This concludes the thesis introduction. We start to present the research in chapter 2. Chapter 2 is concerned with a non-topological soliton theory known as the Qball model. This is a $(1 + 1)$-dimensional theory where we studied the dynamics of Qball-Qball collisions. This led to the realisation that small charge Qballs start to display semi-integrable behaviour during interactions. We also analyse the structure

of Qball breathers. We explain the nature of the two oscillatory modes observed in the breather spectrum.

In chapter 3 we are interested in the $(2+1)$-dimensional baby skyrmion model. This is a lower dimensional analogue of the $(3+1)$-dimensional Skyrme theory. We propose that the static minimum energy bound solutions are chains of baby skyrmions. We perform the numerical analysis on $\mathbb{R}^2$, then on the cylinder $\mathbb{R} \times S^1$ to find the infinite chain energy per unit charge. Then, finally, on $\mathbb{T}^2$ in order to find the minimum energy solution which fills the whole space.

In chapter 4 we introduce a new baby skyrmion model which does not have a Skyrme term. It is instead stabilised, under Derricks theorem [21], by a coupling to an extra vector field. This is a lower dimensional analogue of the $(3+1)$-dimensional skyrmion theory coupled to a vector meson. We numerically find that the baby skyrmion model and the baby skyrmion coupled to a vector meson model produce very similar solutions. We then verify this proof using an analytical approximation.

Chapter 5 is concerned with $(3+1)$-dimensional Hopf solitons. This model is related to the baby skyrmion model due to the Lagrangians being very similar. We include a mass term in this model. This gives exponentially localised Hopfions.

All of these chapters have an introduction, methodology, discussion and conclusion. All the presented results are my own research.

Chapter 2

Qballs, interaction and integrability.

2.1 Introduction.

Most solitons are stabilized by topological effects, but there are also class of soliton that are not stabilised by topology. Non-topological solitons tend to be stabilised by an associated conserved current. In 1985 Sidney Coleman [4] conjectured a new type of non-topological soliton, the Qball. Coleman showed that Qballs can occur in theories that have a time dependent field, with an internal phase, and a continuous unbroken global symmetry. This time dependent internal phase gives rise to a stabilising conserved Noether charge, Q. It is mainly due to this non-topological charge not being quantised in any manner that complicates Qball-Qball interactions. This causes a myriad of possible charge related dynamics ranging from charge exchange to Qball fission.

Qball solutions can arise in any theory with a scalar potential $U(|\phi|)$, which has a global minimum and an unbroken global $U(1)$ symmetry.

It was shown in 1997 by Alexander Kusenko that Qballs can occur in the minimal supersymmetric standard model [22]. This gives rise to Qballs that are linked to the conservation of baryon and lepton number. Also, there are an assortment of physical processes which could have created Qballs during the early universe [23]; hence the possibility that primordial Qballs could still exist.

The possibility that primordial Qballs could still exist means Qballs could be a potential dark matter candidate [24]. This is our main motivation for studying Qballs. We were motivated to try and determine the dynamics of Qball-Qball interactions. This could then be used to understand if primordial Qballs could still exist today, or would they simply annihilate each other and vaporise?

To answer this question we first carried out numerical simulations of Qball collisions. We observed the phenomena of charge exchange and Qballs radiating when in excited states. We then realised that the complex sine-Gordon soliton is also another type of Qball solution. Following this we noticed that in the small Qball limit the standard Qball model converged with the complex sine-Gordon model. Therefore, the non-integrable model will start to present semi-integrable behaviour in the small charge limit. This was one of the main turning points in our research and led to the understanding of small Qball collisions. This semi-integrable behaviour was also fundamental to understanding the behaviour of perturbed Qballs.

This led us to formulate a new truncated Qball model, which attempts to link the complex sine-Gordon model and the usual Qball models. From our observations of Qball collisions, we have come to the conclusion that Qballs interact less as they lose charge. They begin to behave in a semi-integrable way in the small charge limit. This chapter is interested in Qballs in $(1+1)$-dimensions, but they can also occur in higher dimensions [25, 26].

2.2 Qballs in $(1+1)$-dimensions.

One of the simplest models with Qball solutions is a $(1+1)$-dimensional complex scalar field theory with a global $U(1)$ symmetry. Described by the Lagrangian density

$$\mathcal{L} = \partial_\mu \phi \partial^\mu \bar{\phi} - U(|\phi|). \tag{2.2.1}$$

The unbroken $U(1)$ symmetry gives rise to a conserved Noether current q_μ,

$$q_\mu = i\phi\partial_\mu\bar{\phi} - i\bar{\phi}\partial_\mu\phi. \tag{2.2.2}$$

The continuity equation, $\partial_\mu q^\mu = 0$, shows that this theory has a conserved global charge

$$Q = \int_{-\infty}^{\infty} i\left(\dot{\bar{\phi}}\phi - \dot{\phi}\bar{\phi}\right) dx = \int_{-\infty}^{\infty} q(x)dx, \tag{2.2.3}$$

where we have set $q_0(x) = q(x)$. To find the minimum energy solution of (2.2.1), for a fixed charge Q, we introduce the Lagrangian multiplier, ω, into the Hamiltonian $\mathcal{H}_Q$ as

$$\mathcal{H}_Q = H + \omega(Q - \int_{-\infty}^{\infty} q dx),$$

where H is the stationary energy. This gives the minimum energy for a fixed Q. Then using the $U(1)$ symmetry we can re-express the field, ϕ, as an angle $\theta \in \mathbb{R}$ and a profile function $f(x) \in \mathbb{R}$ as

$$\phi = e^{i\theta(t)} f(x,t). \tag{2.2.4}$$

This gives

$$\mathcal{H}_Q = \omega Q + \int_{-\infty}^{\infty} \dot{f}^2 + f'^2 + f^2(\dot{\theta} - \omega)^2 - U_\omega \;\; dx \tag{2.2.5}$$

where $U_\omega = \omega^2 f^2 - U$. We can minimise (2.2.5) by setting the positive definite term $\dot{\theta} - \omega = 0$ and $\dot{f} = 0$. These are the only terms we can set to zero not to give a

trivial $f(x)$. Doing this gives the standard stationary Q-Ball form

$$\phi = f(x)e^{i\omega t}. \tag{2.2.6}$$

This describes a Qball centred at the origin of a coordinate system with a constant internal frequency, $\omega > 0$, and a real profile function. The profile function, f, is a solution of the ordinary differential equation

$$f'' = -\omega^2 f + \frac{1}{2}\frac{dU}{df} = -\frac{1}{2}\frac{dU_\omega}{df}, \tag{2.2.7}$$

with the boundary conditions $f'(0) = 0$ and $f(\infty) = 0$. On multiplication of (2.2.7) by $f'(x)$ and then integration over x we gain the first order differential equation

$$f'^2 = -\omega^2 f + U.$$

Using the boundary conditions on f we gain a constraint on the potential,

$$U(f_0) = \omega^2 f_0^2, \tag{2.2.8}$$

where $f_0 \equiv f(0)$. Substituting (2.2.6) into (2.2.3) gives the Noether charge $Q(\omega)$,

$$Q(\omega) = 2\omega \int_{-\infty}^{\infty} f^2 dx.$$

2.3 Qball existence, ω bounds.

To find a constraint on the form of the potential U we can interpret (2.2.7) as a mechanical Newtonian system. We interpret (2.2.7) as a unit mass particle moving in potential $-U_\omega/2$ at time x and position f. The method is to find a solution for a stationary particle which starts at $f'(0) = 0$ and comes to rest at $f = 0$, after infinite 'time' x. This imposes the condition that $f \to 0$ as $x \to \infty$. This restricts

the possible form of the effective potential U_ω in two ways.

1. Undershooting. If the particles starts at a point f, where $-U_\omega < 0$, then it cannot reach $f(0)$ (2.2.8). This is due to the initial position having less effective potential energy than the final position. Hence

$$\max(-U_\omega) \geqslant 0 \Leftrightarrow \min\left(\frac{U}{f^2}\right) = {\omega_-}^2 < \omega^2. \tag{2.3.1}$$

2. Overshooting. For the particle to come to rest at $f = 0$, $-U_\omega$ must be concave about $f = 0$. hence

$$-\frac{d^2U}{df^2}\Big|_{f=0} > 0 \Leftrightarrow \frac{1}{2}\frac{d^2U}{df^2}\Big|_{f=0} = {\omega_+}^2 = m^2 > \omega^2. \tag{2.3.2}$$

Combining (2.3.1) and (2.3.2) we find the static single Qball existence bound

$$\omega_- \leqslant \omega < \omega_+. \tag{2.3.3}$$

Note that there is also a solution for $\omega < 0$. This solution is termed as the anti-Qball solution and has $Q < 0$.

2.4 Qball stability.

For a Qball solution, of fixed charge Q, to be stable to all perturbations it must be the global minimum energy solution. For this to be the case a solution must fit the two criteria below.

2.4.1 Absolute stability.

For small perturbations about the vacuum, $\phi = 0 + \epsilon(x, t)$, if we only include first order in ϵ the theory becomes linear. If we then place the theory on a large section

L [27] the equation of motion then becomes the Klein Gordon equation. This has the fundamental particle plane wave solution

$$\epsilon(x,t) = Ne^{-i(kx-\omega_k t)}, \tag{2.4.1}$$

where k is the wave number, $\omega_k = \sqrt{m^2+k^2}$ and $N = \sqrt{Q/2\omega_k L}$ is a charge normalising factor. In the low momentum infra-red limit this plane wave solution has total energy

$$\mathcal{H}_{particle} = Qm. \tag{2.4.2}$$

This is interpreted as the energy of Q free particles of mass m. So, for a soliton solution to be stable, the Qball must have less energy than Q single bosons of rest mass m. This criterion is known as the absolute stability criterion,

$$\mathcal{H}_Q < \mathcal{H}_{particle} \;\Rightarrow\; \frac{\mathcal{H}_Q}{Q} < m. \tag{2.4.3}$$

2.4.2 Fusion stability.

For a Qball to be stable against decay into smaller Qballs the total energy per-unit charge must be convex. This is implied because a Qballs energy per-unit charge must be lower than the energy per-unit charge for two Qballs. So a charge Q_T Qball must have less energy per-unit charge than two Qballs of charges $Q_1 = (1-\epsilon)Q_T$ and $Q_2 = \epsilon Q_T$, where $\epsilon \in [\frac{1}{2}, 1]$. Therefore

$$\mathcal{H}(Q_T) \leqslant \mathcal{H}(Q_1) + \mathcal{H}(Q_2). \tag{2.4.4}$$

If we then create a line segment $h(Q)$, between $\mathcal{H}(Q_1)$ and $\mathcal{H}(Q_T)$, which is parametrised as $Q = (1-\lambda)Q_1 + \lambda Q_2$ where $\lambda \in [0, 1]$ as

$$h(Q) = (1-\lambda)\mathcal{H}(Q_1) + \lambda\mathcal{H}(Q_T). \tag{2.4.5}$$

Then at $Q = Q_2$ $\lambda = (2\epsilon - 1)\epsilon^{-1}$, so

$$h(Q_2) = -\frac{\epsilon - 1}{\epsilon}\mathcal{H}(Q_1) + \frac{2\epsilon - 1}{\epsilon}\mathcal{H}(Q_T) < \mathcal{H}(Q_2) \quad \forall \quad \epsilon \in [\frac{1}{2}, 1]. \tag{2.4.6}$$

In the second relation of (2.4.6) we have used (2.4.4) and that the two terms involving ϵ are always positive and less than one. This simple analysis shows that the function $\mathcal{H}(Q)$ must be convex over the interval $Q \in [Q_1, Q_T]$. One of the characteristics of a convex function leads to a strong constraint which is

$$\frac{d^2\mathcal{H}_Q}{dQ^2} < 0. \tag{2.4.7}$$

If we then re-express (2.2.5) as

$$\mathcal{H}_Q = \omega Q + S_\omega, \tag{2.4.8}$$

with the Euclidean action

$$S_\omega = \int_{-\infty}^{\infty} \left(f'^2 - U_\omega \right) dx. \tag{2.4.9}$$

Then taking the charge derivative, for fixed S_ω, of (2.4.8) we get one of the well known Legendre relations [28]

$$\left. \frac{d\mathcal{H}_Q}{dQ} \right|_{S_\omega} = \omega. \tag{2.4.10}$$

We can use this relation with (2.4.7) to give the classical stability criterion,

$$\frac{dQ}{d\omega} \leq 0. \tag{2.4.11}$$

2.5 General Qball profile function.

For a stationary solution the momentum density

$$p(x) = \dot{\phi}\bar{\phi}' + \dot{\bar{\phi}}\phi' = 0. \tag{2.5.1}$$

By the continuity equation, $\partial_t p = \partial_x j$, the momentum density has an associated current

$$j = -|\dot{\phi}|^2 - |\phi'|^2 + U(|\phi|) = 0. \tag{2.5.2}$$

Substituting (2.2.6) into (2.5.2) gives the first order ordinary differential equation

$$f'^2 = -\omega^2 f^2 + U(f). \tag{2.5.3}$$

This first order equation for f can also be found by multiplying (2.2.7) by f' and integrating over x. The above technique is of more use later. Choosing a potential that is a degree 3 polynomial in $\phi\bar{\phi}$

$$U = f^2(1 - f^2) + \beta f^6, \tag{2.5.4}$$

which we can re-write as

$$U(f) = f^2(1 - \frac{1}{2}f^2)^2 + (\beta - \frac{1}{4})f^6. \tag{2.5.5}$$

We find for $\beta > 1/4$ there is only one vacuum value which is $f = 0$, so $\omega_- = \sqrt{1 - \frac{1}{4\beta}}$. For $\beta < 1/4$ the potential is not bounded from below but $f = 0$ is still a local minima; hence there could still be Qball solutions based on this false vacuum with the lower bound $\omega_- = 0$. Also if $\beta = 1/4$ there is no longer a unique vacuum, there are two degenerate values at $f = 0$ and $f = \sqrt{2}$. Qball models with two vacua have previously been studied [28]. For all β the upper bound on ω is found to be $\omega_+ = 1$.

For arbitrary β we find that (2.5.3) has the solution

$$f = \frac{\sqrt{2}a}{\sqrt{\sqrt{1 - 4\beta a^2}\cosh(2ax) + 1}}, \tag{2.5.6}$$

where $a = \sqrt{1 - \omega^2}$. This solution has the associated Noether charge

$$Q = \frac{4\omega}{\sqrt{\beta}} \tanh^{-1}\left(\frac{1 - \sqrt{1 - 4\beta a^2}}{2a\sqrt{\beta}}\right). \tag{2.5.7}$$

On substitution of (2.5.6) and (2.5.4) into (2.2.1) we gain the static energy

$$E = \frac{4a\omega + Q(4\beta a^2 - 1)}{8\omega\beta}. \tag{2.5.8}$$

2.6 Truncated Qballs.

Setting $\beta = 0$ in the potential (2.5.4) we gain a new truncated Qball model. We shall find this truncated model is of great interest later. Stable solutions only occur when the lowest order term in the potential is quadratic in f and the highest order term is quartic in f. This can be shown for a general truncated Qball model with

the Lagrangian density

$$\mathcal{L} = \partial_\mu \phi \partial^\mu \bar{\phi} - |\phi|^2 + |\phi|^n, \tag{2.6.1}$$

where $n = 2\mathbb{Z} \geqslant 4$. Using the same procedure as above we find the first order ordinary differential equation for f

$$f'^2 = -\omega^2 f^2 + f^2 - f^n. \tag{2.6.2}$$

This is solved by

$$f = (a \operatorname{sech}(xap))^{\frac{1}{p}}, \tag{2.6.3}$$

where $p = \frac{1}{2}(n-2)$ and $a = \sqrt{1-\omega^2}$.

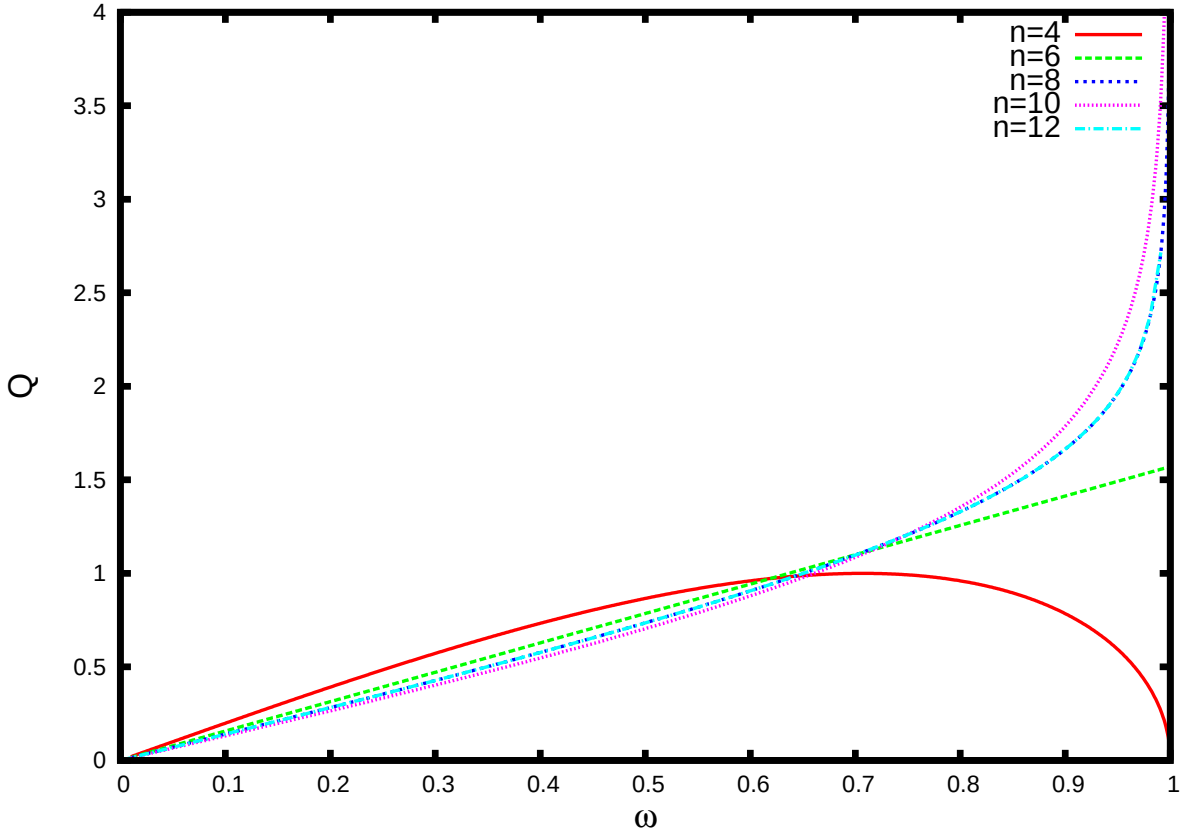

Figure 2.1: Charge as a function of ω for different truncated potentials $U = |\phi|^2 - |\phi|^n$.

If we then numerically calculate the Noether charge of (2.6.1), for different values of n, we find Figure 2.1. Figure 2.1 which shows, by the classical stability criteria

(2.4.11), that the only truncated potential which may give rise to stable Qball solutions is $n = 4$. Throughout this text we will refer to the $n = 4$ truncated model simply as the truncated model. The energy and charge of the truncated model can be found by taking the limit of (2.5.7) and (2.5.8) for $\beta \to 0$ giving

$$Q = 4\omega a, \tag{2.6.4}$$
$$E = \frac{4a}{3}(2\omega^2 + 1)$$

and

$$f(x) = a\text{sech}(ax). \tag{2.6.5}$$

The truncated model has the usual upper limit $\omega < \omega_+$ as shown for the general potential. However, the lower limit is not $\omega > 0$ for this unbounded potential. But, as shown for $n = 4$ in Figure 2.1, the derivative of Q with respect to ω becomes positive for $\omega < 1/\sqrt{2}$. Therefore, by classical stability, a Qball solution is only stable in the truncated model for

$$\frac{1}{\sqrt{2}} \leqslant \omega < 1. \tag{2.6.6}$$

2.7 Integrable complex sine-Gordon model.

A third theory of interest, which also has Qball solutions, is the complex sine-Gordon model [29–31]. This theory is described by the Lagrangian density

$$\mathcal{L} = \frac{1}{1 - \phi\bar{\phi}} \left(\partial_\mu \phi \partial^\mu \bar{\phi} - U(|\phi|) \right),$$

where $U = (1 - \bar{\phi}\phi)|\phi|^2$ giving

$$\mathcal{L} = \frac{\partial_\mu \phi \partial^\mu \bar{\phi}}{1 - \phi\bar{\phi}} - |\phi|^2. \tag{2.7.1}$$

Unlike the previous models this theory has a non-trivial denominator below the sigma term. This allows a more general choice of potential. This is because if we chose a general potential $U(|\phi|) = (1 - \bar{\phi}\phi)W(|\phi|)$, where for the complex sine-Gordon model we have $W(|\phi|) = |\phi|^2$. As long as $W(0) = 0$ then we gain the usual bound

$$\omega_+ = \frac{1}{2}\frac{d^2W}{df^2} = 1.$$

Therefore, this model yields stable solutions for $0 < \omega < 1$. Again using momentum conservation and (2.2.6) we find the first order ordinary differential equation

$$f'^2 = -\omega^2 f^2 + (1 - f^2)f^2. \tag{2.7.2}$$

(2.7.2) is the same as the first order equation describing the truncated model (2.6.2), hence they share the same solution (2.6.5). The static energy and charge associated with (2.7.1) are

$$E = 4a, \quad Q = 4\arccos\omega. \tag{2.7.3}$$

The complex sine-Gordon model has previously been shown to have Qball-type solutions [32]. The integrable nature, of the complex sine-Gordon model, does not seem to have yet been used to help understand Qball dynamics in a non-integrable system. Unlike the previous, non-integrable, models the complex sine-Gordon model has a well known multiple soliton solution [31]. We shall discuss and make use of this multi-soliton solution later.

Now that the main theories of interest have been introduced, for a more powerful and compact analysis later, we shall combine all of the above theories into one Lagrangian density

$$\mathcal{L} = \frac{\partial_\mu\phi\partial^\mu\bar{\phi}}{F(|\phi|)} - W(|\phi|). \tag{2.7.4}$$

2.8 QBall collisions.

In order to try and understand how Qballs interact we shall now discuss some numerically simulated Qball-Qball collisions in the truncated model. As initial conditions for our simulation we shall use the sum of two minimum energy solutions, located at $\pm\alpha$, gently boost towards each other with velocity $\pm v$

$$\phi = e^{i\omega_1 t} f_{\omega_1} + e^{i\omega_2 t} f_{\omega_2}.$$

Using this initial condition we then numerically evolved the relevant equations of motion. This simulation used a finite difference leap frog algorithm on a lattice of $\Delta x = 0.1$ and time step $\Delta t = 0.0001$. Below we shall discuss some of the phenomena uniquely associated with Qball-Qball collisions.

2.8.1 Charge exchange.

One of the signature phenomena of QBall-QBall interactions is the continual exchange of charge. This is when charge oscillates between two Qballs positioned next to each other, with a periodicity in time. An example of this is shown in Figure 2.2 where we placed two truncated Qballs with, $\omega_1 = 0.9$ and $\omega_2 = 0.91$, next to each other with no relative velocity; and then numerically evolved the system.

If we allow this configuration to evolve much later in time the two Qballs seem to swap position. This gives the impression that the two Qballs pass through each other. However, if we observe the fields at finite time it is apparent that two Qballs exchange charge. If we then allow the system to evolve even further we gain a field configuration that is a close match to the initial condition. Another very interesting observation which can be made from these simulations is shown in Figure 2.3. Here we have gently boosted two Qballs ($\omega_1 = 0.9, \omega_2 = 0.91$) towards each other. As they approach they begin to exchange charge and later in time the charge is totally

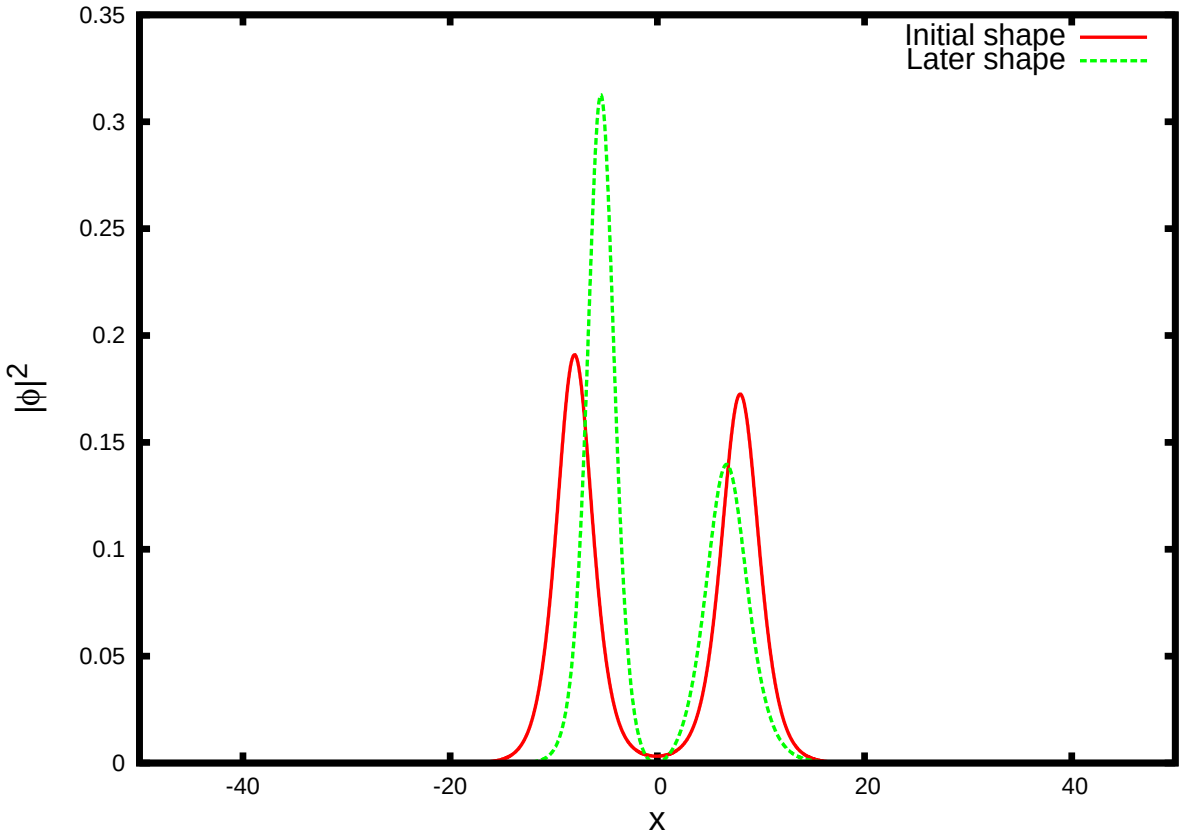

Figure 2.2: Two truncated Qballs of initial internal frequencies $\omega_1 = 0.9$ and $\omega_2 = 0.91$ exchanging charge.

exchanged. For asymptotic time this gives the impression that the Qballs have swapped over. The similarity of the two Qballs at $t = 0$ and for large t mimics the integrable behaviour of the complex sine-Gordon model. In the complex sine-Gordon model this can be analytically proven. This semi-integrable behaviour becomes more apparent in the small Qball limit. This is not surprising because as $\phi \to 0$ all the above theories converge; their Lagrangian densities become similar hence so do their equations of motion, charges and energies. Therefore we expect to see integrable characteristics in the non-integrable model.

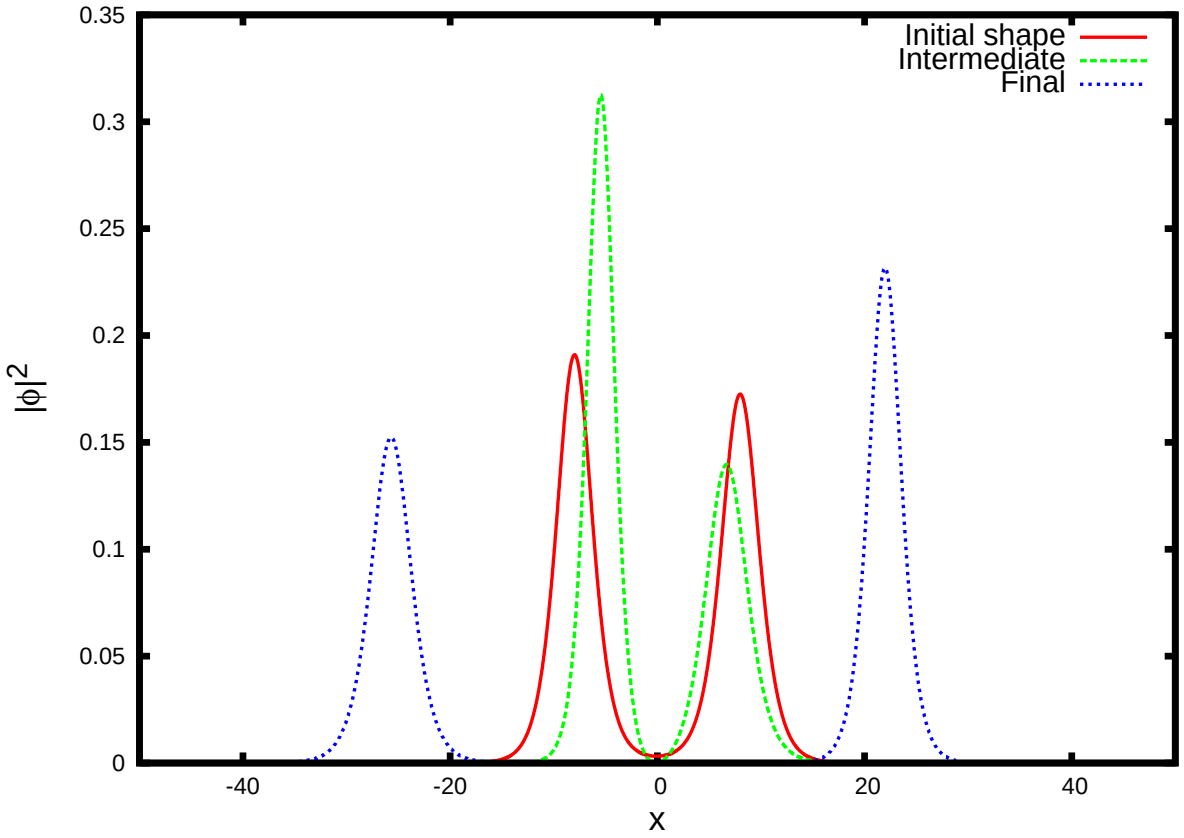

Figure 2.3: Two truncated Qballs of initial internal frequencies $\omega_1 = 0.9$ and $\omega_2 = 0.91$ exchanging charge.

2.8.2 QBall anti-QBall collisions.

Another interesting interaction is the Qball anti-Qball interaction. As stated previously an anti-Qball simply has an $\omega < 0$ and therefore negative charge. An interesting interaction occurs when, in the truncated model, we collide a Qball and an anti-Qball each with velocity $v = 0.9$. This interaction is shown in Figure 2.4. We see that the Qballs appear to pass through each other without interacting and neither of the Qballs seem to lose charge.

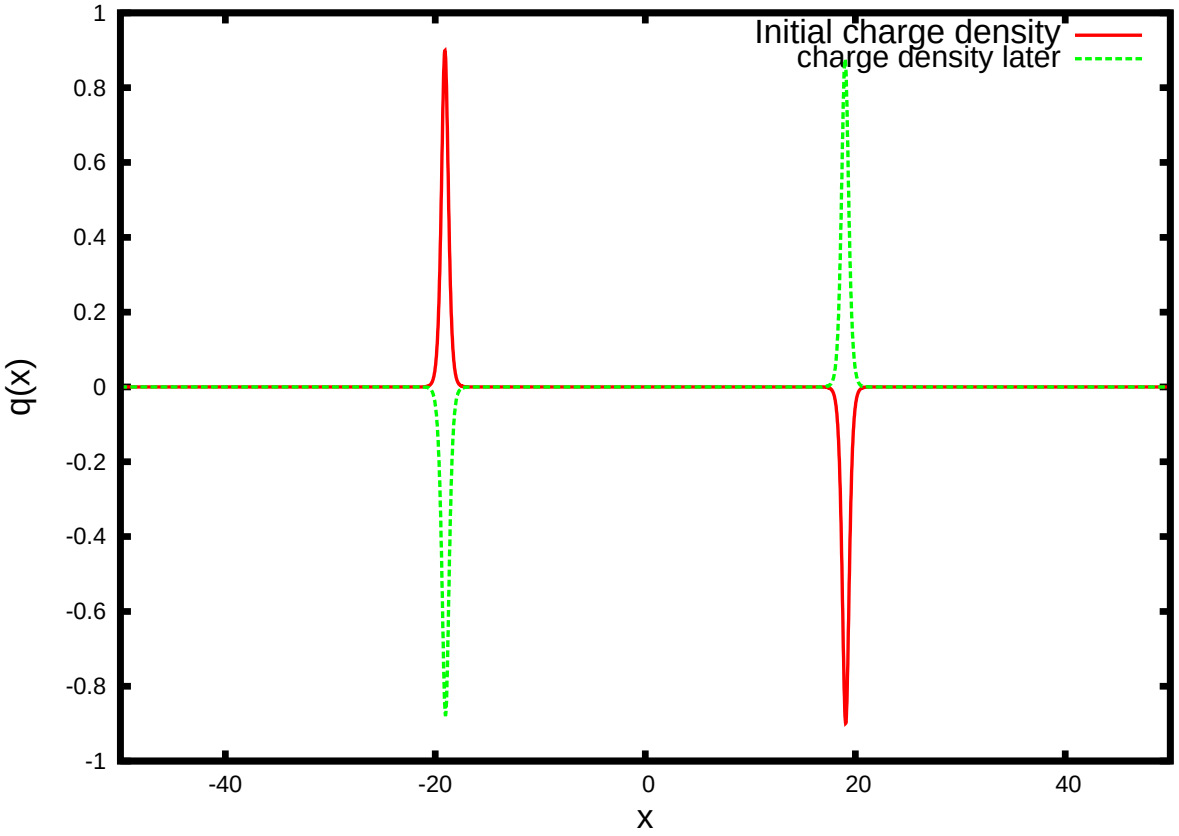

Figure 2.4: Charge density of a Qball anti-Qball with internal frequencies $\omega_1 = -\omega_2 = 0.9$ boosted towards each other at $v = 0.9$.

This effect can be attributed to the lack of time for annihilation to occur. Another interesting interaction in the truncated model is a slow, small charge, Qball anti-Qball collision. We can simulate this by boosting a Qball and an anti-Qball towards each other at $v = 0.08$, with the internal frequencies $\omega_1 = -\omega_2 = 0.998$. On first inspection we would expect total annihilation. But the convergence with the integrable model outlined above predicts minimal charge should be annihilated, leaving two similar Qballs. On simulation the latter prediction proves to be correct. Figure 2.5 shows how negligible charge has been annihilated in this non-integrable model.

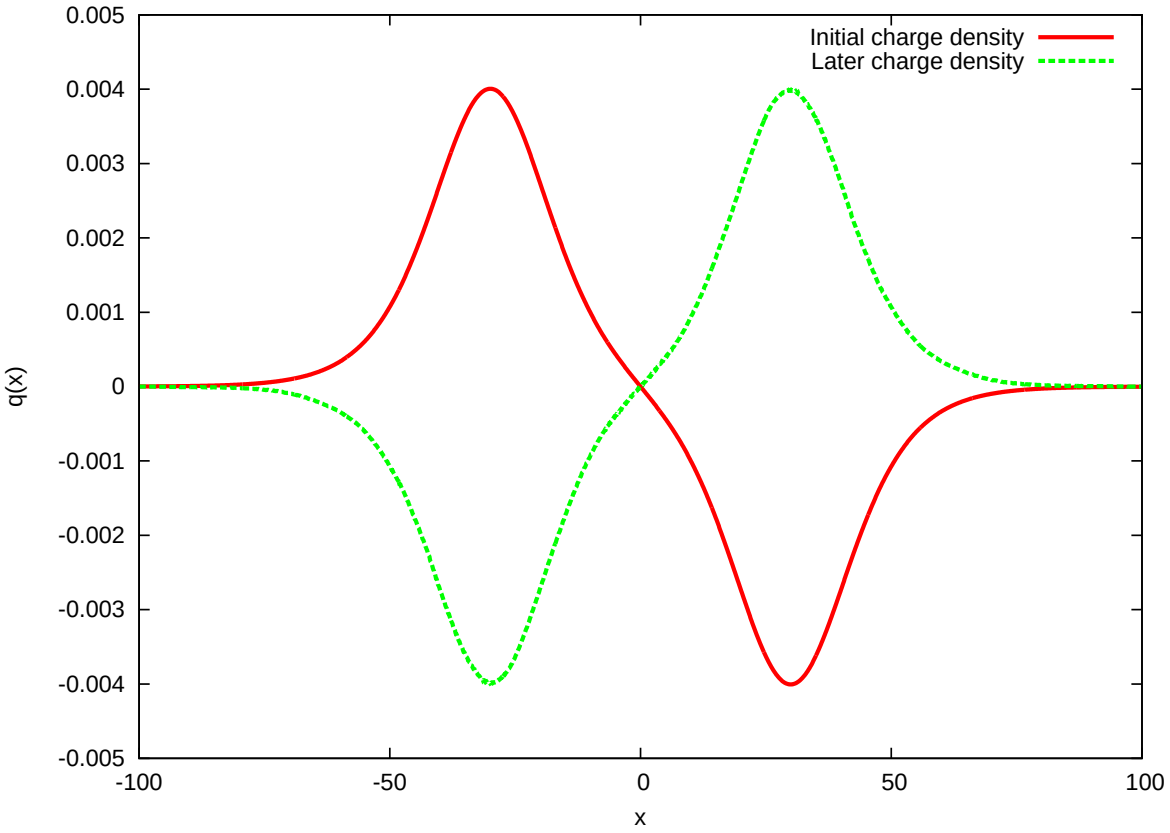

Figure 2.5: Charge density of a Qball anti-Qball collision with internal frequencies $\omega_1 = -\omega_2 = 0.998$. Each Qball was boost at $v = 0.08$, towards each other.

These interesting phenomena led us to add a Qball anti-Qball ($\omega_1 = -\omega_2 = 0.9$) pair each with zero velocity and both at $x = 0$. Simulation of this zero charge configuration is found to oscillate over a very long time as shown in Figure 2.6.

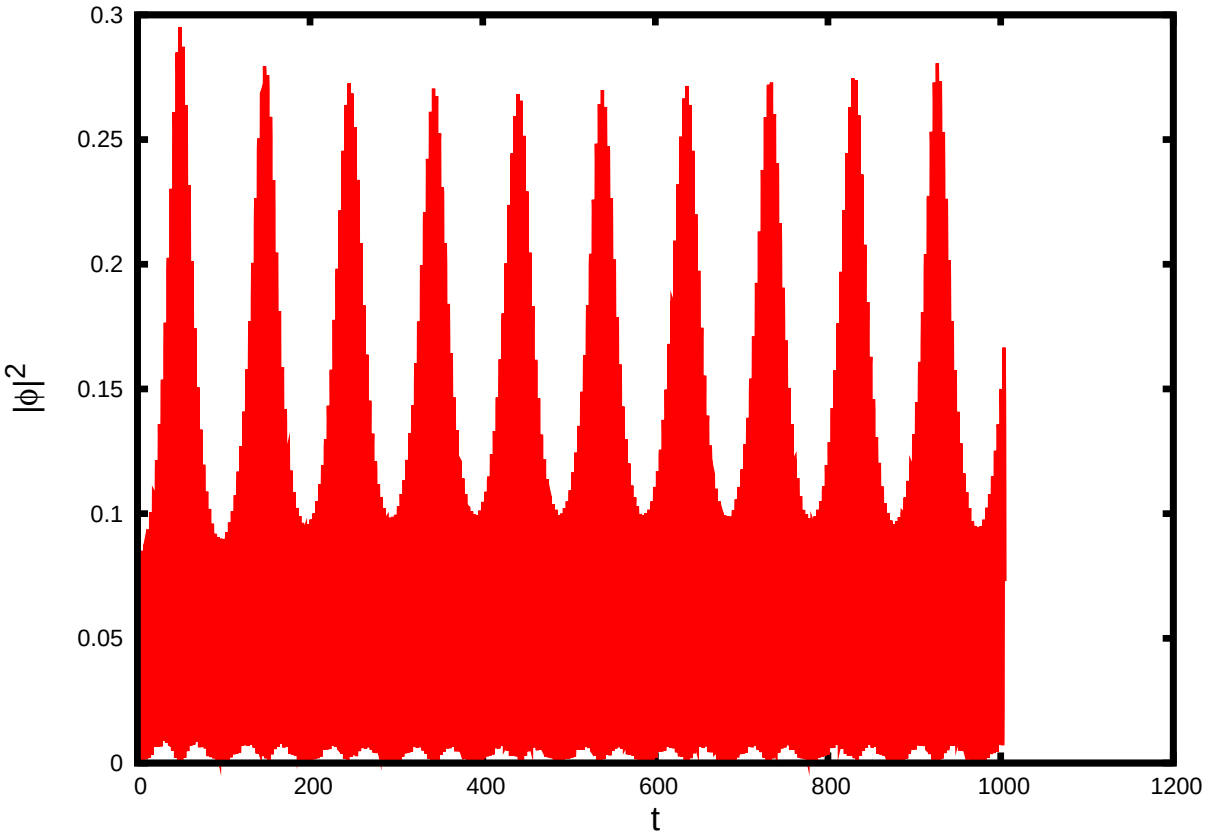

Figure 2.6: Maximum squared field value for a Qball anti-Qball system with internal frequencies $\omega_1 = -\omega_2 = 0.9$. Each Qball was placed on top of each other.

2.9 Forces between general Qballs.

For a field configuration of two well separated Qballs. The force exerted by one Qball on the other can be found by calculating the rate of change of momentum in a region containing one Qball, due to the presence of the second Qball. Using the two Qball summation ansatz

$$\phi = \phi_1 + \phi_2 = e^{i\omega_1 t} f_1 + e^{i\omega_2 t + i\theta} f_2, \tag{2.9.1}$$

where $f_1 = f(\omega_1)$ and $f_2 = f(\omega_2)$ are each centred at $\pm\alpha$ respectively with a phase difference θ. It must be noted that this ansatz does not conserve charge for varying α. But this ansatz, (2.9.1), is suitable as a well separated static approximation. We

can calculate the force, $\mathcal{F}$, between two Qballs by taking the time derivative of the momentum, P, over a large interval $[x_+, x_-]$ as

$$\mathcal{F} = \frac{dP}{dt} = \int_{x_-}^{x_+} \partial_t p \, dx. \tag{2.9.2}$$

Instead of performing this integration, (2.9.2), we can again use the continuity equation, $\partial_t p = \partial_x j^p$, giving

$$\mathcal{F} = \int_{x_-}^{x_+} \partial_x j \, dx = \left[-\frac{|\dot{\phi}|^2 - |\phi'|^2}{F(|\phi|)} + W(|\phi|) \right]_{x_-}^{x_+}. \tag{2.9.3}$$

Now using the above summation ansatz and due to the soliton tails, $|\phi| \approx 0$, at x_+, x_- we only need to keep terms up to quadratic order in ϕ. This gives

$$\begin{aligned} \mathcal{F} &= -\left[|\partial_t \phi_1|^2 + |\partial_x \phi_1|^2 - \phi_1 \bar{\phi_1} + |\partial_t \phi_2|^2 + |\partial_x \phi_2|^2 - \phi_2 \bar{\phi_2} \right]_{x_-}^{x_+} \\ &- \left[\partial_t \phi_1 \partial_t \bar{\phi_2} + \partial_x \phi_1 \partial_x \bar{\phi_2} - \phi_1 \bar{\phi_2} + \partial_t \phi_2 \partial_t \bar{\phi_1} + \partial_x \phi_2 \partial_x \bar{\phi_1} - \phi_2 \bar{\phi_1} \right]_{x_-}^{x_+}. \end{aligned} \tag{2.9.4}$$

We can simplify (2.9.4) further by using the fact that for a single Qball $j = 0$. Hence, when evaluated at $x_\pm$, the top bracket must vanish for two well separated Qballs. Re-expressing ϕ in terms of f, ω and a phase difference θ we gain an expression for the force

$$\mathcal{F} = 2\cos((\omega_2 - \omega_1)t + \theta) \left[(1 - \omega_1 \omega_2) f_1 f_2 - \partial_x f_1 \partial_x f_2 \right]_{x_-}^{x_+}. \tag{2.9.5}$$

For this expression, (2.9.5), of the force to be physically sensible we need the total force on a region containing two Qballs to be identically zero. Choosing a region $[x_+, x_-]$ which contains two Qballs each centred at $\pm\alpha$ where $|x_+|, |x_-| >> |\alpha|$. We

can the linearise the two profile forms for large $|x|$ as

$$f_1(x >> -\alpha) \sim C_{\omega_1} e^{-a_1(x+\alpha)}, \qquad (2.9.6)$$
$$f_2(x << \alpha) \sim C_{\omega_2} e^{a_2(x-\alpha)}.$$

C_{ω_i} is some positive function of ω_i that is dependent on the model. Substituting these into (2.9.5) gives,

$$\mathcal{F}[x_+, x_-] = 4C_{\omega_1}C_{\omega_2}\cos((\omega_2-\omega_1)t+\theta)(1+a_1a_2-\omega_1\omega_2)\sinh((a_2-a_1)L)\exp(-\alpha(a_1+a_2)). \qquad (2.9.7)$$

This is the total force on an interval, $[x_-, x_+] = [-L, L]$, that contains the two Qballs. We find that (2.9.7) is zero if and only if $\omega_1 = \omega_2$. Hence the above analysis only works for two Qballs with the same internal frequency ω. Therefore we are restricted to $\omega_1 = \omega_2 = \omega$. If we evaluate $\mathcal{F}$ over the interval $(L, \infty]$, where $0 < L < \alpha$, and note that due to $f(x = \infty) = 0$ there is no contribution to the force at $x = \infty$. Then on substitution of the linearised forms of f into (2.9.5) and evaluating at L we gain

$$\mathcal{F} = -4C_\omega^2 a^2 \exp(-2\alpha a)\cos\theta. \qquad (2.9.8)$$

(2.9.8) is independent of the position L and reduces to zero for infinite separation. For two Qballs with phase $\theta = 0$ it is known that there is an attractive force between them [2]. This is shown in (2.9.8) where $\mathcal{F} < 0$, hence attractive. Also it is known, [33–35], that two Qballs which are exactly out of phase, $\theta = \pi$, repel and this is again verified as $\mathcal{F} > 0$.

For the non-integrable case ($F = 1$) we have a potential of the form

$$W = |\phi|^2 - |\phi|^4 + \beta|\phi|^6, \qquad (2.9.9)$$

where the function,

$$C_\omega = \frac{2a}{\sqrt{1-4\beta a^2}}. \tag{2.9.10}$$

This gives an interaction force

$$\mathcal{F}_{QB} = -\frac{16a^4}{1-4\beta a^2}\cos\theta e^{-2a\alpha}. \tag{2.9.11}$$

In the complex sine-Gordon case $F = 1-\phi\bar{\phi}$, $W = \phi\bar{\phi}$ and $C_\omega = -16a^2$ giving

$$\mathcal{F}_{CSG} = -16a^4 e^{-2\alpha a}\cos\theta. \tag{2.9.12}$$

(2.9.11) and (2.9.12) show that for $\beta = 0$ two complex sine-Gordon solitons have the same interaction force as the force between two Qballs in the truncated model. Also in the small charge limit, $a \to 0$, the usual Qball model, the truncated model and the complex sine-Gordon model all have the same interaction force. In this limit the respective charges, energy and equations of motion all converge. This shows that two small charged, well separated, Qballs will behave similarly irrespective of the model. Hence we expect to observe some integrable characteristics starting to occur in the non-integrable models in the small charge limit, as previously numerically shown.

2.10 Qball perturbation.

A general property of field theories is that we can perturb their minimum energy field configurations by a small amount. In the Qball model this has to be performed in a charge conserving manner. Due to the non-static internal phase this gives two main classes of perturbation; spatial perturbations and an internal space perturbations. These perturbations supply the Qball with energy causing it to oscillate about its charge specific minimum energy solution. These oscillations can manifest in a number of different ways depending on the nature of the model. In a non-integrable

model the Qball oscillations are damped by consistently radiating energy.

2.10.1 Perturbations in the complex sine-Gordon theory.

Setting $F = 1 - \phi\bar{\phi}$ and $W = \phi\bar{\phi}$ in (2.7.4) gives the Complex Sine-Gordon Lagrangian density. As stated above there are two main types of perturbations, spatial and internal. For the perturbation to conserve charge Q,

$$Q = i\int \frac{(\phi\dot{\bar{\phi}} - \bar{\phi}\dot{\phi})}{1-\phi\bar{\phi}}dx = 2\omega\int\left(\frac{f^2}{1-f^2}\right)dx. \tag{2.10.1}$$

The simplest perturbations are:

1. The spacial perturbation

$$\begin{aligned} x &\rightarrow \lambda x, \\ f^2 &\rightarrow \frac{\lambda f^2}{1+(\lambda-1)f^2}. \end{aligned} \tag{2.10.2}$$

2. Internal space perturbation

$$x \rightarrow \lambda x, \tag{2.10.3}$$

$$\phi \rightarrow e^{i\omega t\lambda} f. \tag{2.10.4}$$

We simulate the above perturbations by perturbing the minimum energy complex sine-Gordon solution (2.6.3) for $\omega = 0.4$. Using the same technique as previously described we evolve the new initial conditions on a lattice of 25000 grid points, with spacial separation $\Delta x = 0.02$ and time steps $\Delta t = 0.001$. To replicate an infinite line we implement absorbing boundary conditions. This stops radiation from being reflected back into the bulk and causing secondary perturbations. After every 4000 time steps we plot the field value at the origin, $|\phi(0)|$, giving Figure 2.7.

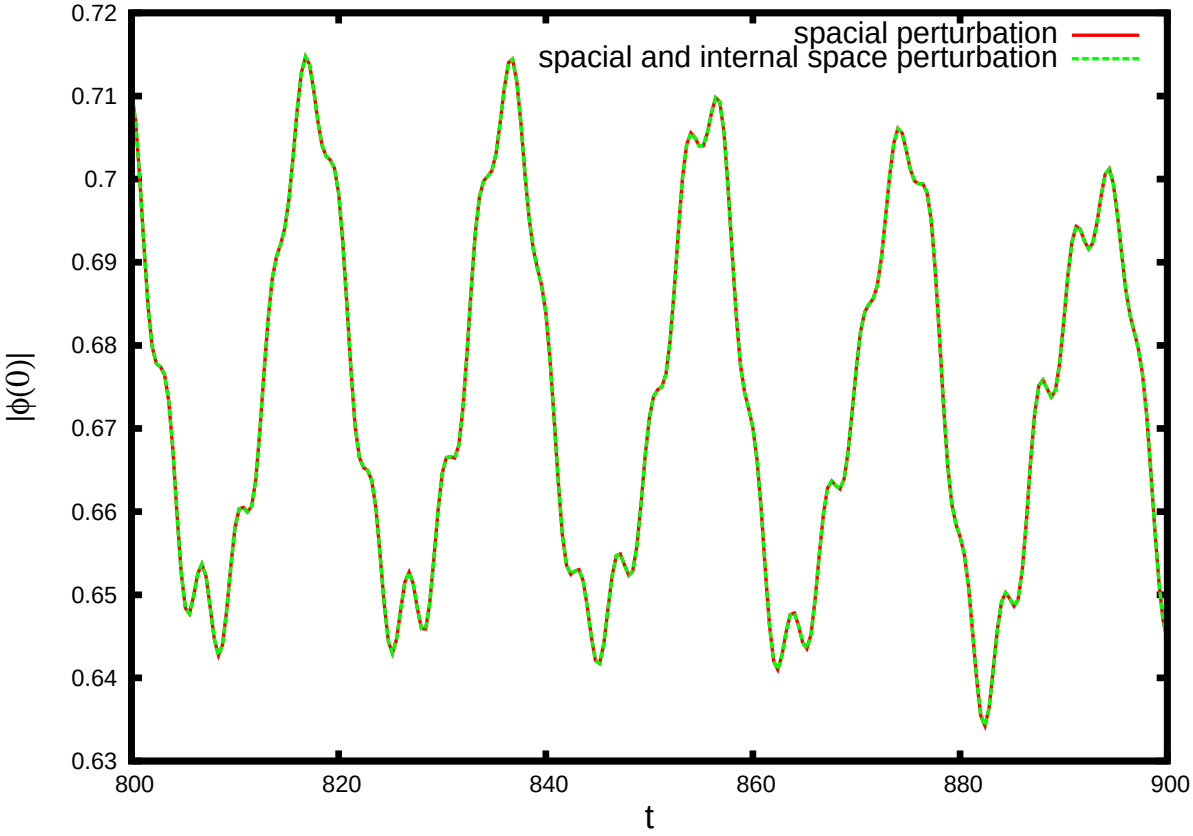

Figure 2.7: $|\phi(0)|$ of a perturbed complex sine-Gordon soliton with internal frequency $\omega = 0.4$.

Figure 2.7 shows that the two perturbations give rise to almost exactly the same oscillations, and there is more than one excited mode. This led us to numerically calculate a power spectrum of the data in Figure 2.7, giving Figure 2.8.

The Power spectrum shows the relative distribution of energy in each oscillation mode and the vibrational frequency of that mode. This is achieved by first normalising the data in Figure 2.7, giving $\phi(0)_N$, then numerically evaluating

$$P(\Omega) = \int_{-\infty}^{\infty} e^{i\Omega t} |\phi(0)_N| dt, \tag{2.10.5}$$

where $P(\Omega)$ is the power spectrum. The power spectrum, $P(\Omega)$, in Figure 2.8 shows the oscillatory modes and their relative excitations in the complex sine-Gordon model.

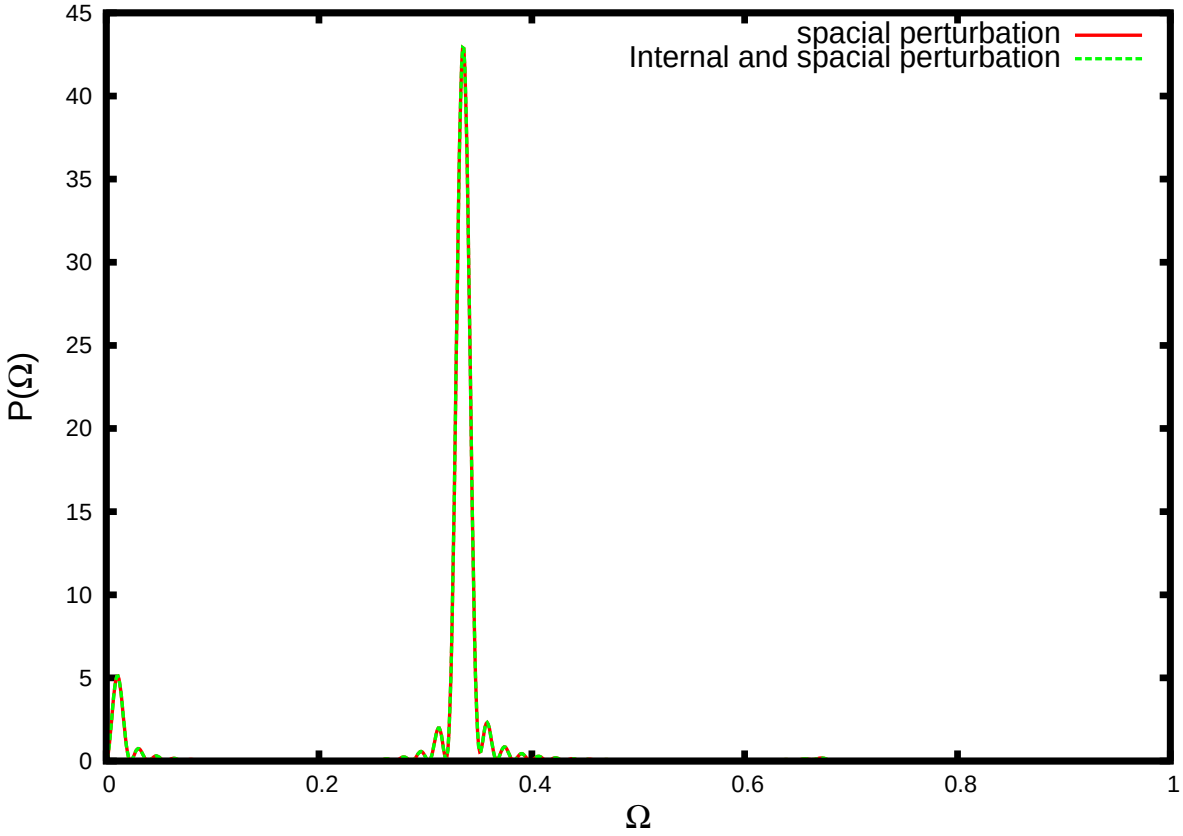

Figure 2.8: Power spectrum density of a perturbed complex sine-Gordon soliton with internal frequency $\omega = 0.4$.

2.10.2 Normal Qball perturbations.

As previously detailed for any perturbation to be consistent it must conserve Q,

$$Q = i\int(\phi\bar{\dot{\phi}} - \bar{\phi}\dot{\phi})dx = 2\omega\int f^2 dx. \tag{2.10.6}$$

Due to the non-integrable Qball theory not having a fractional sigma term, in its Lagrangian density, the charge conserving perturbations take the different forms:

1. Spacial perturbation

$$x \to \lambda x, \quad f \to \sqrt{\lambda} f. \tag{2.10.7}$$

2. Combined internal and spacial perturbation

$$x \to \lambda x, \quad \omega \to \lambda\omega. \tag{2.10.8}$$

Using the same technique as outlined above, for the complex sine-Gordon model, we can simulate the behaviour of a perturbed Qball. One thing to be noted is that the non-integrable Qballs do not need to have a lattice spacing and time step as small as the complex sine-Gordon model; for these simulations we used a lattice of 24000 grid points with a spacing $\Delta x = 0.05$ and time step $\Delta t = 0.01$. Absorbing boundary conditions were implemented, which in this case played a more significant role, due to the perturbed Qball continuously radiating. If we again record $|\phi(0)|$ every 4000 time steps for both perturbations we gain Figure 2.9.

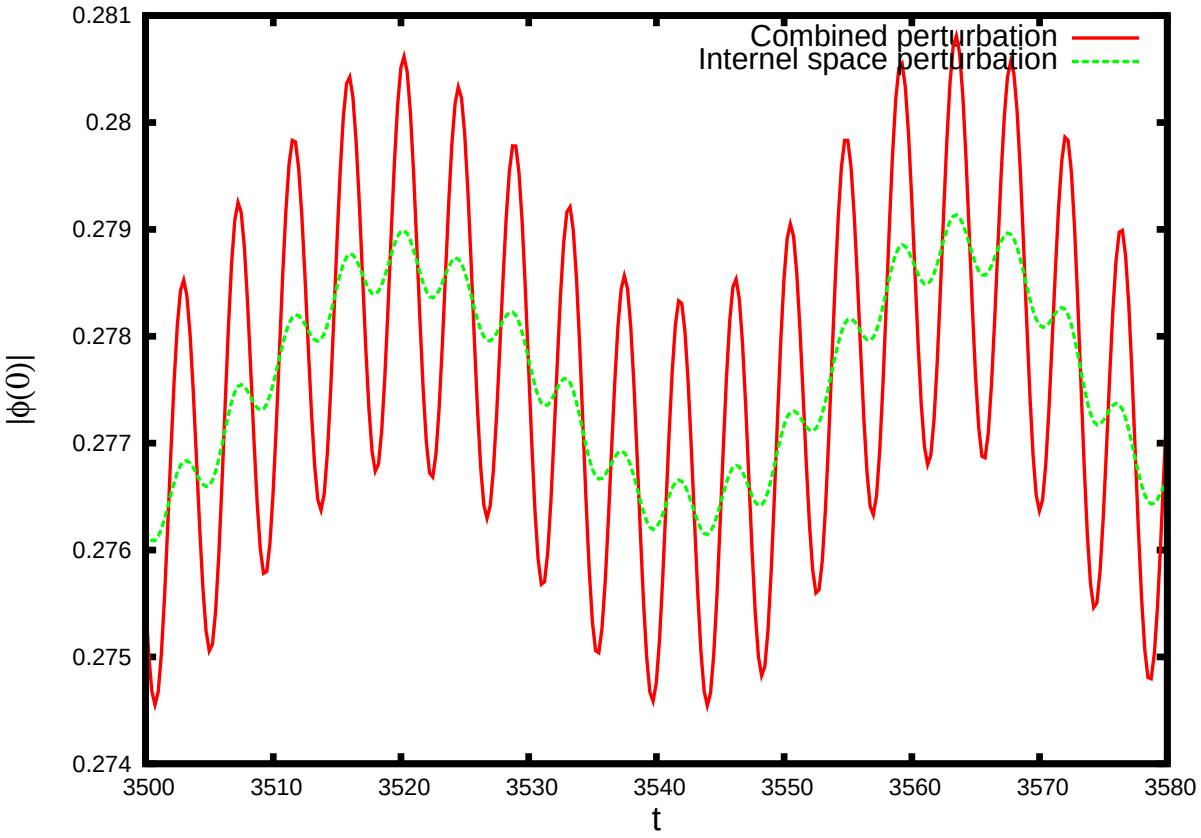

Figure 2.9: $|\phi(0)|$ of a perturbed truncated Qball with internal frequency $\omega = 0.85$.

Figure 2.9 clearly shows that the purely spacial and the combined perturbations excite the same modes, but with different relative energies. Calculating the power spectrum for the data in Figure 2.9 gives Figure 2.10; which shows that there are two oscillatory modes. It is worth noting that the non-integrable model has a vibration mode of $\Omega > 1$ which is outside of the region of ω for a stable Qball.

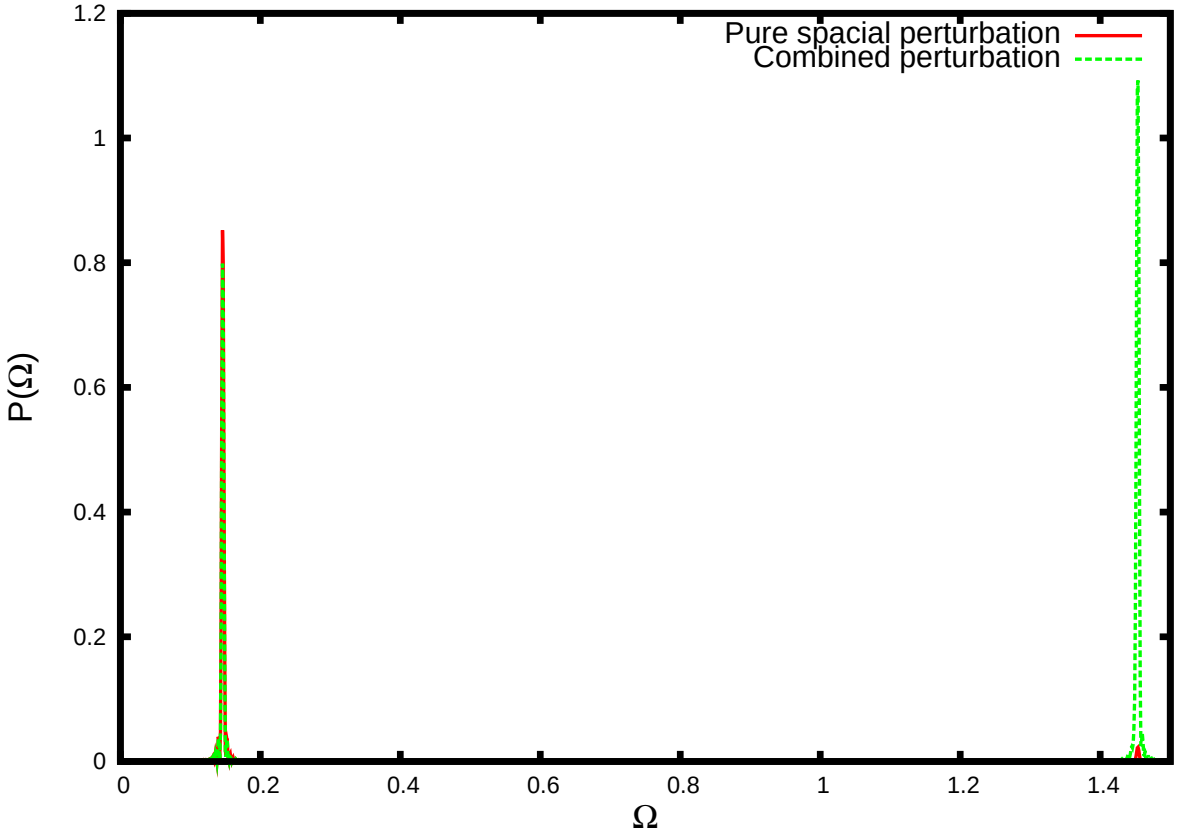

Figure 2.10: Power spectrum density of truncated Qball with internal frequency $\omega = 0.85$.

2.11 Perturbation moduli approximation.

We used a moduli approximation to understand what each of these vibrational modes physically represent. To do this, for the non-integrable model, we perturb (2.2.1) and then solve the subsequent equations of motion with respect to two real moduli, $\alpha(t)$ and $\theta(t)$. Choosing a more general perturbation of the internal space as

$$\phi = \alpha e^{i\theta} f(x), \tag{2.11.1}$$

then simplifying components of the resulting Lagrangian density as,

$$\begin{aligned}
\int \dot{\phi}\dot{\bar{\phi}} &= (\dot{\alpha}^2 + \alpha^2\dot{\theta}^2)I_2, \\
\int |\phi'|^2 &= \alpha^2 I_x, \\
\int |\phi|^2 &= \alpha^2 I_2, \\
\int |\phi|^4 &= \alpha^4 I_4, \\
\int |\phi|^6 &= \alpha^6 I_6.
\end{aligned}$$

We gain the Lagrangian density

$$\mathcal{L} = (\dot{\alpha}^2 + \alpha^2\dot{\theta}^2)I_2 - \alpha^2 I_x - \alpha^2 I_2 + \alpha^4 I_4 - \beta\alpha^6 I_6.$$

We can then vary this Lagrangian with respect to the real moduli, α and θ, giving the two equations of motion

$$\ddot{\alpha}I_2 - \alpha\dot{\theta}^2 I_2 + \alpha(I_x + I_2) - 2\alpha^3 I_4 + 3\beta\alpha^5 I_6 = 0 \tag{2.11.2}$$

$$2\dot{\alpha}\dot{\theta} + \alpha\ddot{\theta} = 0. \tag{2.11.3}$$

To solve these coupled equations for a small perturbation we set $\dot{\theta} = \omega + \dot{\eta}$ and

$\alpha = 1 + \epsilon$, where $\eta << 1$ and $\epsilon << 1$. From (2.11.3) we gain

$$\dot{\eta} = -2\omega\epsilon + c$$

where c is a constant of integration. Substituting this into (2.11.3) gives a differential equation for ϵ,

$$\ddot{\epsilon} I_2 + \epsilon(3\omega^2 I_2 + I_x + I_2 - 6I_4 + 15\beta I_6) - \omega^2 I_2 + I_x + I_2 - 2I_4 + 3\beta I_6 = 0.$$

Hence the system oscillates at

$$\Omega = \sqrt{\frac{3\omega^2 I_2 + I_x + I_2 - 6I_4 + 15\beta I_6}{I_2}}.$$

Calculating all the necessary integrals, I, we can verify this for a single truncated Qball as

$$\Omega = \sqrt{\left(\frac{20\omega^2 - 8}{3}\right)}. \tag{2.11.4}$$

So for an $\omega = 0.85$ we find $\Omega = 1.47$. This is in very close agreement to the power spectrum of the previous simulation of a perturbed truncated Qball, with internal frequency $\omega = 0.85$, which has a oscillatory mode at $\Omega = 1.45$. From this we believe the upper frequency vibrational mode to be caused by a perturbation in internal space.

2.12 Qball minor-Qball coupling.

In section 2.10.2 on calculation of the power spectrum we noticed that there were two main vibrational modes, and in section 2.11 we have shown that the upper frequency mode is due to a perturbation in internal space.

During the cycle of a perturbed Qball we noticed that the field configuration is comparable to that of a complex sine-Gordon breather. Using this we are able to

predict the creation of a second much smaller Qball under perturbation.

2.12.1 Complex sine-Gordon breather.

To construct a complex sine-Gordon breather we first need a two soliton solution of the complex sine-Gordon model. The construction of a multi-soliton solution, by a Bäcklund transformation of the complex sine-Gordon model, is highly involved and slightly exceeds the focus of this thesis. Bäcklund transformations were first used by differential geometers to iteratively create pseudo-spherical surfaces [36]. They link two or more solutions, of the relevant equations of motion, together with solutions of a dual model and Bäcklund parameters δ_i. Using a Lorentz boosted complex sine-Gordon soliton solution centred at α_i at time $t = 0$

$$\phi_i = a_i \exp(i\omega_i(t - v_i(x - \alpha_i)))\mathrm{sech}(a_i\gamma_i(x - \alpha_i - v_i t)),$$

where γ_i is the Lorentz factor

$$\gamma_i = \frac{1}{\sqrt{1 - v_i^2}}.$$

Then defining an associated complex kink function defined as

$$\psi_i = -a_i \tanh(a_i\gamma_i(x - \alpha_i - v_i t)) - i\omega_i. \tag{2.12.1}$$

We can combine two complex sine-Gordon solutions ϕ_1 and ϕ_2 with two kink solutions ψ_1 and ψ_2. This gives the two soliton complex sine-Gordon solution

$$\phi_{1,2} = \frac{(-\delta_1\bar{\psi_2} + \delta_2\bar{\psi_1})(\delta_1\phi_1 - \delta_2\phi_2) + (-\delta_1\phi_2 + \delta_2\phi_1)(-\delta_1\psi_1 + \delta_2\psi_2)}{\delta_1^2 + (-\bar{\phi_1}\phi_2 - \bar{\phi_2}\phi_1 - \bar{\psi_1}\psi_2 - \bar{\psi_2}\psi_1)\delta_1\delta_2 + \delta_2^2}. \tag{2.12.2}$$

This solution was first found in [30] using the Hirota method. It gives a two soliton solution, $\phi_{1,2}$, via a superposition technique with Bäcklund parameters $\{\delta_1, \delta_2\}$. We

can set the Bäcklund parameters to be

$$\delta_i = \sqrt{\frac{1-v_i}{1+v_i}}. \tag{2.12.3}$$

The way in which we create our complex sine-Gordon breather from (2.12.2) is by setting $\alpha_i = v_i = 0$ in (2.12.3). This places two complex sine-Gordon solitons on top of each other, at the origin of the system, and has the field configuration

$$\phi_B = \frac{\Delta\omega(a_2 e^{i\omega_2 t}\cosh(x_1) - a_1 e^{i\omega_1 t}\cosh(x_2))}{(1-\omega_1\omega_2)\cosh(x_1)\cosh(x_2) - a_1 a_2(\cos(\Delta\omega t) + \mathrm{sech}(x_1)\mathrm{sech}(x_2))}, \tag{2.12.4}$$

where

$$\Delta\omega = \omega_1 - \omega_2,\ x_i = a_i x. \tag{2.12.5}$$

It is simply seen in (2.12.4) that the system will oscillate with angular frequency $\Omega_c = \Delta\omega$. This led us to hypothesize that for a small perturbation it is energetically inexpensive for a Qball to create a second smaller Qball of internal frequency ω_2. So a perturbed Qball has the ability to lose energy by creating a second smaller Qball as long as total charge is conserved.

To test this coupled Qball hypothesis we performed a simulation of two truncated Qballs placed on top of each other using the initial condition

$$\phi = e^{i\omega_1 t} f_{\omega_1} + e^{i\omega_2} f_{\omega_2}. \tag{2.12.6}$$

This ansatz is two minimum energy solutions place on top of each other with $\omega_1 = 0.95$ and $\omega_2 = 0.99999$. Using the above analysis we expect the system to oscillate at $\Omega_c = 0.9999 - 0.95 = 0.04999$. Figure 2.11 shows that the two-Qball system oscillates at $\Omega \sim 0.055$. This is very close to the predicted $\Omega_c = \Delta\omega = 0.04999$. This minor deviation could be explained by numerical approximations and the two Qball system not being integrable.

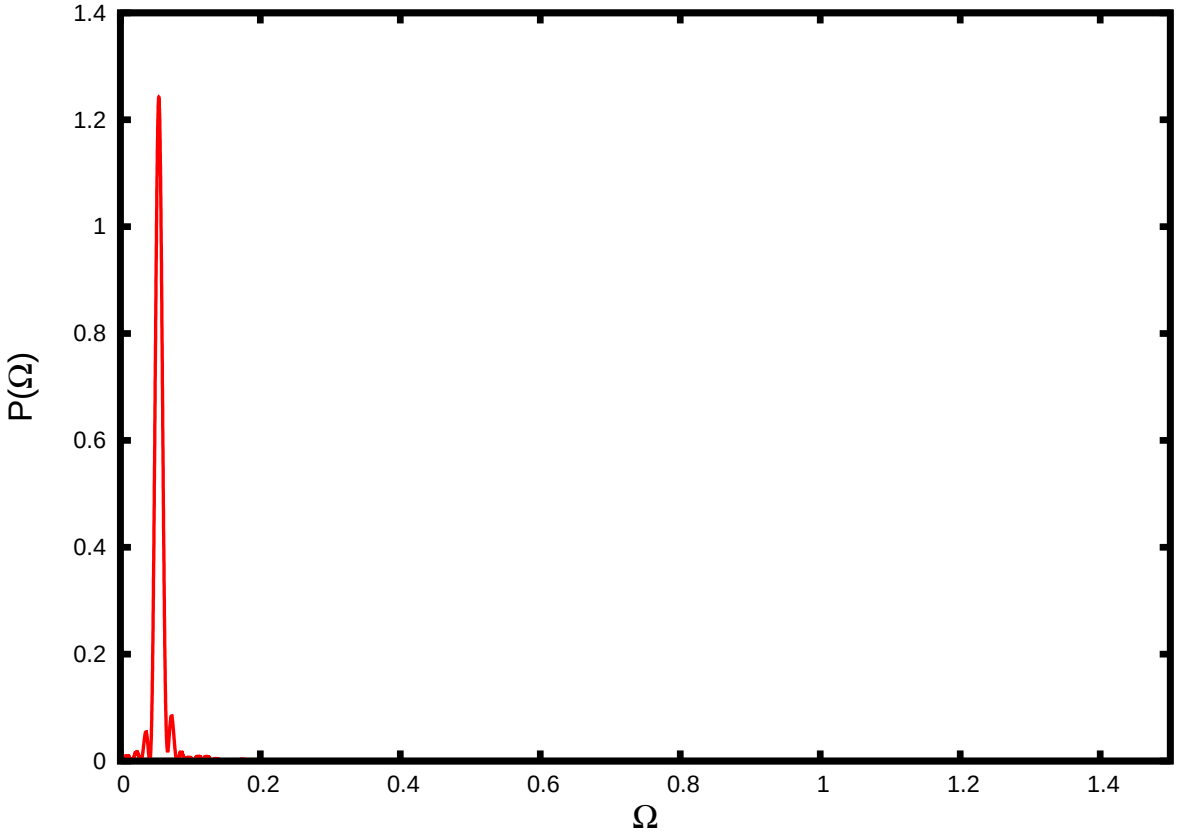

Figure 2.11: Power Spectrum density of a truncated Qball coupled to a smaller Qball with internal frequencies $\omega_1 = 0.95$ and $\omega_2 = 0.99999$.

We now have the ability to understand the oscillatory nature of the total charge zero Qball anti-Qball superposition in section 2.8.2. If we calculate the power spectrum of the data in Figure 2.6 we gain Figure 2.12. This shows that there is a major oscillatory mode at $\Omega \sim 1.8$. This matches the value predicted by (2.12.4) of $\Omega_c = \Delta\omega = 1.8$. This shows that the charge-less Qball anti-Qball system can also enter into a breather state.

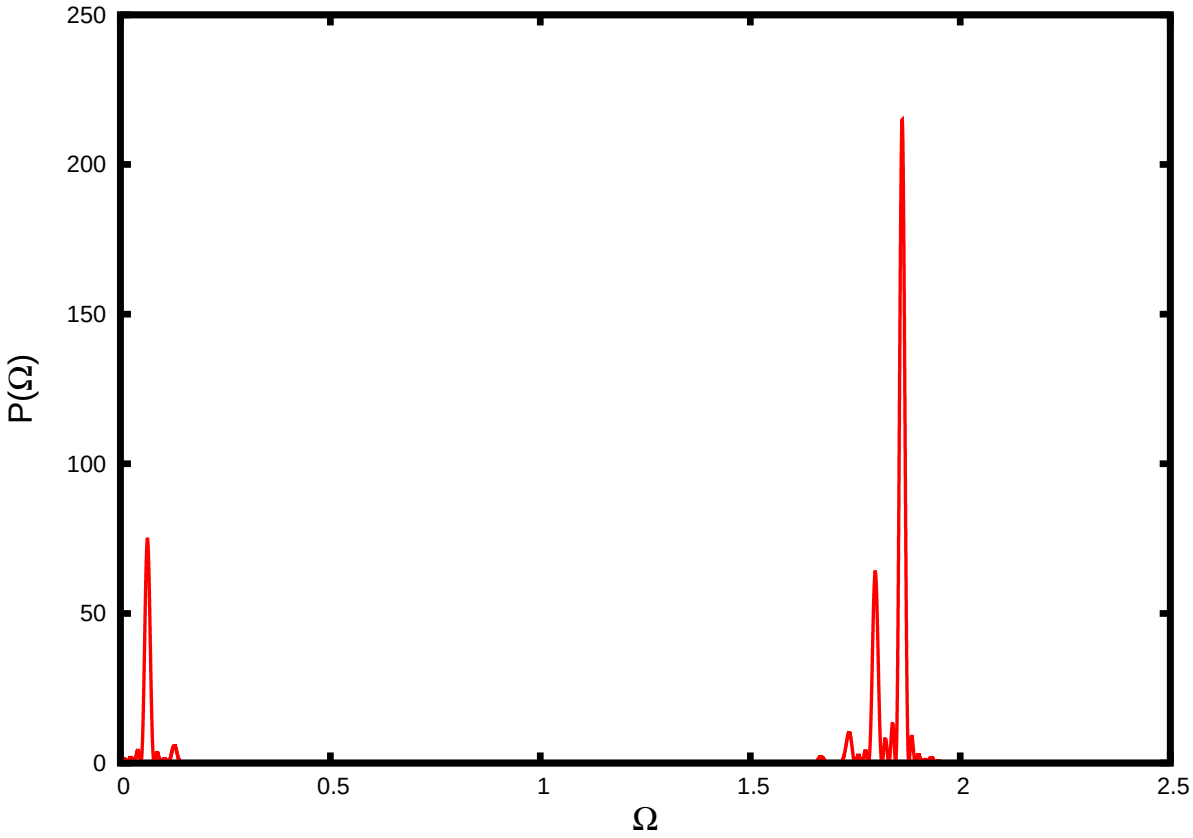

Figure 2.12: Power spectrum density of a coupled truncated Qball anti-Qball breather with internal frequencies $\omega_1 = -\omega_2 = 0.9$.

2.13 Summary and conclusion.

We noticed that the soliton solution of the complex sine-Gordon model is actually a Qball type solution. This motivated the observation that the standard Qball model and the complex sine-Gordon model converge in the small charge limit. This led us to realise that all the non-integrable Qball models posses a limit where they display semi-integrable behaviour. We verified this behaviour by numerical simulations of Qball-Qball collisions and breather states.

Using this semi-integrable behaviour we managed to gain an understanding of the outcome of Qball collisions. We found the surprising resistance Qballs have to total annihilation under Qball anti-Qball collisions. In the event of a collision not only do the Qballs interact they also enter an excited perturbed state. These perturbed states were found to have quite specific oscillatory modes, two of which we have

been able to explain. We found the upper frequency mode to be a consequence of a perturbation of internal space. The second major mode, the lower frequency mode, was found to be caused by a second small ($\omega \sim 1$) Qball being formed which absorbed the excess energy. We also found that small charge breathers exist for a long period of time and radiate negligible amounts of radiation. This is similar to the known complex sine-Gordon breather state. Also, the link between the complex sine-Gordon model and the normal Qball model led us to formulate a new truncated Qball model. This truncated model has stable soliton solutions based on a false vacuum.

Chapter 3

Baby skyrmion chains.

3.1 Introduction.

The Skyrme model is a $(3+1)$-dimensional non-linear theory of pions and admits topological soliton solutions, which describe baryons. In this chapter we are concerned with a lower dimensional analogue, known as the baby skyrmion model [1,38]. As a lower dimensional analogue of the Skyrme model the baby skyrmion model can be used to guide investigations of the Skyrme model. Hence the baby skyrmion theory can be used to aid the application of the Skyrme theory to nuclear physics. In this chapter we present alternative numerical solutions. These solutions are new baby skyrmion chain solutions, which have lower energy than those found previously. These chains are good candidates for the global minimum energy solutions. The baby skyrmion model also has applications in condensed matter physics [6, 39]; but this goes beyond the scope of this thesis. The baby skyrmion model has the Lagrangian density

$$\mathcal{L} = \frac{1}{2}\partial_\mu \boldsymbol{\phi} \cdot \partial^\mu \boldsymbol{\phi} - \frac{\kappa^2}{4}(\partial_\mu \boldsymbol{\phi} \times \partial_\nu \boldsymbol{\phi}) \cdot (\partial^\mu \boldsymbol{\phi} \times \partial^\nu \boldsymbol{\phi}) - m^2(1-\phi_3), \tag{3.1.1}$$

where the field is a three component scalar, $\boldsymbol{\phi} = (\phi_1, \phi_2, \phi_3)$, and takes its value on the unit sphere, $\boldsymbol{\phi} \cdot \boldsymbol{\phi} = 1$.

Theory (3.1.1) is a modified $O(3)$-σ model which includes a fourth power derivative and a symmetry breaking potential. The fourth power derivative is commonly known as the Skyrme term. The Skyrme term coupled with the potential term gives rise to a scale in (3.1.1). This scale means Derrick's theorem, [21], does not exclude soliton solutions in 2-dimensions. This potential is analogous to the pion mass term in the $(3+1)$-dimensional Skyrme model. The positive constant κ in combination with the mass, m, determines the size of the baby skyrmion as being proportional to $\sqrt{\kappa/m}$. For finite energy $\boldsymbol{\phi}$ has to be a constant at the spacial boundary thus we impose the condition

$$\lim_{|\boldsymbol{x}|\to\infty} \boldsymbol{\phi} = (0,0,1). \tag{3.1.2}$$

This condition is the vacuum value of the potential in (3.1.1). The physical space can now be one-point compactified, $\mathbb{R}^2 \cup \{\infty\}$, which is topologically equivalent to S^2. This compactification of the physical space and the compact target space gives rise to the field configuration $\boldsymbol{\phi}$ at fixed time being a map

$$\boldsymbol{\phi} : S^2 \to S^2. \tag{3.1.3}$$

Such maps can be classified by the homotopy class $\pi_2(S^2) = \mathbb{Z}$. This gives the model a topological degree, otherwise known as a topological charge B. The topological charge of the map $\boldsymbol{\phi}$ can be calculated using the pull back of a normalised area form ω, from the target S^2, as

$$\begin{aligned} B &= \deg[\boldsymbol{\phi}] && (3.1.4)\\ &= \int_{\mathbb{R}^2} \boldsymbol{\phi}^*\omega \;\; d^2x \\ &= -\frac{1}{4\pi}\int_{\mathbb{R}^2} \boldsymbol{\phi}\cdot(\partial_1\boldsymbol{\phi}\times\partial_2\boldsymbol{\phi})d^2x, \\ &= \int_{\mathbb{R}^2} j(x_1,x_2)\; d^2x. && (3.1.5) \end{aligned}$$

Here j is defined as the topological charge density.

The aim of this chapter is to discuss the structure of static multi-charge solutions, focusing on the chain-like structure. We show that these chain solutions could be the minimum energy configurations of multi-charge baby skyrmions. Firstly we shall outline the well known symmetry reduction technique used to calculate charge one and two baby skyrmions. Then we shall discuss the numerical computation of higher charge structures, producing the minimum energy chain configurations. We then extend our investigation to include periodic spaces, firstly investigating infinite chains on $\mathbb{R}^1 \times S^1$ and then baby skyrmion crystal structures on the torus $\mathbb{T}^2$.

3.2 Topological charge one and two.

Static baby skyrmions are energetic minima of the energy associated with (3.1.1) namely,

$$E = \int_{\mathbb{R}^2} \left(\frac{1}{2} \partial_i \boldsymbol{\phi} \cdot \partial_i \boldsymbol{\phi} + \frac{\kappa^2}{2} \left| \partial_1 \boldsymbol{\phi} \times \partial_2 \boldsymbol{\phi} \right|^2 + m^2 (1 - \phi_3) + \frac{1}{2} \lambda (1 - \boldsymbol{\phi} \cdot \boldsymbol{\phi}) \right) d^2 x. \tag{3.2.1}$$

The static field equation found from the variation of (3.2.1) is the highly non-linear partial differential equation

$$\begin{aligned} 0 &= \partial_i \partial_i \boldsymbol{\phi} + m^2 \mathbf{e}_3 + \lambda \boldsymbol{\phi} \\ &+ \kappa^2 \left(\partial_i \partial_i \boldsymbol{\phi} (\partial_j \boldsymbol{\phi} \cdot \partial_j \boldsymbol{\phi}) + \partial_i \boldsymbol{\phi} (\partial_i \partial_j \boldsymbol{\phi} \cdot \partial_j \boldsymbol{\phi}) - \partial_i \partial_j \boldsymbol{\phi} (\partial_i \boldsymbol{\phi} \cdot \partial_j \boldsymbol{\phi}) - \partial_j \boldsymbol{\phi} (\partial_i \partial_i \boldsymbol{\phi} \cdot \partial_j \boldsymbol{\phi}) \right). \end{aligned} \tag{3.2.2}$$

Here $\mathbf{e}_3 = (0, 0, 1)$ and λ is a Lagrange multiplier to impose the constraint $\boldsymbol{\phi} \cdot \boldsymbol{\phi} = 1$ as,

$$\begin{aligned} \lambda &= \partial_i \boldsymbol{\phi} \cdot \partial_i \boldsymbol{\phi} - m^2 \mathbf{e}_3 \cdot \boldsymbol{\phi} \\ &+ \kappa^2 (\partial_i \boldsymbol{\phi} \cdot \partial_i \boldsymbol{\phi} (\partial_j \boldsymbol{\phi} \cdot \partial_j \boldsymbol{\phi}) - \partial_j \boldsymbol{\phi} \cdot \partial_i \boldsymbol{\phi} (\partial_j \boldsymbol{\phi} \cdot \partial_i \boldsymbol{\phi})). \end{aligned}$$

The only way to find solutions of (3.2.2) is to use a numerical technique. Throughout this chapter we used a gradient flow numerical minimisation scheme. This minimises (3.2.1) by relaxing the partial differential equation (3.2.2). A very effective simplification of (3.2.1), and hence its corresponding field equation (3.2.2), is to use the underlying symmetry of an $O(2)$ rotation in the physical space. This rotation can be neutralised by an iso-rotation of the target space. This technique is known as the Hedgehog ansatz and is covered extensively in [38]. Here it is shown that the field, $\boldsymbol{\phi}$, can be re-expressed with axial symmetry in terms of a profile function, $f(r)$, and a polar angle, θ, as

$$\boldsymbol{\phi}(\boldsymbol{x}) = (\sin f \cos(B\theta - \chi), \sin f \sin(B\theta - \chi), \cos f), \tag{3.2.3}$$

with a phase $\chi \in [0, 2\pi)$. The profile function, $f(r)$, takes the values $f(0) = \pi$ and $f(\infty) = 0$. Using this simplification the static energy (3.2.1) becomes

$$E = 2\pi \int_0^\infty \left(\frac{1}{2} f'^2 + (1 + \kappa^2 f'^2) \frac{B^2}{2r^2} \sin^2 f + m^2 (1 - \cos f) \right) r dr. \tag{3.2.4}$$

Varying (3.2.4) gives

$$\begin{aligned} 0 &= f'' \left(r + \frac{\kappa^2 B^2 \sin^2 f}{r} \right) + f' \left(1 - \frac{\kappa^2 B^2}{r^2} \sin^2 f + f' \frac{\kappa^2 B^2}{2r} \sin(2f) \right) \\ &- \frac{B^2}{2r} \sin(2f) - m^2 r \sin f. \end{aligned} \tag{3.2.5}$$

For comparative consistency with [38] we chose $\kappa = 1$ and $m^2 = 0.1$. A gradient flow algorithm is then implemented using (3.2.5) to minimise (3.2.4). The minimum energies for $B = 1$ and $B = 2$ are found to be $E_1 = 19.66$ and $E_2 = 36.90$ respectively. These energies are within 0.03% agreement with the results of [38]. The profile functions for these solutions are then used to generate the 2-dimensional topological charge density plots in figure 3.1.

It is known that the minimal energy solutions are not axially symmetric for

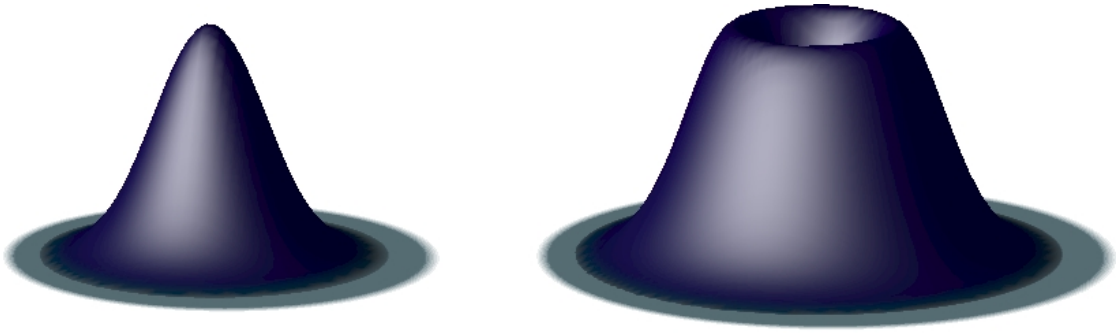

Figure 3.1: Two-dimensional plots of the topological charge density, j, of baby skyrmions with $B = 1$ on the left and $B = 2$ on the right.

$B > 2$ [38]. Only $B = 1, 2$ minimum energy baby skyrmion solutions can be calculated using the above method. For $B > 2$ this approach creates ring baby skyrmion structures. These are not stable to perturbations and break the axial symmetry. Therefore to calculate $B > 2$ minimum energy baby skyrmions full field two-dimensional gradient flow is required.

3.3 Larger charge baby skyrmions $B > 2$.

For $B > 2$ it is known, [38], that axially symmetric solutions are not stable to perturbations which break axial symmetry. To proceed we solve the static field equation, (3.2.2), using a 2-dimensional gradient flow algorithm. To create multiple baby skyrmion initial conditions it is conducive to use the stereographic coordinates

$$W = \frac{\phi_1 + i\phi_2}{1 + \phi_3}. \tag{3.3.1}$$

Then using the previous Hedgehog ansatz we can create n baby skyrmions of topological charge B_i, each with field configuration centred at $\boldsymbol{\phi}_i(x_i, y_i)$. Using the stereographic coordinates (3.3.1) and summing these configurations as,

$$W = \sum_{i}^{n} W_i. \tag{3.3.2}$$

Then under the inverse stereographic projection we gain a smooth field configuration of multiple baby skyrmions. With topological charge

$$B = \sum_{i}^{n} \deg[\boldsymbol{\phi}_i].$$

A sum of n charge one baby skyrmions in stereographic coordinates (3.3.1), equally separated on a circle, with arbitrary phase is used as an initial condition. This configuration is then numerically minimised using gradient flow, on a 200×200 lattice with a spacing of $\Delta x = 0.2$, using fourth-order accurate derivatives. As a comparison, which validates the two-dimensional minimisation algorithm, the minimum energies of the $B = 1$ and $B = 2$ are calculated to be $E_1 = 19.65$ and $E_2 = 36.90$. These $B = 1, 2$ values differ slightly from the two-dimensional results in [38], [40] and [41]. The previously published results seem to differ by 1% compared to the greater accuracy axial solutions. Our results are in better agreement with the previous dimensionally reduced solutions, with $E_1 = 19.66$ and $E_2 = 36.90$. We also have a closer agreement with the dimensionally reduced results of the collective literature. We believe our slightly greater accuracy is due to the use of the fourth-order accurate finite differences in comparison to the second-order differences commonly used.

3.3.1 Topological charge $B = 3, 4$.

Minimisation of $B = 3, 4$ initial conditions reveal energies of $E_3 = 55.58$ and $E_4 = 73.61$. These are close to the previous literatures energies plus a 1% perceived discrepancy in their computations. We also gain similar charge density distributions as in [38], shown in figure 3.2.

The configurations for $B = 1, 2, 3, 4$ which we obtain are essentially identical to those of [38]. The first major difference between our results and the results contained in [38] arises at $B = 5$.

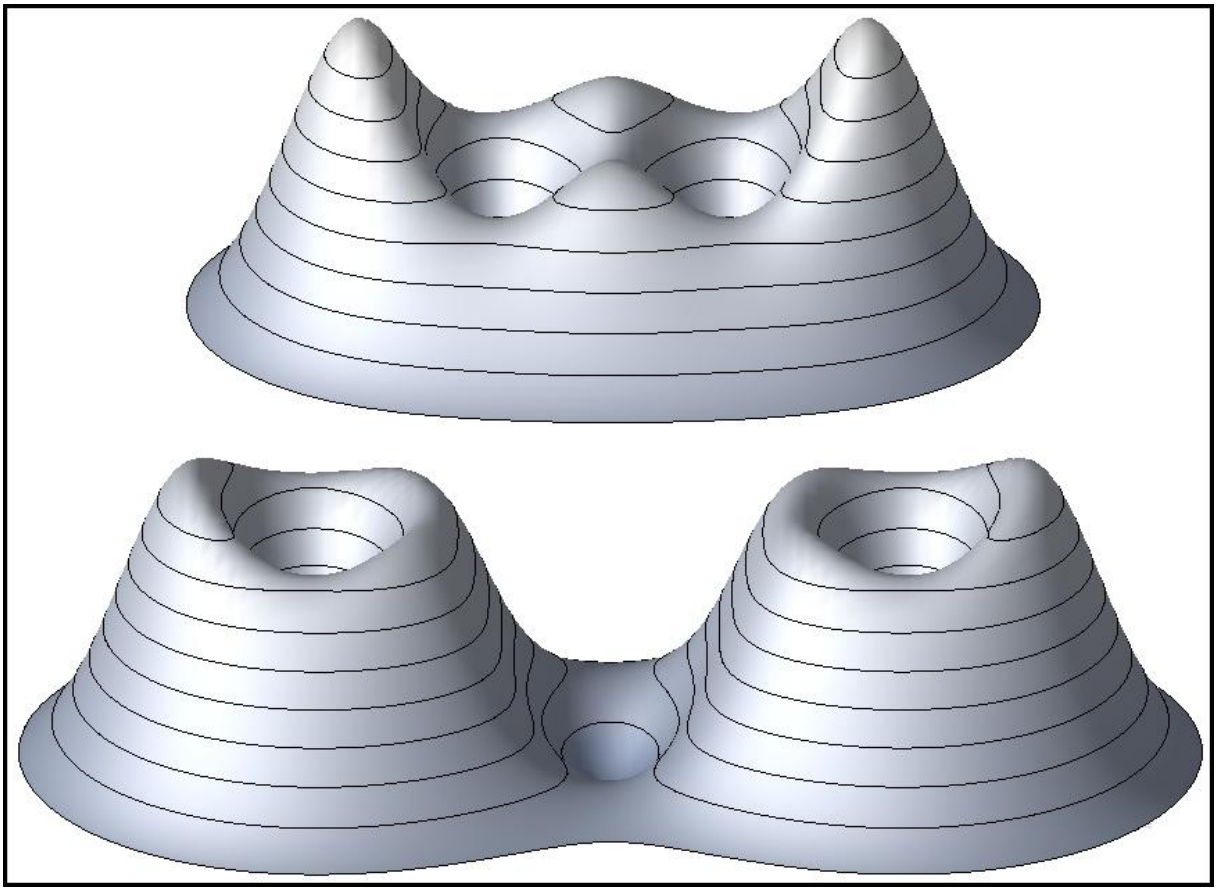

Figure 3.2: Two-dimensional plots of the topological charge densities, j. For the $B = 3$ baby skyrmion on the top and the $B = 4$ baby skyrmion on the bottom.

3.3.2 Topological charge $B = 5$.

A configuration of five $B = 1$ baby skyrmions, equally spaced to form a ring, each with a random relative phase, χ, is used as the initial condition. This initial configuration gradient flows to the chain configuration shown in Figure 3.4. This configuration has energy $E_5 = 92.02$ and is different to the $B = 3 + 2$ solution proposed in [38]. By setting up a system of baby skyrmions as in figure 3.3, which possesses an underlying symmetry about the y-axis, we are able to minimise to a $B = 3 + 2$ solution with an energy of $E = 92.41$.

Therefore we believe our chain solution is of a lower energy. A third justification of our results is shown in figure 3.4. This figure shows that the initial condition, of five $B = 1$ baby skyrmions in a ring, flows through a slightly perturbed $3 + 2$ solution, and minimises to a chain configuration. This shows that the chain solution

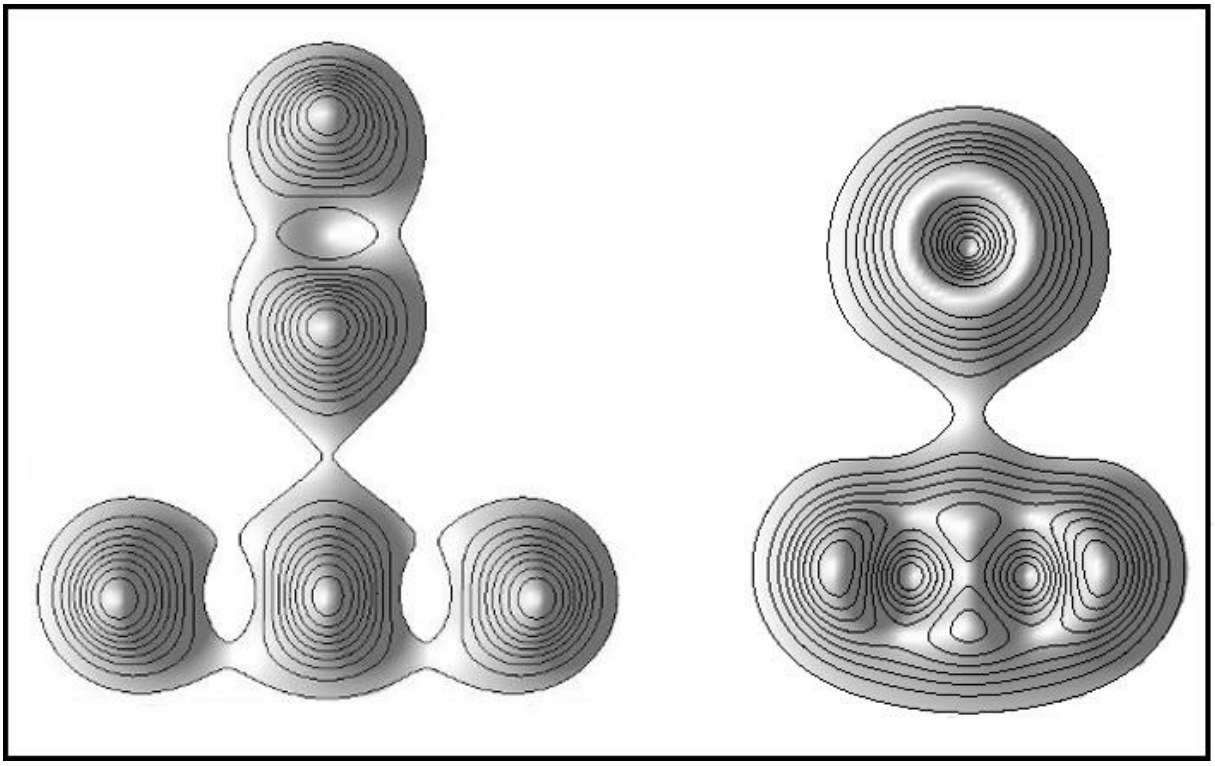

Figure 3.3: Two-dimensional plots of topological charge density, j. On the left five $B = 1$ baby skyrmionswhich was used as initial conditions to create the $B = 3 + 2$ solution on the right.

must be of a lower energy than the accepted $3+2$ modular solution. We believe the $3+2$ solution is a very long lived saddle point in the energetic landscape. Also, [42] has a $B = 5$ static chain configuration for a potential term of the form $m^2(1-\phi_3)^{0.9}$, but there seems to be no comment on this new configuration.

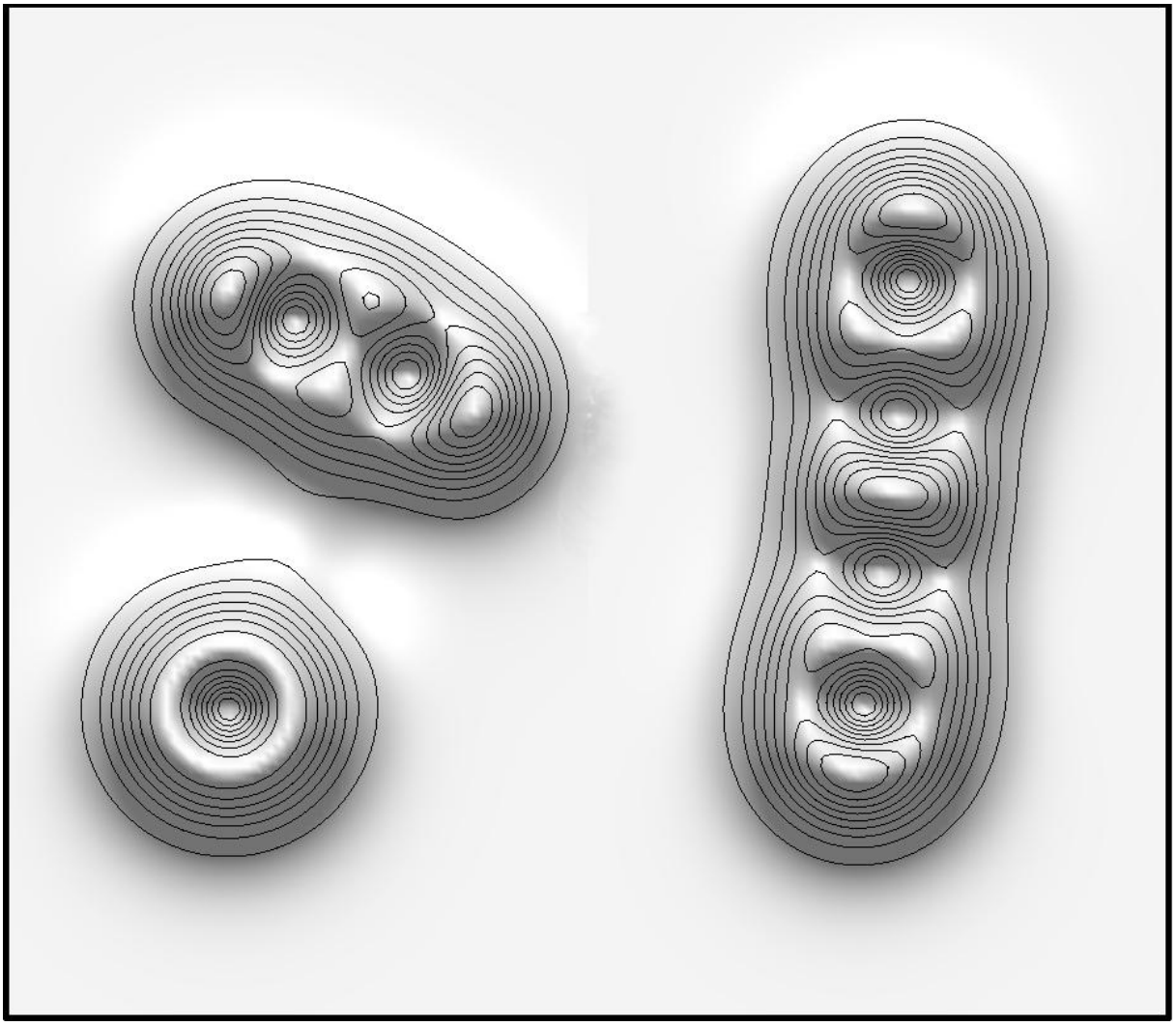

Figure 3.4: Two-dimensional plots of topological charge density, j, of a $B = 5$ baby skyrmions. A perturbed version of the previously accepted $B = 3 + 2$ configuration on the left which then flows to the new $B = 5$ chain on the right.

3.3.3 Topological charge $B = 6$.

The next configuration which differs from the common results of the literature is the $B = 6$ case. Using a circle of six $B = 1$ baby skyrmions as the initial configuration led to a minimum energy configuration similar to the $B = 6$ configuration presented in [38]. This is a configuration of three $B = 2$ baby skyrmions located at the vertices of an equilateral triangle as in figure 3.5. We found the minimum energy of this triangular solution to be $E_6^{\Delta} = 110.30$. This configuration does not match with

the incremental structure common to all the previous lower charge configurations. This deviation from the chain form led us to minimise the energy of a row of six out of phase baby skyrmions. This produced a $B = 6$ chain of static energy $E_6 = 110.22$. Due to the difference in energy being less than 0.1% we believe the triangular structure to be a local minimum energy configuration.

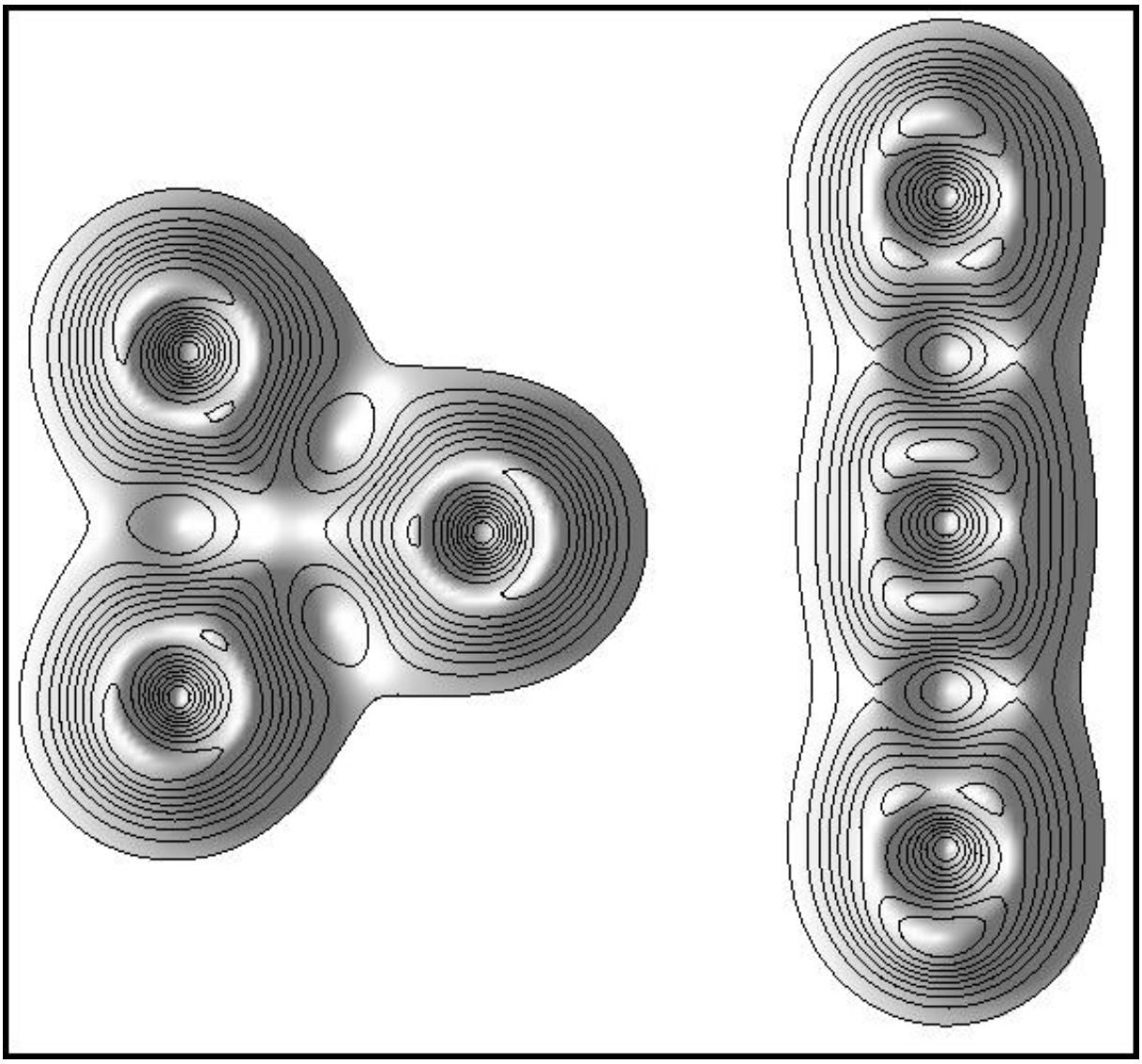

Figure 3.5: Two-dimensional plots of the topological charge densities, j. The previously accepted $B = 2 + 2 + 2$ baby skyrmion triangular configuration on the left and the new $B = 6$ chain solution on the right.

3.3.4 Topological charge $B > 6$.

For topological charges $6 < B \leq 10$ we systematically found the minimum energy solution to be a baby skyrmion chain. We also energetically minimised some larger charges, namely $B = 20, 21$, and were again able to find chain solutions.

B	E	$E/4\pi B$
1	19.65	1.564
2	36.90	1.468
3	55.58	1.474
4	73.61	1.464
5	92.02	1.464
6	110.22	1.462
7	128.55	1.461
8	146.81	1.460
9	165.11	1.460
10	183.38	1.459
20	366.20	1.457
21	384.48	1.457

Table 3.1: Minimum energies of charged baby skyrmions

One of the features of the chains is that for large topological charge the central body appears to be made of uniform, overlapped charge one baby skyrmions. Also the topological charge density tends to be less uniform nearer the ends of the chain, where upon they appear similar to highly perturbed topological charge two baby skyrmions. These $B = 2$ baby skyrmions seem to 'cap' the ends of the chain, as in figure 3.6 for $B = 20$.

Apart from the exceptional case of $B = 3$ the general trend, as observed in figure 3.7, is that the energy per-unit topological charge decreases with increasing topological charge. On top of this general trend there is a finer structure that differentiates between even and odd B.

This is because even B baby skyrmion chains can be interpreted as a modular structure of tightly bound $B = 2$ baby skyrmions. The odd B baby skyrmion chains again have the same $B = 2$ modular structure but also with an extra, less tightly bound, $B = 1$ baby skyrmion. The asymptotic energy per-unit topological charge

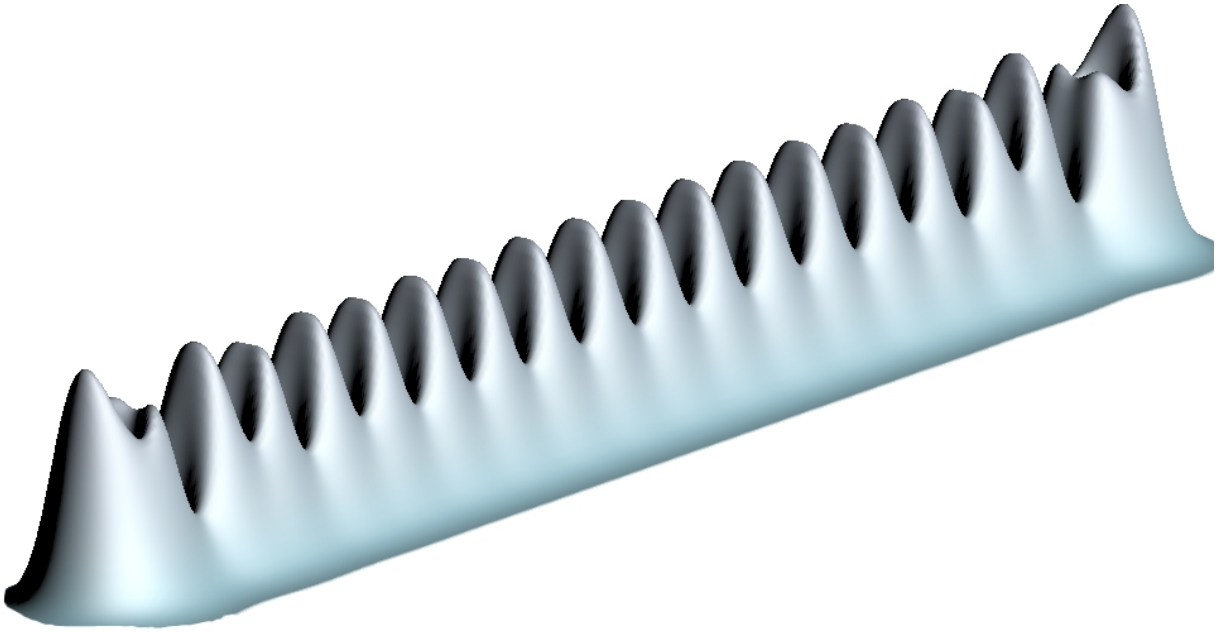

Figure 3.6: Two-dimensional plot of the topological charge density, j, of the $B = 20$ baby skyrmion chain.

with the periodic nature of the central topological charge density, as shown in Figure 3.6. This motivated the calculation of the energy per-unit topological charge of an infinitely charged baby skyrmion chain. This is described in the next section.

3.4 Baby skyrmions on a cylinder.

This section is similar to the work in [43]. The aim is to calculate the minimum baby skyrmion energy per-unit topological charge of an infinitely topological charged chain. As presented in [38] it can be shown that two well separated baby skyrmions have an interaction energy, that depends on a relative phase $\Delta\chi$. This can be calculated using a dipole approximation to be

$$E_{int} = \frac{p^2 m^2}{\pi} K_0(mR)\cos(\Delta\chi). \tag{3.4.1}$$

Here K_0 is the order zero modified Bessel function, p is a numerically found asymptotic decay constant and R is the large separation distance. (3.4.1) shows that the relative

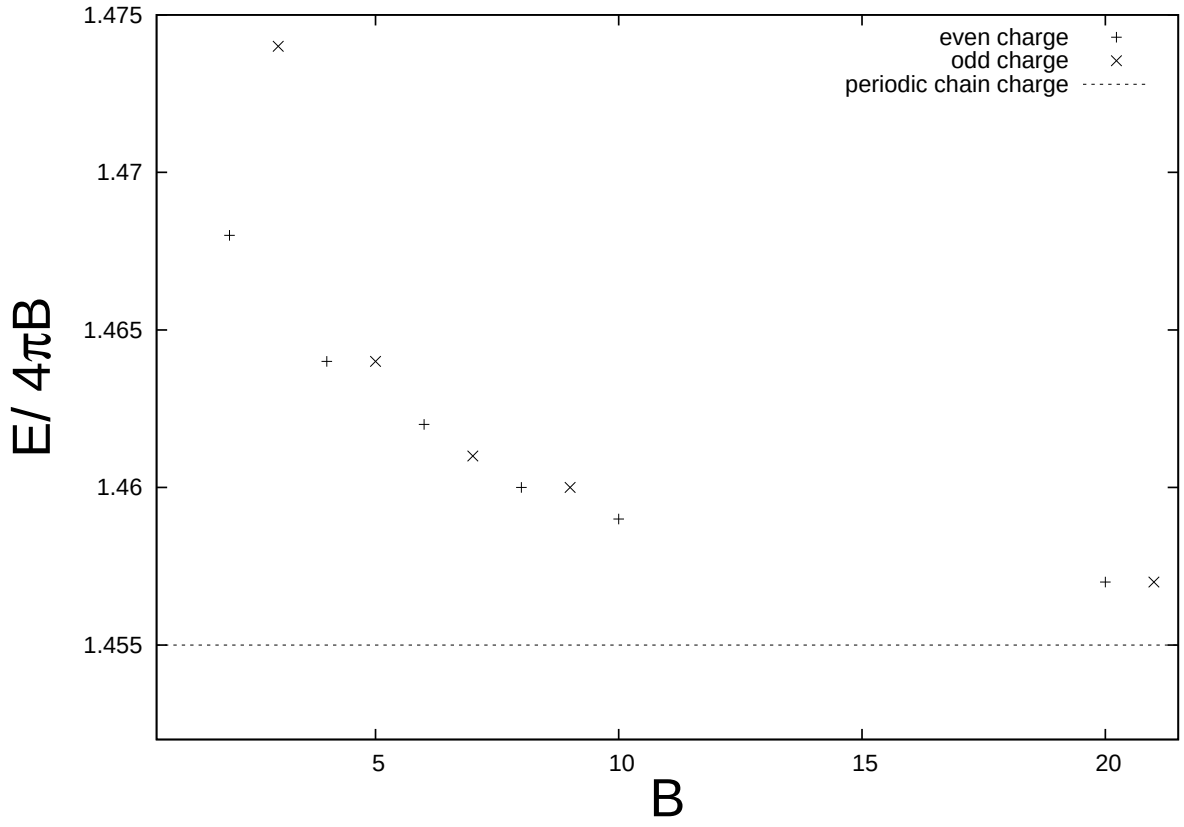

Figure 3.7: Plot of energy per-unit charge, in units of 4π, against the topological charge of the baby skyrmion chain.

phase, $\Delta\chi$, of two baby skyrmions dictates the type of interaction. For $\Delta\chi = 0$ the baby skyrmions repel, and for $\Delta\chi = \pi$ they attract. Hence to create a stable chain of interacting baby skyrmions we have to start with an anti-periodic chain of $B = 1$ baby skyrmions. To proceed the same numerical procedure as outlined above is implemented. Instead of imposing $\boldsymbol{\phi} = \mathbf{e}_3$ at the boundaries, we imposed periodic boundary conditions in the y-direction. We then vary the length of the periodic y-direction to find the minimum energy as shown in Figure 3.8. Due to the smaller lattice size than the infinite plane case $\Delta x = 0.08$ is used for a greater energy resolution.

This shows a minimum energy for a cell of periodic length $L = 8.56$ for $\kappa = 1$ and $m = \sqrt{0.1}$. The minimum energy for a baby skyrmion on a cylinder is found to be $E_{min} = 1.4549$, this energy is the dashed line plotted in Figure 3.7, which is

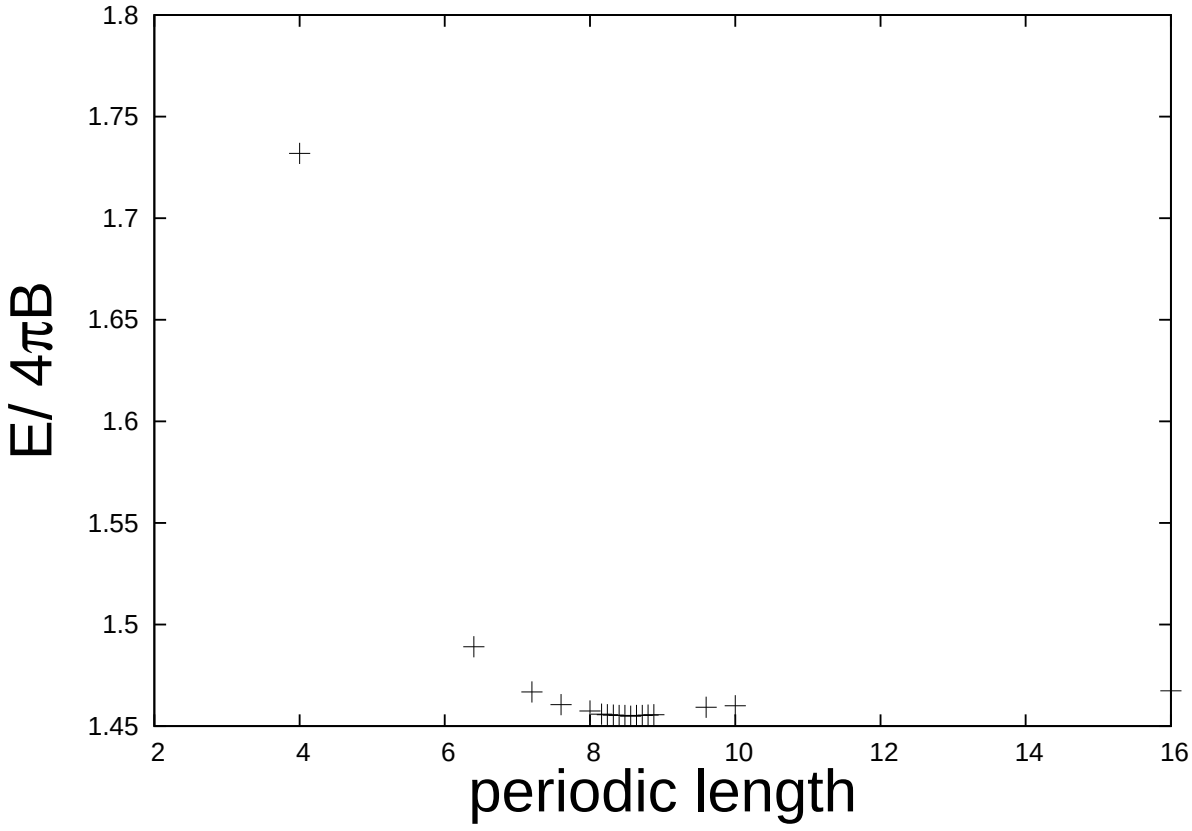

Figure 3.8: Plot of baby skyrmion chain energy per-unit charge, in units of 4π, for a varying periodic cell length, L.

consistent with the asymptotic of the curve in Figure 3.7.

3.5 Baby skyrmion on a torus

To discover the minimum energy per-unit topological charge of a baby skyrmion crystal we need to impose periodic boundary conditions. Hence the physical space is now a 2-torus, so

$$\boldsymbol{\phi} : \mathbb{T}^2 \to S^2. \tag{3.5.1}$$

It is already known that the topological charge density of the minimum energy configuration forms a hexagonal lattice [44]. Each hexagon hole effectively represents a charge of $B = 1/2$. For numerical simplicity it is easier to study a hexagonal configuration by working on a fundamental rectangular torus of size $L' \times \sqrt{3}L'$, as

in [45]. Note that the space is still discretized on a regular rectangular lattice. This fundamental torus has the geometry to contain eight hexagons, hence a $B = 4$ initial configuration is needed. To proceed we used the above algorithm to energetically minimise two $B = 2$ baby skyrmions, on a $L' \times \sqrt{3}L'$ bi-periodic lattice. The length L' is then varied to find how the minimum energy varies with cell size, giving figure 3.9.

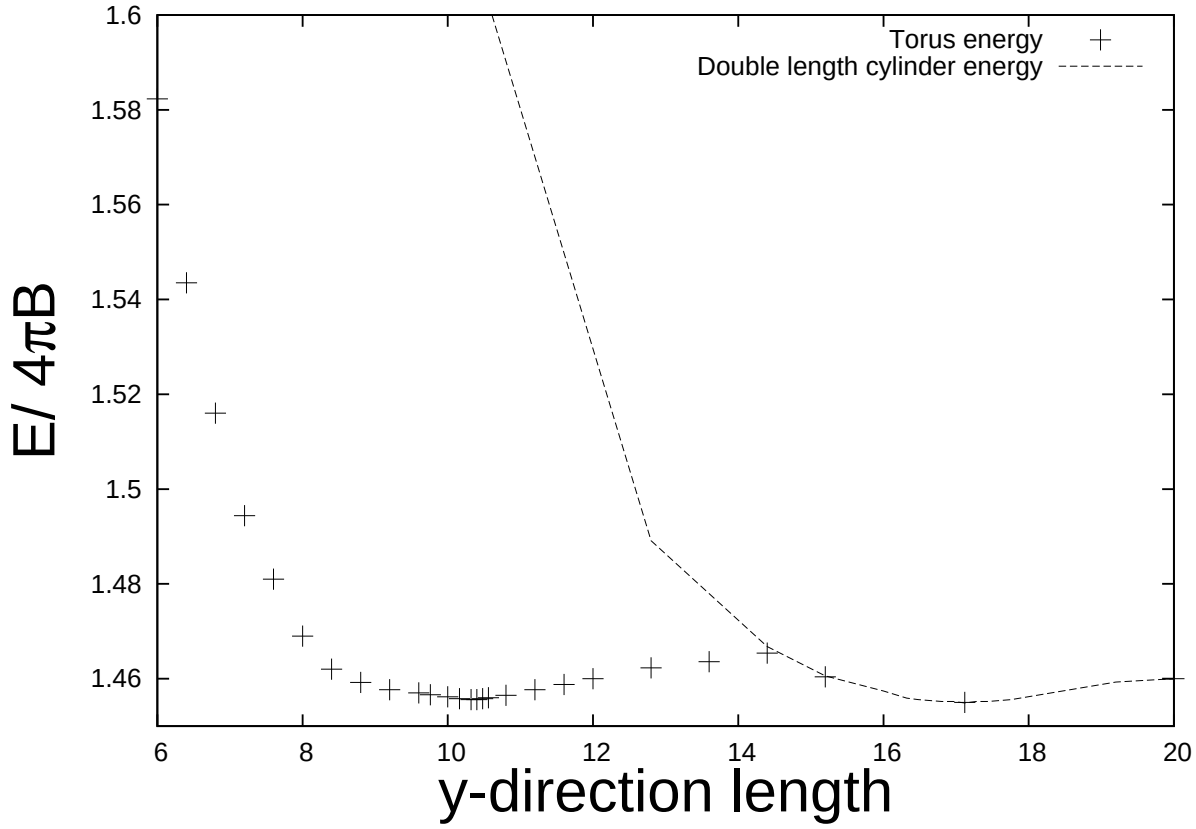

Figure 3.9: Plot of baby skyrmion chain and lattice energy per-unit topological charge, in units of 4π, for varying periodic cell lengths L and L'.

The result is that the natural unit cell size for a baby skyrmion lattice is a cell of size $L' = 10.4$, for $\kappa = 1$ and $m = \sqrt{0.1}$. Figure 3.9 also has the energy per-unit topological charge data for the cylinder case, where the periodic length is doubled to allow for a $B = 4$ unit cell. This shows that as the fundamental rectangle becomes large the baby skyrmion behaves as if it were on a cylinder. So the baby skyrmion configuration for increasing fundamental rectangle first starts off as a compressed

crystal, then a hexagonal crystal, then a deformed chain, then an energetically minimum chain and finally a single $B = 4$ baby skyrmion. One of the main points of interest of the torus case is that the minimum energy of a lattice, $E_{latt} = 1.4555$, and the minimum $B = 4$ infinite chain, $E_{chain} = 1.4549$, are well within 0.05%. This difference in energy is smaller than the numerical accuracy. So we cannot conclude which is the lower energy solution; only that the two configurations have very comparable energies.

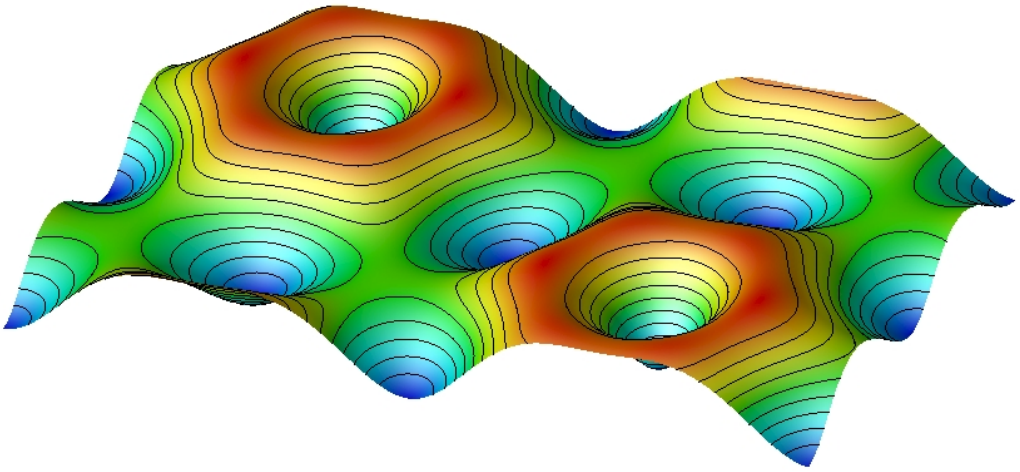

Figure 3.10: Two-dimensional plot of the topological charge density, j, of a $B = 4$ baby skyrmion on a torus.

3.6 Conclusion

We have presented new minimum energy solutions for multi-charge baby skyrmions. This discrepancy, between our solutions and the previously accepted solutions, is believed to be due to the extra computing power now available. This has allowed us to find lower energy solutions for $B \geq 5$. This has led to the proposal that baby skyrmion minimum energy configurations are chains. We are confident in this

result because of the smooth lowering of energy, per-unit topological charge, for increasing topological charge configurations. Also, the energy per-unit topological charge asymptotes to the periodic chain energy per-unit topological charge case. This shows the increasing stability as the topological charge of a chain grows.
The planar hexagonal lattice and the periodic chains minimum energies are too similar to be able to identify the preferred configuration. This energetic similarity, between the hexagonal lattice and the chain energies, is similar to the negligible difference between the commonly accepted $B = 2 + 2 + 2$ solution and the $B = 6$ chain solution. The energetic similarity between the $B = 2 + 2 + 2$ and the $B = 6$ chain is an exact analogue to the $(3 + 1)$-dimensional Skyrme model. In the Skyrme model it is found that the $B = 12$ solution can be either: a linear chain of three $B = 4$ skyrmions, or three $B = 4$ skyrmions each placed at a vertex of an equilateral triangle, [46]. These two configurations again have similar energies.

An interesting extension to this work would be to extend the numerical algorithms to higher orders. With the aim to confidently identify the minimum energy periodic space topological charge configuration. Also it would be interesting to see if similar chain solutions are also minimum energy solutions to the $(3+1)$-dimensional Skyrme model.

Chapter 4

Baby skyrmion stabilized by a vector meson.

4.1 Introduction.

As discussed in the previous chapter the baby skyrmion model can be motivated as a lower dimensional analogue of the full $(3+1)$-dimension Skyrme theory [7]. The Skyrme theory is a non-linear theory of pions, where the topological degree of the field is interpreted as the baryon number. The $(3+1)$-dimensional Skyrme theory is stable under Derricks theorem, [21], because its Lagrangian has a sigma term, which is quadratic in derivative, and a Skyrme term which is quartic in derivatives. It has been shown, [47], that if the Skyrme term is removed and the theory is coupled to a vector field using the charge density. Then there is still a stable topological charge one soliton solution. Numerically it has been shown that charge specific solutions of this modified model share qualitative features with those of the usual Skyrme theory. For topological charge one the modified theory also has spherically symmetric solutions [47]. Due to the extra computational intensity needed for larger topological charges this analysis has only been performed using the rational map

ansatz [20]. This constrains the system with a certain symmetry.

Here we are interested in a $(2+1)$-dimensional modified $O(3)$-sigma model. Unlike the baby skyrmion model this model does not have a Skyrme term. This model is stabilised by including a massive vector meson coupled to the topological charge density. We find that the charge specific solutions of this model are qualitatively similar to those of the baby skyrmion model and their energies are comparable. This is a justification of the symmetry ansatz used in the analysis of the $(3+1)$-dimensional Skyrmion coupled to a vector meson [48]. For clarity, in the remainder of this chapter, we shall refer to the baby skyrmion stabilised by a vector meson model simply as the vector meson model.

4.2 Baby skyrmion model stabilised by a vector meson.

Removing the Skyrme term from the baby skyrmion model and including a vector field gives a theory described by the Lagrangian density [1]

$$\begin{aligned} \mathcal{L}^{VM} &= \frac{1}{2}\partial_\mu \boldsymbol{\phi}\cdot\partial^\mu\boldsymbol{\phi} - m_\pi^2(1-\phi_3) \\ &- \frac{1}{4}(\partial_\mu\omega_\nu - \partial_\nu\omega_\mu)(\partial^\mu\omega^\nu - \partial^\nu\omega^\mu) + \frac{1}{2}m_\omega^2\omega_\mu\omega^\mu + g\omega_\mu j^\mu. \end{aligned} \tag{4.2.1}$$

Where we have defined the two masses m_π and m_ω which are the pion and vector field masses respectively. The vector field, ω_μ, is coupled to the topological charge current, j^μ, of $\boldsymbol{\phi}$ by a positive constant g. In this planar model the vector field, ω_μ, can be interpreted as the lower dimensional analogue of the vector field in the $(3+1)$-dimensional Skyrme theory coupled to a vector meson [48].

As in the baby skyrmion model, due to the finite energy criteria, $\boldsymbol{\phi}(r\to\infty) = (0,0,1)$ so the field is a map $\boldsymbol{\phi}:\mathbb{R}^2\cup\{\infty\}\sim S^2\to S^2$. This map belongs to the homotopy class $\pi_2(S^2)=\mathbb{Z}\ni B$ hence each field, $\boldsymbol{\phi}$, has an associated topological

degree B. Each field, $\boldsymbol{\phi}$, cannot be smoothly altered to have a new topological invariant. So the configuration spaces for separate B are not connected. We define the topological degree as the topological charge, B. The topological charge can be calculated from the conserved topological current,

$$j^{\mu} = -\frac{1}{8\pi}\epsilon^{\mu\alpha\beta}\boldsymbol{\phi}\cdot(\partial_{\alpha}\boldsymbol{\phi}\times\partial_{\beta}\boldsymbol{\phi}), \tag{4.2.2}$$

as

$$B = \int_{\mathbb{R}^2} j^0 d^2x. \tag{4.2.3}$$

This is found in a similar way as the topological charge density j, in the previous chapter. However, instead of an area form being pulled back by $\boldsymbol{\phi}(x)$ to $\mathbb{R}^2$, the normalised 2-form is pulled back by $\boldsymbol{\phi}(\boldsymbol{x},t)$ to $\mathbb{R}^2\times\mathbb{R}$.

Our research is concerned with static fields hence it is convenient to work with the static energy

$$\begin{aligned} E^{VM} &= \int_{\mathbb{R}^2}(\frac{1}{2}\partial_i\boldsymbol{\phi}\cdot\partial_i\boldsymbol{\phi} + m_{\pi}^2(1-\phi_3) \\ &- \frac{1}{2}(\partial_i\omega)^2 - \frac{1}{2}m_{\omega}^2\omega^2 + \frac{g\omega}{8\pi}\epsilon_{ij}\boldsymbol{\phi}\cdot(\partial_i\boldsymbol{\phi}\times\partial_j\boldsymbol{\phi}))d^2x. \end{aligned} \tag{4.2.4}$$

For static fields the spacial components of the topological current, (4.2.2), all equal zero, $j^i = 0$. j^i is the source for ω_i. So in the static limit there is no coupling with the spacial components of the vector field. For simplicity we have set $\omega_0 \equiv \omega$ and $\omega_i \equiv 0$ in (4.2.4). A point worth noting is that the vector field, ω, is constrained by its equation of motion. This stops the ω field from becoming very large and making the energy, (4.2.4), negative. In this chapter we shall denote the energy associated with the vector meson model as E^{VM}, and the energy associated with the normal-baby skyrmion model as E^{BS}. Varying the energy (4.2.4) gives the two

static field equations

$$\partial_i^2\boldsymbol{\phi} + m_\pi^2\mathbf{e}_3 + \frac{g}{4\pi}\epsilon_{ij}\partial_j\omega\boldsymbol{\phi}\times\partial_i\boldsymbol{\phi} + (\partial_i\boldsymbol{\phi}\cdot\partial_i\boldsymbol{\phi} - m_\pi^2\phi_3)\boldsymbol{\phi} = 0, \quad (4.2.5)$$

$$\partial_i^2\omega - m_\omega^2\omega + \frac{g}{8\pi}\epsilon_{ij}\boldsymbol{\phi}\cdot(\partial_i\boldsymbol{\phi}\times\partial_j\boldsymbol{\phi}) = 0. \quad (4.2.6)$$

If we multiply (4.2.6) by ω and substitute it into (4.2.4). Then after an integration by parts the energy can be rewritten as

$$E^{VM} = \int_{\mathbb{R}^2}\left(\frac{1}{2}\partial_i\boldsymbol{\phi}\cdot\partial_i\boldsymbol{\phi} + m_\pi^2(1-\phi_3) + \frac{g}{16\pi}\omega\epsilon_{i,j}\boldsymbol{\phi}\cdot(\partial_i\boldsymbol{\phi}\times\partial_j\boldsymbol{\phi})\right)d^2x. \quad (4.2.7)$$

To leading order we can approximate (4.2.6) by assuming ω varies negligibly when compared to $\boldsymbol{\phi}$, and also for large enough m_ω. Then neglecting the Laplacian term we find

$$\omega = \frac{g}{4\pi^2 m_\omega^2}\boldsymbol{\phi}\cdot(\partial_1\boldsymbol{\phi}\times\partial_2\boldsymbol{\phi}) + \mathcal{O}\left(\frac{\partial_i^2\omega}{m_\omega^2}\right).$$

This gives an approximate solution for ω which we can substitute into (4.2.7) giving

$$E^{VM} \backsimeq \int_{\mathbb{R}^2}\left(\frac{1}{2}\partial_i\boldsymbol{\phi}\cdot\partial_i\boldsymbol{\phi} + m_\pi^2(1-\phi_3) + \frac{g^2}{32\pi^2 m_\omega^2}|\partial_1\boldsymbol{\phi}\times\partial_2\boldsymbol{\phi}|^2\right)d^2x. \quad (4.2.8)$$

If we identify κ from the previous baby skyrmion chains chapter as

$$\kappa = \frac{g}{4\pi m_\omega},$$

we gain the static energy for the normal-baby skyrmion model. Therefore, for large m_ω, we expect this vector meson model to have similar topological charge specific solutions as the baby skyrmion model. We show this similarity numerically in the next section. So that we can compare this model directly with the previous baby skyrmion chapter we chose ${m_\pi}^2 = 0.1$ and $\kappa = 1$. We also chose the ratio of m_π/m_ω to be similar to the ratio used in the analysis of the $(3+1)$-dimensional skyrmion

coupled to a vector field [48], hence $m_\omega = 3/2$.

4.3 Soliton solutions.

4.3.1 Topological charge $B \leq 2$.

As discussed in the baby skyrmion chains chapter it is expected that the topological charges one and two minimum energy solution, of the vector meson model, will also be axially symmetric. Again using the hedgehog ansatz

$$\boldsymbol{\phi} = \big(\sin f(r)\cos B\theta, \sin f(r)\sin B\theta, \cos f(r)\big) \tag{4.3.1}$$

where r and θ are the polar coordinates, and a profile function, $f(r)$, which satisfies $f(0) = \pi$ and $f(\infty) = 0$. This gives a topologically non-trivial ansatz for the field $\boldsymbol{\phi}$. For the vector field, ω, we choose $\omega(r)$ with the boundary conditions $\omega'(r = 0) = 0$ and $\omega(\infty) = 0$. These conditions are required by regularity and the finite energy criteria. Using this ansatz we gain the energy as a function of r,

$$E^{VM} = \pi \int_0^\infty \left(f'^2 + \frac{B^2 \sin^2 f}{r^2} + 2m_\pi^2(1 - \cos^2 f) - \omega'^2 - m_\omega^2\omega^2 + \frac{gB\omega f' \sin f}{2\pi r} \right) r dr. \tag{4.3.2}$$

Varying this energy, (4.3.2), yields the axial partial differential equations

$$0 = f'' + \frac{f'}{r} - \frac{B^2 \sin f \cos f}{r^2} - m_\pi^2 \sin f + \frac{gB\omega' \sin f}{4\pi r}, \tag{4.3.3}$$

$$0 = \omega'' + \frac{\omega}{r} - m_\omega^2\omega + \frac{gBf' \sin f}{4\pi r}. \tag{4.3.4}$$

It is worth noting that, by symmetric criticality [49], we would have arrived at the same axial differential equations, (4.3.3) and (4.3.4), if we had substituted the ansatz (4.3.1) and the radial expression, $\omega(r)$, into (4.2.5) and (4.2.6).

We can solve (4.3.3) and (4.3.4) using a heat flow type method, where we numerically

gradient flow (4.3.3) and evolve (4.3.4) at the same time. For $B = 1$ we find $E_1^{VM} = 19.66$ where we have chosen $g = 20.83$. This is chosen so the vector meson model has the same energy as the topological charge one baby skyrmion, $E^{BS} = E^{VM}$. This energetic choice of g is slightly larger than that found in the previous analysis, $g = 4\pi m_\omega \kappa \approx 18.85$. This small difference is due to the approximation of the removal of the Laplacian term in (4.2.6). With the energetically chosen value of g Figure 4.1 shows that for $B = 1, 2$ the profile functions, $f(r)$, only slightly differs from those found in the normal baby skyrmion model. Also Figure 4.2 shows the form of the vector field, $\omega(r)$, which as expected is located about the topological charge density.

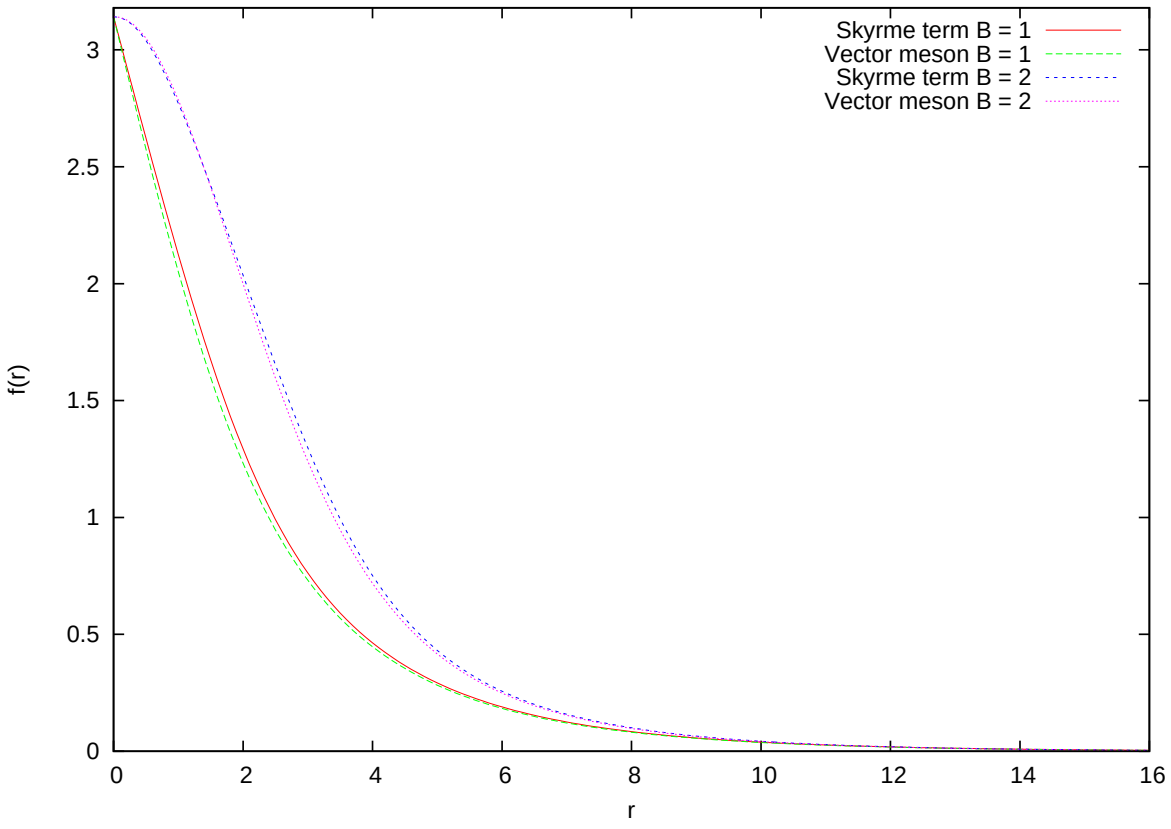

Figure 4.1: The profile functions, $f(r)$, of the usual baby skyrmion model compared to the vector meson model for $B = 1, 2$.

As discussed in the previous baby skyrmion chains chapter, for this choice of

potential the $B > 2$ minimum energy solutions are no longer axially symmetric. Therefore we expect the $B > 2$ vector meson model minimum energy solutions also not to be axially symmetric.

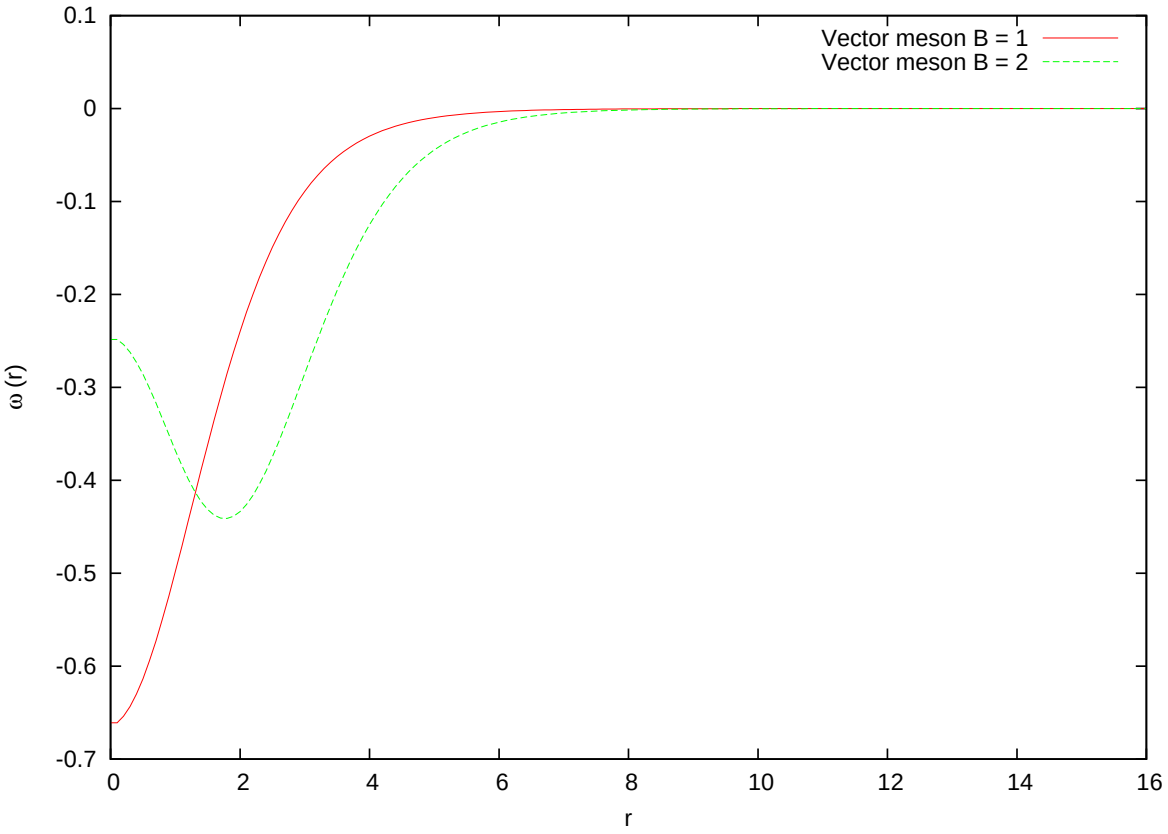

Figure 4.2: The vector fields, $\omega(r)$, for the axial $B = 1, 2$ vector meson model.

B	E^{BS}	E^{BS}/B	E^{VM}	E^{VM}/B
1	19.66	19.66	19.66	19.66
2	36.90	18.45	37.32	18.66
3	55.58	18.53	56.19	18.73
4	73.61	18.40	74.48	18.62

Table 4.1: Charge specific comparison of energy between the baby skyrmion model, E^{BS}, and the vector meson model, E^{VM}.

4.3.2 Topological charge $B > 2$.

To find potentially non-axially symmetric soliton solutions of the coupled partial differential equations (4.3.3) and (4.3.4), for $B > 2$, we perform the same heat

flow type minimisation as described above. The minimisation was performed on a two-dimensional lattice of 250×250 points, with spacing $\Delta x = 0.2$, using fourth order accurate derivatives. This lattice is found to be large enough to contain a soliton which can smoothly attain its vacuum value, without an energetic penalty. We can create topologically non-trivial initial conditions using the hedgehog ansatz (4.3.1). Which we then minimise to find the minimum energies in Table 4.1 and the, $1 \leqslant B \leqslant 4$, topological charge density plots, $j^0(\boldsymbol{x})$, in Figure 4.3. For this choice of g Table 4.1 shows that the charge specific energies of the two models are very similar. In Figure 4.3 the plots on the left side are the topological charge densities of the vector meson model; these are very similar to the topological charge densities of the baby skyrmion model shown on the right. These very similar plots, and the closely matching energies, show the remarkable similarity of the soliton solutions of the two models.

4.4 Symmetric potential.

The choice of the potential in the baby skyrmion model is not general. In [40] the authors proposed a new symmetric potential (4.4.1). This potential is invariant under the transformation $\phi_3 \mapsto -\phi_3$,

$$V(\boldsymbol{\phi}) = \frac{1}{2}(1 - \phi_3^2). \tag{4.4.1}$$

This choice of potential, (4.4.1), has no contribution to the energy at the origin, $\boldsymbol{\phi} = (0, 0, -1)$, of the axially symmetric soliton. Baby skyrmions with this potential are all axially symmetric. For $B > 1$ the maximum charge density is located on a ring of constant radius [40]. Using the axial Hedgehog ansatz defined earlier we can calculate the axially symmetric minimum energies for this potential. For both the baby skyrmion model and the vector meson model we find the charge specific energies in Table 4.2. Even though we have kept $g = 20.83$, from the previous

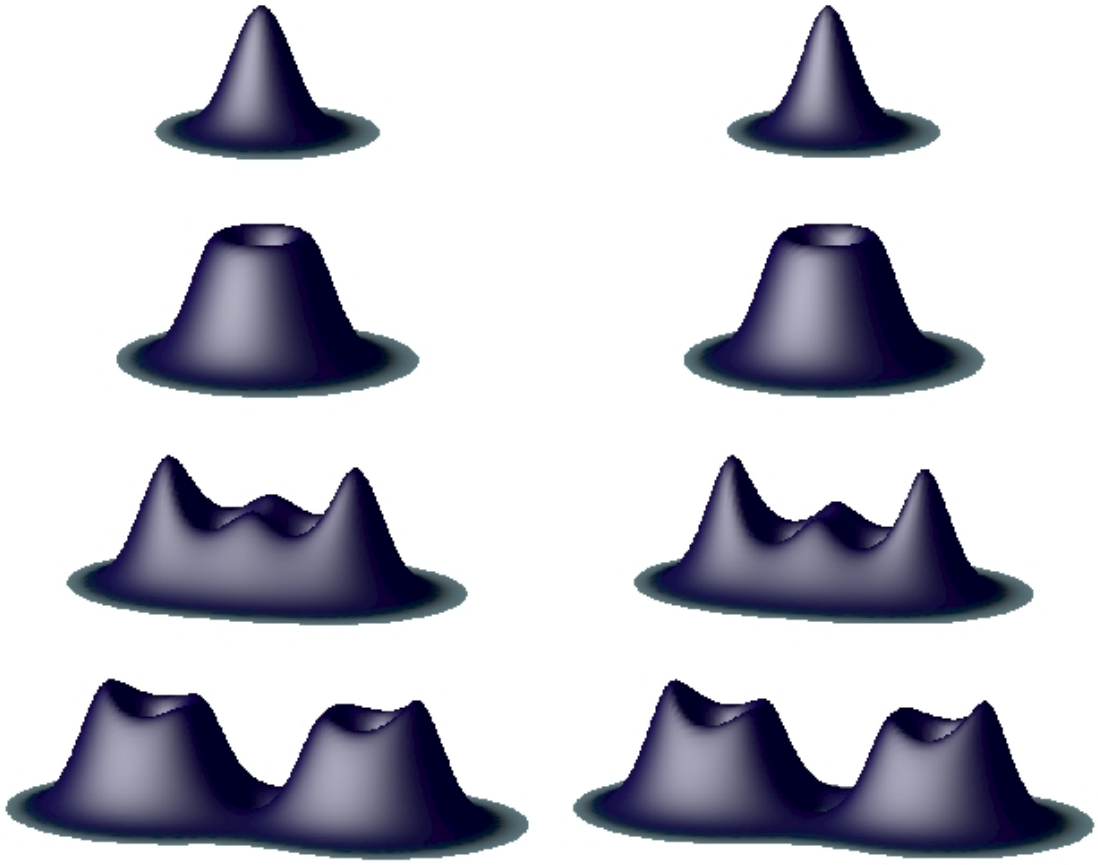

Figure 4.3: Topological charge density plots for $1 \leqslant B \leqslant 4$ from top to bottom. On the left are minimum energy solutions of the baby skyrmion model and on the right the vector meson model.

non-symmetric potential model, the energies are still very comparable between the baby skyrmion and vector meson model. Also as shown in Figure 4.4 the charge specific profile functions, $f(r)$, are very similar between the vector meson model and the baby skyrmion model, for this symmetric potential (4.4.1). Similar to the baby skyrmion model, with a symmetric potential [40], the vector meson model also has its maximum charge density located on a ring. This is shown by the minimum value of ω in Figure 4.5. For all the discussed models Tables 4.1 and 4.2 show that we have found bound states. We can verify that the symmetric solutions of the vector meson model, with the symmetric potential (4.4.1), are minimum energy solutions by minimising perturbed $1 \leqslant B \leqslant 4$ solution of the Hedgehog ansatz (4.3.1). We

used a 2-dimensional lattice as described above, but with the symmetric potential (4.4.1), and again we found the same axial results.

B	E^{BS}	E^{BS}/B	E^{VM}	E^{VM}/B
1	18.18	18.18	18.30	18.30
2	32.91	16.46	33.28	16.64
3	48.29	16.10	48.82	16.27
4	63.89	15.97	64.58	16.15

Table 4.2: Charge specific comparison of energy between the baby skyrmion model, E^{BS}, and the vector meson model, E^{VM}, with the symmetric potential (4.4.1).

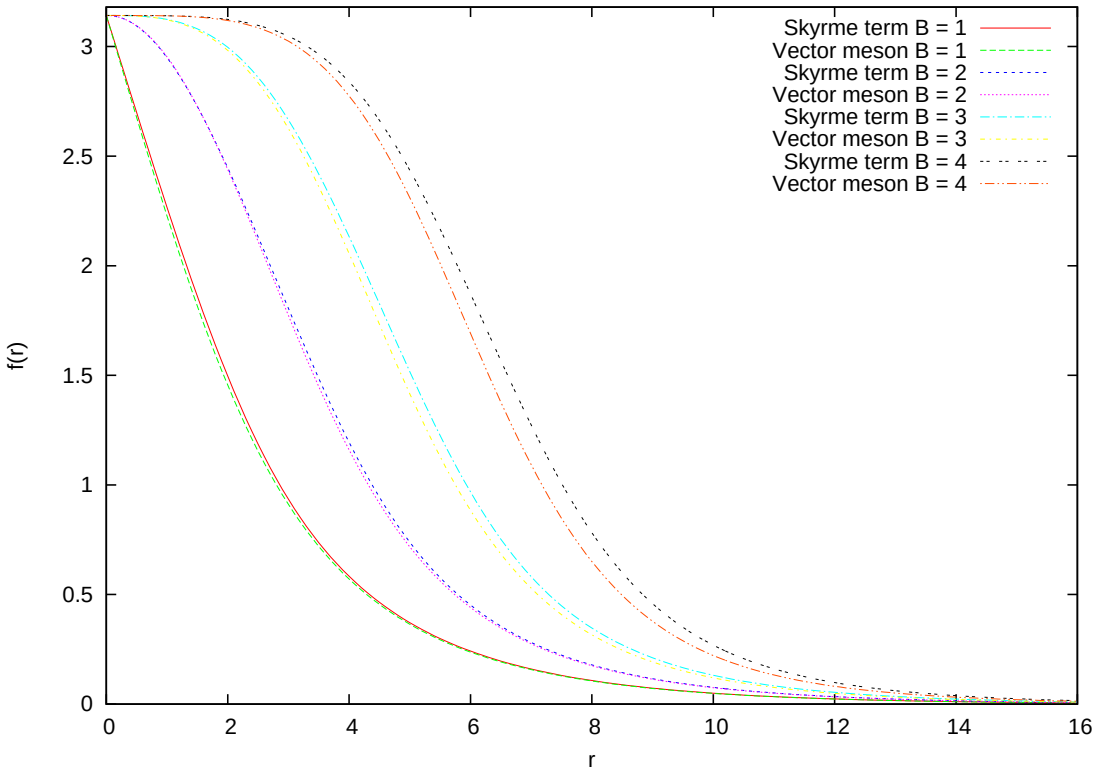

Figure 4.4: Plots of the profile functions, $f(r)$, of the baby skyrmion model and the vector meson model with the symmetric potential (4.4.1). For $1 \leq B \leq 4$.

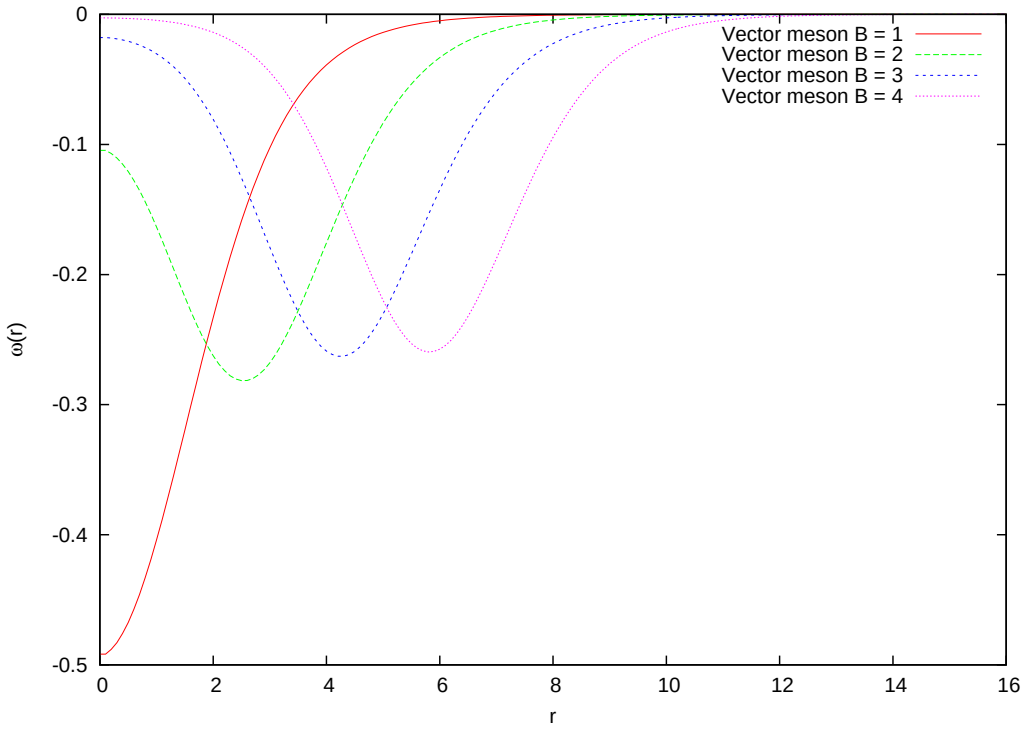

Figure 4.5: Plots of the vector field, $\omega(r)$, of the vector meson model with the symmetric potential (4.4.1). For $1 \leq B \leq 4$.

4.5 Conclusion.

In this chapter we have numerically presented the remarkable similarities between the baby skyrmion model and the new vector meson model. This model is stabilised by coupling to a vector meson via the topological charge density. For topological charges $1 \leq B \leq 4$ we have shown that the two models have very similar, topological charge densities. We have also shown that their energies are very similar. We also presented this similarity for two different choices of potentials, where the potential has a great effect on the form of the solutions. We have analytically understood this similarity using a derivative expansion of the static vector meson field equation. On substitution into the energy density this gives a Skyrme-term as in the baby skyrmion model. This analysis is a lower dimensional analogue justification of the rational map ansatz [20] used in [48].

Chapter 5

Hopf solitons.

5.1 Motivation.

The research presented in this chapter is my own results from part of an on going collaboration with Dr. D. Harland and Prof. P. M. Sutcliffe. The collaboration is concerned with formulating a string ansatz approximation for Hopfions in the Skyrme-Faddeev model. We intend for this ansatz to have two degrees of freedom, the string location and a continuous phase parametrized along the length of the string. We aim for this reduced degrees of freedom model to be simpler than the full Skyrme-Faddeev model and not present the relative computational intensity. The cross-sections of Hopfion strings, in the normal Skyrme-Faddeev model, are not symmetric and decay as a power. The string ansatz assumes the Hopfions are actually compactons with symmetric cross-sections. We have added a potential term to the Skyrme-Faddeev model to make it have a stronger correspondence with the string model. Doing this increases the similarities between the two models, where as we increase the coupling the Hopfions become increasingly localized in space. This also reduces the strings self interaction. This research is still on going.

5.2 The Skyrme-Faddeev model.

The Skyrme-Faddeev model is a (3+1)-dimension $O(3)$-sigma model [54] modified by including a quartic term. This quartic term is known as the Skyrme term and is required to provide a scale for Derricks theorem, [21], in 3-spacial dimensions. The theory is described by the Lagrangian

$$L = \frac{1}{32\pi^2\sqrt{2}} \int \left(\partial_\mu \boldsymbol{\phi} \cdot \partial^\mu \boldsymbol{\phi} - \frac{1}{2} (\partial_\mu \boldsymbol{\phi} \times \partial_\nu \boldsymbol{\phi}) \cdot (\partial^\mu \boldsymbol{\phi} \times \partial^\nu \boldsymbol{\phi}) - 2m^2 V(|\boldsymbol{\phi}|) \right) d^3x. \tag{5.2.1}$$

The field, $\boldsymbol{\phi}$, is a three component unit vector, $\boldsymbol{\phi} = (\phi_1, \phi_2, \phi_3)$, and is constrained to $S^2_{\boldsymbol{\phi}} = \{\boldsymbol{\phi} | \boldsymbol{\phi} \cdot \boldsymbol{\phi} = 1\}$. At fixed time $\boldsymbol{\phi}$ is the map $\boldsymbol{\phi} : \mathbb{R}^3 \to S^2_\phi$. This model is usually studied with the parameter $m = 0$, [50–54], which we shall discuss now, and we shall discus $m > 0$ later. For finite energy solutions of (5.2.1) the field, $\boldsymbol{\phi}$, must tend to a constant value at spatial infinity, which we select to be $\boldsymbol{\phi}(t, r = \infty) = (0, 0, 1) = \mathbf{e}_3$ for all time, t. This allows a one-point compactification of the domain, $\mathbb{R}^3 \cup \{0\} \sim S^3$. So static, finite energy, solutions are $\boldsymbol{\phi} : S^3 \to S^2_\phi$ where S^3 can be interpreted as a fibration of S^1 over S^2_ϕ. This map, $\boldsymbol{\phi}$, belongs to an equivalence class characterised by the homotopy group $\pi_3(S^2_\phi) = \mathbb{Z}$. This shows that there is an integer topological invariant associated with $\boldsymbol{\phi}$, known as the Hopf invariant. In this case we will refer to the Hopf invariant as the topological charge Q.

The charge associated with a Hopf projection can be found by defining an area form ω, which is a generator of the cohomology group $H^2(S^2)$ on the target S^2. The smooth map $\boldsymbol{\phi} : S^3 \to S^2_\phi$, has an induced pull-back of the de Rham cohomology group $\boldsymbol{\phi}^* : H^2(S^2) \to H^2(S^3)$. This pull-back maps closed forms to closed forms and exact forms to exact forms [55]. We can now define $g = \boldsymbol{\phi}^* \omega$, which is the pull-back of the area form, ω, by $\boldsymbol{\phi}$. Due to the second cohomology group of the three sphere being trivial, $H^2(S^3) = 0$, all closed forms on S^3 are exact forms. Therefore, we can now re-define the exact form g by the 1-form a as $g = da$. Therefore we can express

the topological charge, Q, as

$$Q = \frac{1}{4\pi} \int_{S^3} g \wedge a. \tag{5.2.2}$$

This is the integral of a Chern-Simons 3-form over S^3.

Unlike most other topological solitons, such as Skyrmions and vortices, the dimensions of the domain and the target space are not equal. Therefore the topological charge is not equal to the degree of $\boldsymbol{\phi}$. Also the topological charge cannot be expressed in the domain as a local density. This non-local definition of the topological charge, (5.2.2), is not particularly useful in this thesis. But the topological charge of $\boldsymbol{\phi}$ can also be found as the linking number of loops in the domain. These are formed as preimages of two distinct points on the target space. For example if we define the two curves C_p and C_q as the preimages of the points $\mathbf{p}$ and $\mathbf{q}$. Then if we choose a smooth surface D, with a boundary C_p, then the linking is defined as

$$\text{link}(C_p, C_q) = \sum_{D \cap C_q} \pm 1,$$

where the $\pm$ refers to the relative orientations of D and C_q. This definition of the topological invariant can be shown to be the same as (5.2.2), [56]. There is a well known lower bound on the energy, [57–59], which is based on an involved argument using Sobolev-type inequalities,

$$E \geq c\, Q^{3/4} \text{ where } c = \left(\frac{3}{16}\right)^{3/8}. \tag{5.2.3}$$

The fractional power of (5.2.3) is widely accepted. But the value of c might not be optimal. Ward, [57], was motivated by his study of the Skyrme-Faddeev theory on a unit three-sphere to propose that $c = 1$ might be a more optimal value.

The Hopfion location cannot be defined as the position of maximum local topological charge density, as in most topological soliton systems. Instead it is commonly chosen

to be the curve $C = \boldsymbol{\phi}^{-1}(0, 0, -1) \equiv \boldsymbol{\phi}^{-1}\mathbf{e}_{-3}$, which is the antipodal value to the boundary vacuum value.

Over the years there have been many extensive and detailed investigations into the static minimum energy solutions of (5.2.1), [50, 52–54, 60, 61]. For charges one to seven it is believed their respective global minimum energy solutions have all been identified. It is known for topological charges one to three that the minimum energy solutions have a planar loop position curve. Topological charges five and six have the minimum energy solutions of two linked Hopfions. For topological charge seven the minimum energy location curve is a trefoil knot. In [51] Sutcliffe devised a new knotted rational map ansatz as initial conditions. These initial conditions were then energetically minimised to give new minimum energy solution candidates for a large class of topological charges. We shall be describing and making use of this technique later.

5.3 $m > 0$.

The actual model of interest here is a modification of the usual Skyrme-Faddeev model. It is modified by an additional coupling to a potential term, so $m > 0$ in (5.2.1) and

$$V(\boldsymbol{\phi}) = (1 - \phi_3). \tag{5.3.1}$$

This choice of potential, (5.3.1), is not general but is one of the simplest choices. If we restrict ourself to the plane this model reduces to the old Baby Skyrmion model. Also this potential, (5.3.1), meets the finite energy criteria for the chosen boundary condition; where the single vacuum of $V(\boldsymbol{\phi})$ is also the chosen boundary value. This potential, (5.3.1), increases the energy density along the location of the Hopfion. This is because the location curve, $C = \boldsymbol{\phi}^{-1}(0, 0, -1)$, corresponds to the maximum of the potential (5.3.1). Therefore we expect the Hopfion location curve to become smaller in length for increasing m. We also expect the Hopfion string to become

finer with increasing m; as it is analogous with the Baby Skyrmion model. This is best understood by an asymptotic analysis where we approximate the field for large r as

$$\boldsymbol{\phi} = (\epsilon_1, \epsilon_2, 1 - \epsilon_1^2 - \epsilon_2^2) + \mathcal{O}(\epsilon_a^3),$$

where $a \in (0, 1)$. For large r we know that, due to finite energy criteria, $|\partial_i \epsilon_a| < 1$ therefore the energy density associated with (5.2.1) becomes

$$\mathcal{E} = (\partial_i \epsilon_a)^2 + 2m^2 \epsilon_a^2 + \mathcal{O}\left((\partial_i \epsilon_a)^4\right).$$

Where ϵ_a is a solution of the partial differential equation

$$(\Delta - 2m^2)\epsilon_a = 0. \tag{5.3.2}$$

Separating ϵ_a into radial and angular components as $\epsilon_a = r^{-\frac{1}{2}} R_a(r)\Theta_a(\theta, \psi)$. Where $R_a(r)$ is a purely radial function, Θ_a is a spherical harmonic ($\nabla_{s^2}\Theta_a = -\lambda(\lambda+1)\Theta_a$) and (r, θ, ψ) are the usual spherical polar coordinates. Then solving (5.3.2) we gain an asymptotic approximation for $R_a(r >> 1)$,

$$R_a(r >> 1) \sim C_a \sqrt{\frac{\pi}{2\sqrt{2}mr}} e^{-\sqrt{2}mr} \left(1 + \mathcal{O}\left(\frac{1}{\sqrt{2}mr}\right)\right).$$

Where C_a is a constant of integration. This shows that Hopfions become increasingly exponentially located as the coupling, m, increases. Hence the Hopfions in this massive theory will have Yukawa type asymptotic tails.

5.4 Static solutions.

It is already well known that charged Hopfions can be knotted objects, [50–54,60,61]. One of the most effective ways to create non-trivial knotted initial conditions, to be minimised, is to use the rational map ansatz technique described in [51]. Here the

author used a degree one spherically equivariant map to compactifiy $\mathbb{R}^3 \to S^3_{Z_1,Z_0} \subset \mathbb{C}^2$ by

$$(Z_1, Z_0) = \left(\frac{(x_1 + ix_2)}{r} \sin f, \cos f + \frac{ix_3}{r} \sin f \right), \tag{5.4.1}$$

where $f(0) = \pi$, $f(\infty) = 0$ and

$$S^3_{Z_1,Z_0} \cong \{(Z_1, Z_0) \in \mathbb{C}^2 \mid |Z_1|^2 + |Z_0|^2 = 1\}. \tag{5.4.2}$$

Using these complex coordinates an (a, b)-torus knot can be described as the intersection of a complex curve $q(Z_1, Z_0)$ with a unit three-sphere [62]. Hence we can formulate the rational map ansatz

$$W = \frac{p(Z_1, Z_0)}{q(Z_1, Z_0)}, \tag{5.4.3}$$

where p, q have no common roots. This is a map $W : S^3 \to \mathbb{CP}^1$. We can also notice that the stereographic projection, W, of $S^2_\phi = \{\boldsymbol{\phi} \mid \boldsymbol{\phi} \cdot \boldsymbol{\phi} = 1\}$ also maps to $\mathbb{CP}^1$ as,

$$W = \frac{\phi_1 + i\phi_2}{1 + \phi_3}. \tag{5.4.4}$$

Therefore, as shown in Figure 5.1, the inverse stereographic projection of the curve $q = 0$ produces a $\phi_3 = -1$ closed curve in $\mathbb{R}^3$. The asymptotic value of p in the rational map ansatz (5.4.3) is used to fix the boundary conditions of $\boldsymbol{\phi}$. Therefore, we need $p(r)|_{r\to\infty} = 0$ so the inverse stereographic projection gives $\boldsymbol{\phi} = (0, 0, 1)$ at the spacial boundary of $\mathbb{R}^3$.

Therefore an initial condition for a Hopfion, with a position curve of an (a, b)-torus knot, can be formed by the rational map ansatz

$$W = \frac{{Z_1}^\alpha {Z_0}^\beta}{{Z_1}^a + {Z_0}^b} \tag{5.4.5}$$

where $\alpha \in \{x > 0 | x \in \mathbb{Z}\}$ and $\beta \in \{x \geqslant 0 | x \in \mathbb{Z}\}$. This gives a closed curve that wraps a and b times about the two circumferences of a torus, [62]. The topological

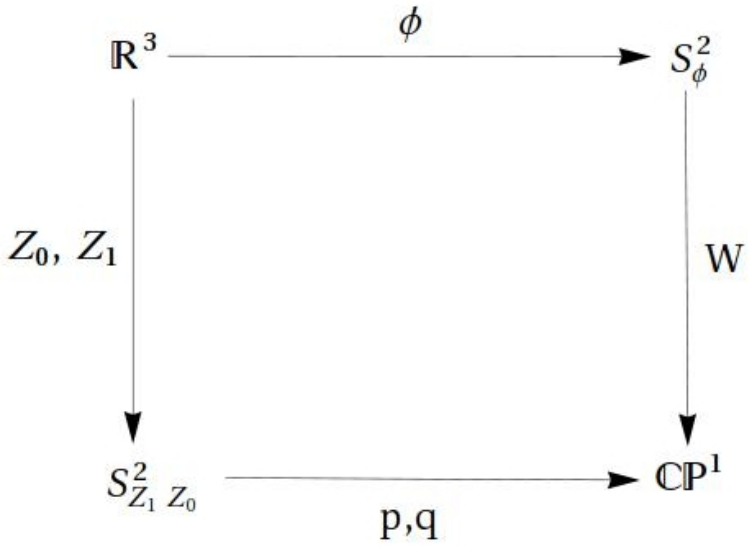

Figure 5.1: Commutative maps.

charge associated with this ansatz is most easily found by extending the map (5.4.1) to be

$$(p, q) : \mathbb{B}^4 \in \mathbb{C}^2 \to \mathbb{C}^2. \tag{5.4.6}$$

This extension is achieved by altering the constraint for $S^3_{Z_1,Z_0}$ to $|Z_1|^2 + |Z_0|^2 \leq 1$ giving a $\mathbb{B}^4$. This produces a map between spaces of equal dimensions, with $\deg[(p, q)] = Q$. The topological degree of (p, q) can then be found by counting the number of preimages of a point on $S^2_{Z_1,Z_0}$. Also, the map (p, q) being holomorphic means orientation is preserved locally. Hence the Jacobian is positive everywhere (Cauchy-Riemann), so all the preimages of a point occur with positive multiplicity. Therefore choosing a general point, $(a, 0) \in \mathbb{C}^2$, the Hopf invariant of (5.4.5) is given by the number of solutions of $({Z_1}^\alpha {Z_0}^\beta, {Z_1}^a + {Z_0}^b) = (a, 0)$. This can be shown to have

$$Q = \alpha b + \beta a \tag{5.4.7}$$

solutions [51].

This approach not only produces a non-trivial knotted location curve with an analytically known topological charge; it also gives a smooth field with the correct

boundary conditions.

To find static Hopf solitons we set $\dot{\boldsymbol{\phi}} = 0$ in the Skyrme term of (5.2.1). This gives a non-relativistic theory which has the same static equations of motions as the those derived from (5.2.1). This greatly simplifies the corresponding equations of motion by removing a numerically cumbersome matrix inversion. It also still facilitates time evolution by the second order dynamics derived from the the sigma term. The non-relativistic equation of motion can then be numerically evolved on a discrete lattice using a fourth-order derivative approximation. We also need an additional Lagrangian multiplier, λ, to constrain $\boldsymbol{\phi}$ to take its value on $S^2_{\boldsymbol{\phi}}$. If we periodically remove kinetic energy the potential energy will also become minimised; this will yield minimum energy static solutions. This minimisation technique produces static solutions and uses much less CPU time when compared to other similar minimisation algorithms. A numerical grid of $250 \times 250 \times 250$ points, with $\Delta x = 0.08$, was found to be large enough to contain the exponentially located Hopfion. On this lattice the Hopfion can smoothly attain the vacuum value at the boundary without a noticeable expense of energy. This lattice is also fine enough not to lose the fundamental topology. The definition of the position of a Hopf soliton is sensible, but not useful for display purposes. Therefore, all the images of Hopf solitons in this chapter are plots of an isosurface of the preimage of the curve $\phi_3 = -0.85$ in the domain. This gives a surface that is a fine tube in the physical space and produces much clearer images. To show the linking number we also need to plot the preimage of a second loop, but there is no unique loop to choose. In all the plots shown we generate general loops on the target space by choosing a point, $\mathbf{p} = (\sqrt{1-\mu^2}, 0, \mu)$, on $S^2_{\boldsymbol{\phi}}$. We then find the distance on the surface of $S^2_{\boldsymbol{\phi}}$ between $\mathbf{p}$ and $\boldsymbol{\phi}$. This distance is then normalised by the distance between $\mathbf{p}$ and the south pole of $S^2_{\boldsymbol{\phi}}$, $\mathbf{e}_{-3}$, as

$$\mathrm{dist}(\mathbf{p}, \boldsymbol{\phi}) = \frac{\cos^{-1}(\mathbf{p} \cdot \boldsymbol{\phi})}{\cos^{-1}(\mathbf{p} \cdot \mathbf{e}_{-3})}.$$

This gives many loops of constant radius on $S^2_{\boldsymbol{\phi}}$. The preimages, of these loops, are tubes of varying thickness in the domain. Also, an isosurface of unitary value is known to intersect with the position curve of a Hopf soliton. Throughout this chapter we will choose $\mu = -0.9$ which is an arbitrary choice for aesthetics.

5.4.1 $Q \leqslant 4$ trivial knots.

A Hopfion initial condition, where the position curve is contained completely on a plane, can be formed by the rational map ansatz

$$W = \frac{Z_1^n}{Z_0^p}. \tag{5.4.8}$$

We refer to a Hopfion location curve of this configuration as $A_{n,p}$. This configuration has topological charge $Q = np$ [51], which again can be shown by counting pre-images as shown previously. So if we set $n = p = 1$ in (5.4.8) this gives the initial condition of a topological charge one Hopf soliton which is located along a planar loop. Using this initial condition, and the above described minimisation procedure, we can find the minimum energy configurations for $m = (0, 1, 2, 4, 5)$ for a topological charge one Hopfion as shown in Figure 5.2.

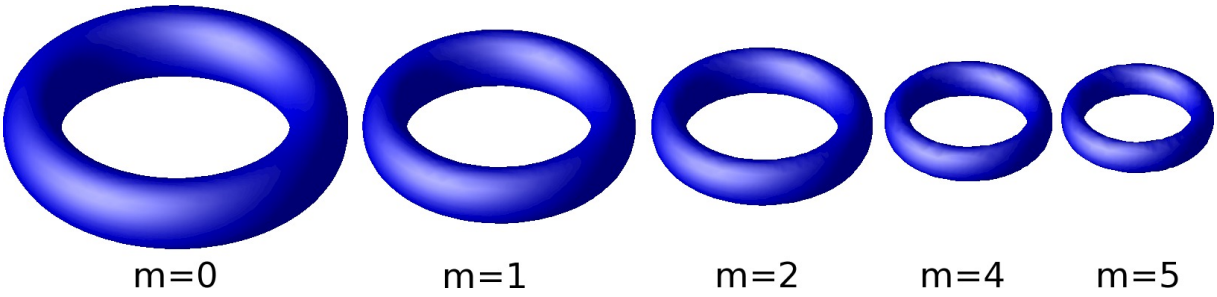

Figure 5.2: Minimum energy topological charge one Hopfions. Of mass $m = (0, 1, 2, 4, 5)$, all on the same scale.

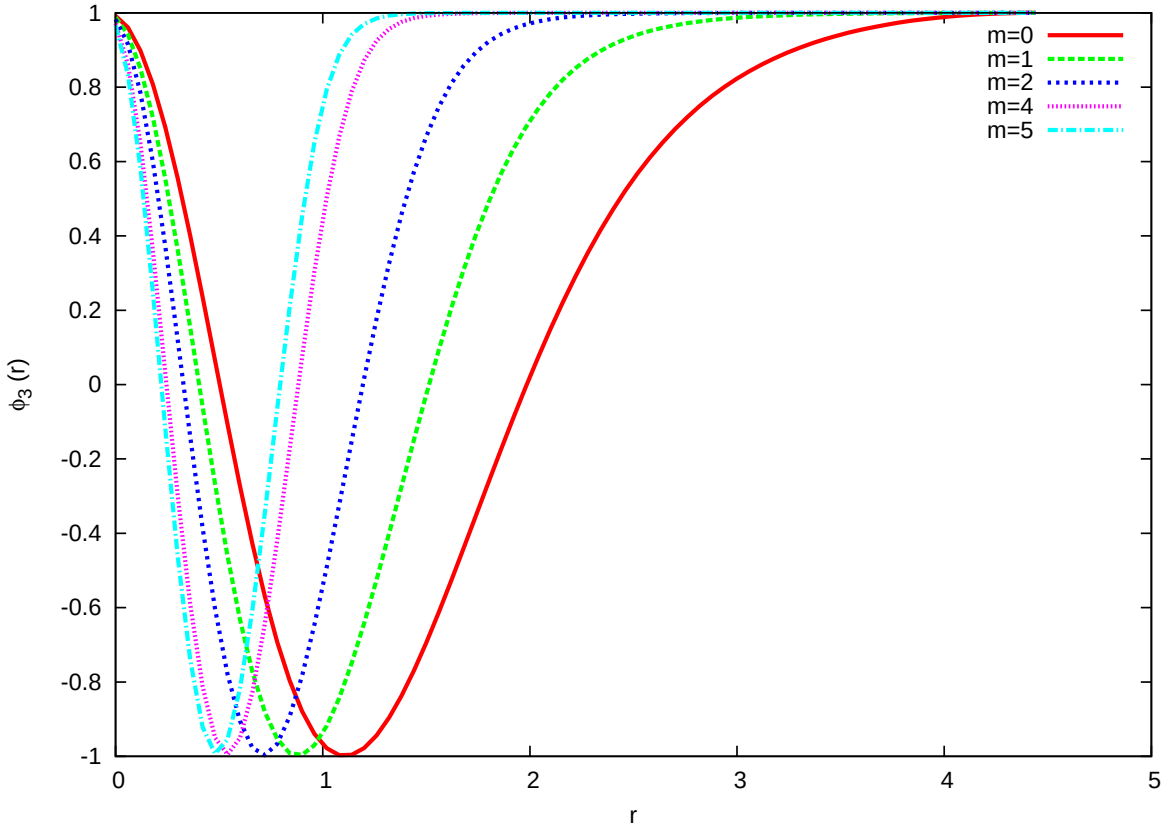

Figure 5.3: ϕ_3 for masses $m = 0, 1, 2, 4, 5$.

Mass, m	E
0	1.236
1	1.421
2	1.668
4	2.017
5	2.170

Table 5.1: Minimum energies for, $m = (0, 1, 2, 4, 5)$, topological charge one Hopfions.

Figure 5.2 shows as expected that the larger m is the smaller the Hopfion is. This is due to the potential term creating an energy penalty where $\boldsymbol{\phi} = (0, 0, -1)$, which corresponds to the maximum value for the potential. Thus the minimum energy Hopfion location loop becomes smaller with growing m. The energy for $m = 0$ is 1.236, this is within 2% of the previously accepted result [51]. This similarity is a nice validation of our numerical procedure. The small difference can be attributed to the difference in lattice spacing between our algorithm and the one used by the author. As shown in Figure 5.3 for larger values of mass the field ϕ_3 is increasingly

symmetric about the Hopfion location. Due to this we have decided to perform the remaining analysis with the relatively large $m = 5$. This choice of coupling is arbitrary, we could have chosen $m > 5$; but this choice gives sharply located Hopfions and is still large enough so the topology is not lost by the numerical lattice. We find a minimum energy $Q = 1$ Hopfion to be $E_1 = 2.17$.
Using (5.4.8) with $(n, p) = (2, 1)$ this again gives a planar loop Hopfion location but with topological charge $Q = 2$. Minimising this configuration we find the minimum energy $E_2 = 3.45$, with a planar Hopfion location curve. We can construct a $Q = 3$ Hopfion by setting $(n = 3, p = 1)$ in (5.4.8) or $(\alpha = \beta = b = 1, a = 2)$ in (5.4.5). The latter configuration produces a Hopfion which is located along an unknotted twisted loop. Minimisation of these two configurations produces the same configurations with the same energy, $E_3 = 4.74$, located on a twisted unknotted loop.

A topological charge $Q = 4$ Hopfion initial condition can be made using (5.4.5) with either $(\alpha = a = 2, \beta = b = 1)$ or $(\alpha = a = 4, b = 1, \beta = 0)$. This gives Hopfion location curves $K_{2,1}$ and $K_{4,1}$ respectively. Minimising both of these configurations give a $\tilde{A}_{4,1}$ (twisted $A_{4,1}$) Hopfion location curve, with energy $E_4 = 6.051$. We can also generate $Q = 4$ axial initial conditions using (5.4.8) with $(n = p = 2)$ and $(n = 4, p = 1)$. This gives $A_{2,2}$ and $A_{4,1}$ planar curves respectively. Minimisation of the $A_{2,2}$ configuration remains as an $A_{2,2}$, with an energy $\sim 0.6\%$ larger than the $\tilde{A}_{4,1}$. This is within numerical accuracy of our minimisation scheme. Therefore we are not able to define which of these two configuration is the lower energy. The $A_{4,1}$ configuration also minimises to a planar curve described by $A_{4,1}$. This seems to show that twisting the loop slightly reduces the energy. The $Q = 4$ planar loops are most likely long lived saddle point solutions, preserved by symmetry.

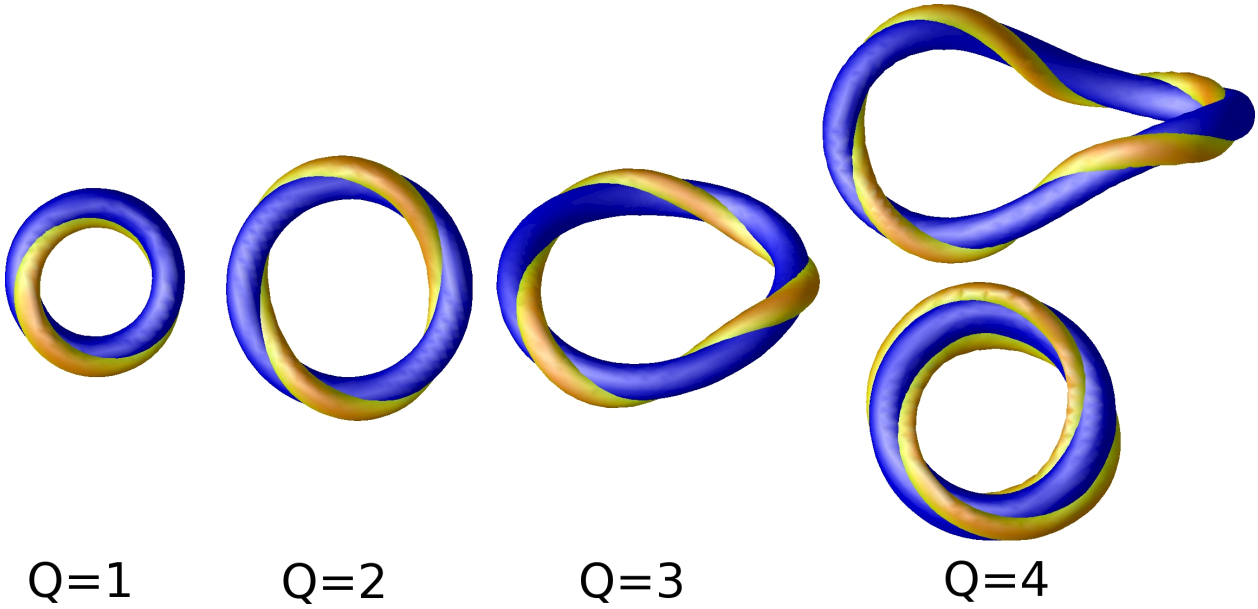

Figure 5.4: Minimum energies for $m = 5$, Hopfions.

5.4.2 $Q \geqslant 5$ knotted/linked Hopfions.

For a select few simulations Figure 5.5 and 5.6 show a plot of minimum energy Hopfion locations. Also Figure 5.5 and 5.6 show the linking of the initial rational map ansatz and the linking of the corresponding minimum energy Hopfion curve. For topological charges $Q \leqslant 4$, both in the massive case and in the normal massless case, the Hopfion location curves are all found to be unknot solutions. For topological charges $Q \geqslant 5$ we find the minimum energy Hopfions have either a linked or knotted location curves, as shown in Figure 5.6. The minimum energy solutions presented have very similar qualitative features with the massless model [51]. The minimum energy Hopfion location curves for each charge sector have comparable linking form hence, due to the computational intensity, we have restricted our analysis to the presented charges.

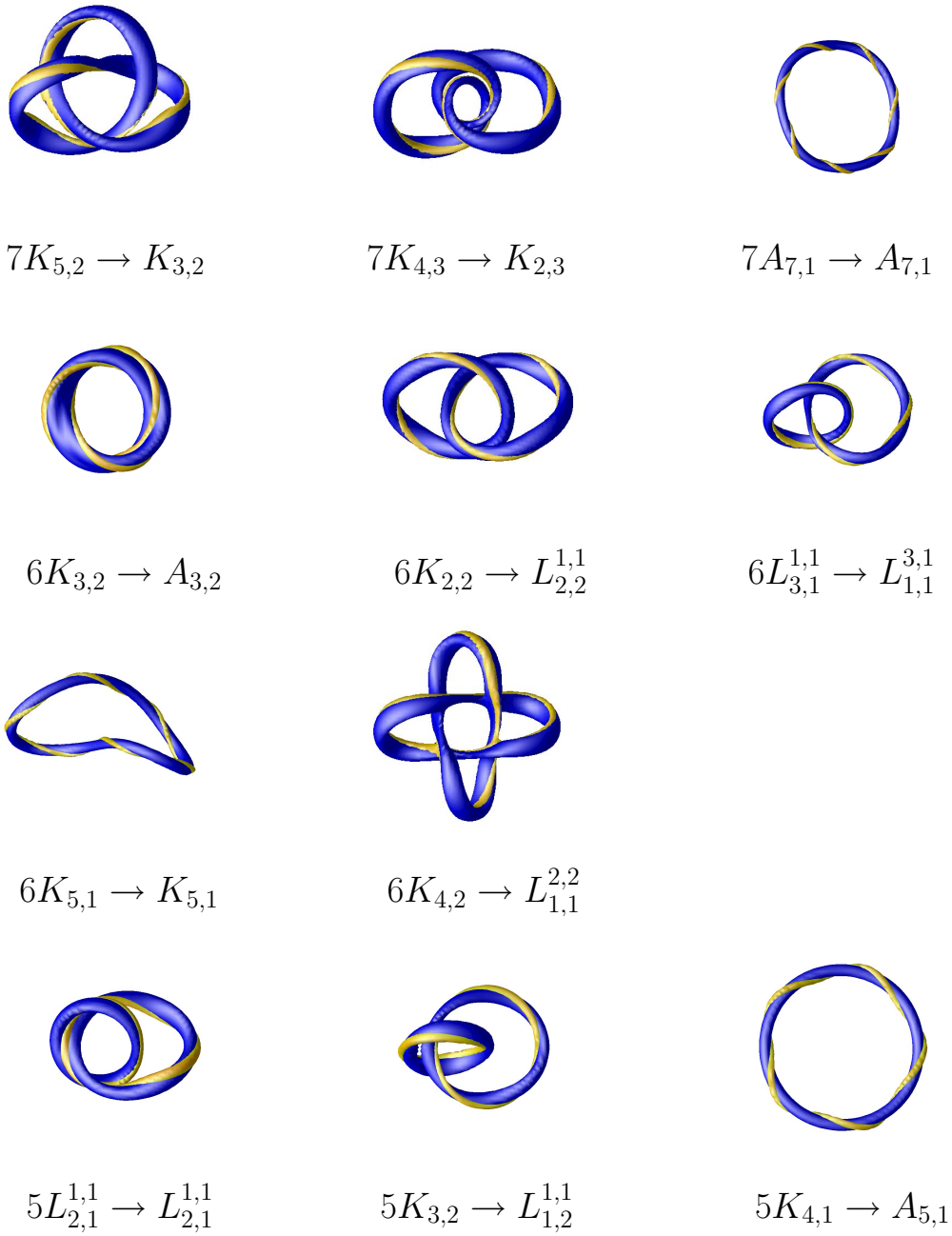

Figure 5.5: Minimum energies for $m = 5$ Hopfions of charge $5 \leq Q \leq 7$. The most top left plot represents the lowest energy solutions for each topological charge.

One main difference between our results and those of [51] is that we are presenting potentially new energetic local minimum or saddle point solutions. As shown in Figure 5.6 we have new linked topological charges $Q = 8, 12, 15$ excited solutions.

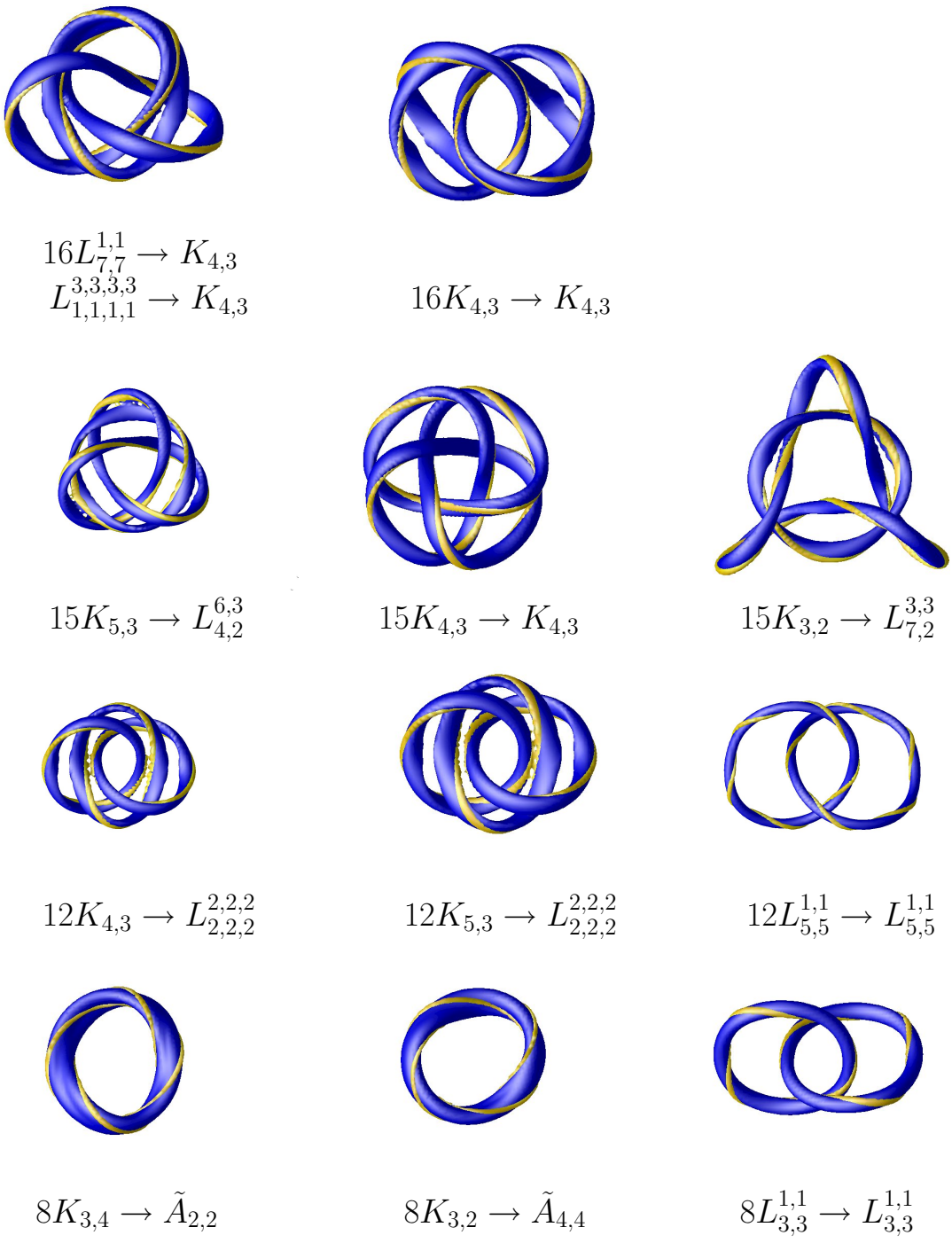

Figure 5.6: Minimum energies for $m = 5$ Hopfions of charge $Q = (8, 12, 15, 16)$. The most left plot represents the lowest energy solutions for each topological charge.

Also our topological charge eight and six minimum energy solutions seem to have the same linking structure as in the $m = 0$ case. But in the $m = 5$ case the links

	E	$E/Q^{3/4}$
$Q=4$		
$K_{2,1} \to \tilde{A}_{4,1}$	6.05	2.14
$K_{4,1} \to \tilde{A}_{4,1}$	6.05	2.14
$A_{4,1} \to A_{4,1}$	6.07	2.15
$A_{2,2} \to A_{2,2}$	6.09	2.15
$L^{1,1}_{1,1} \to L^{1,1}_{1,1}$	7.17	2.53
$Q=5$		
$L^{1,1}_{2,1} \to L^{1,1}_{1,2}$	6.23	1.86
$K_{3,2} \to L^{1,1}_{1,2}$	7.17	2.14
$K_{4,1} \to A_{5,1}$	7.43	2.22
$Q=6$		
$K_{3,2} \to A_{3,2}$	8.01	2.09
$K_{2,2} \to L^{1,1}_{2,2}$	8.19	2.14
$L^{1,1}_{3,1} \to L^{1,1}_{3,1}$	8.41	2.19
$K_{5,1} \to K_{5,1}$	8.60	2.24
$K_{4,2} \to L^{2,2}_{1,1}$	9.07	2.37
$Q=7$		
$K_{5,2} \to K_{3,2}$	9.19	2.14
$K_{3,2} \to K_{3,2}$	9.20	2.14
$K_{4,3} \to K_{2,3}$	9.64	2.24
$A_{7,1} \to A_{7,1}$	10.18	2.37
$Q=8$		
$L^{2,2}_{2,2} \to \tilde{A}_{4,2}$	9.86	2.07
$K_{3,2} \to A_{4,2}$	9.88	2.08
$K_{3,4} \to \tilde{A}_{4,2}$	9.88	2.08
$K_{5,2} \to A_{4,2}$	9.97	2.10
$L^{1,1}_{3,3} \to L^{1,1}_{3,3}$	10.45	2.20
$Q=12$		
$K_{4,3} \to L^{2,2,2}_{2,2,2}$	13.77	2.16
$K_{5,3} \to L^{2,2,2}_{2,2,2}$	13.77	2.16
$L^{1,1}_{5,5} \to L^{1,1}_{5,5}$	15.30	2.37
$Q=15$		
$K_{5,3} \to L^{6,3}_{4,2}$	16.17	2.12
$K_{4,3} \to K_{4,3}$	16.56	2.17
$K_{3,2} \to L^{3,3}_{7,2}$	17.11	2.25
$Q=16$		
$L^{3,3,3,3}_{1,1,1,1} \to \tilde{K}_{4,3}$	17.07	2.13
$K_{4,3} \to K_{4,3}$	17.12	2.14
$K_{3,2} \to K_{4,3}$	17.25	2.17

Table 5.2: Table of initial configurations and final configurations form and energy. For $m = 5$ Hopfions.

seem to be almost on top of each other. The minimum energy location curve of the topological charge 15 Hopfion is topologically similar to that found in [51]; but it is qualitatively different.

Figure 5.7 shows how the energy grows with increasing charge.

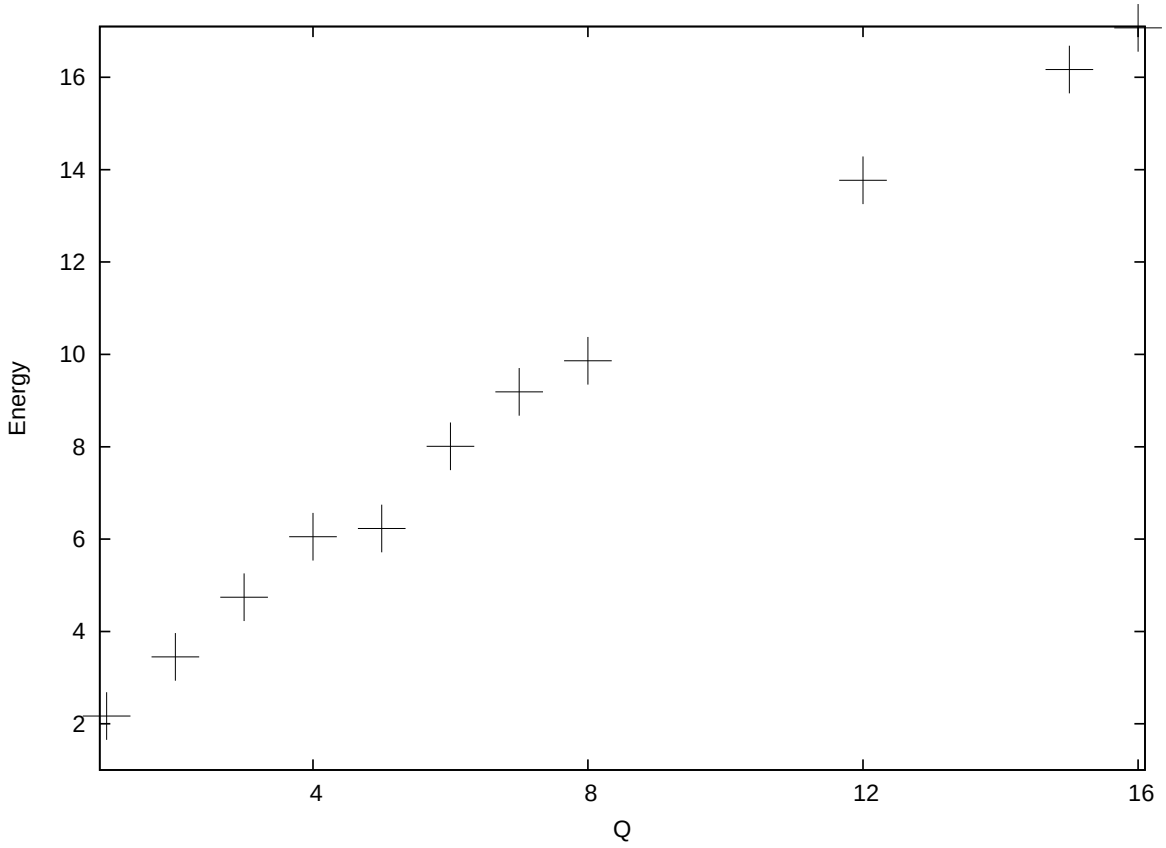

Figure 5.7: Minimum energies for $m = 5$ Hopfions. As a function of topological charge Q.

5.5 Infinite mass, $m \to \infty$.

Rescaling the Lagrangian density (5.2.1) by $\boldsymbol{x} \mapsto \sqrt{m}\boldsymbol{x}$ gives

$$\frac{\mathcal{L}(\sqrt{m}\boldsymbol{x})}{\sqrt{m}} = \frac{\mathcal{L}_2}{m} + \mathcal{L}_4 + \mathcal{L}_0.$$

Where $\mathcal{L}_a$ refers to the a^{th} order derivative in the Lagrangian density. We can then define

$$\mathcal{L}_{m\to\infty} = \lim_{m\to\infty} \frac{\mathcal{L}(\sqrt{m}\boldsymbol{x})}{\sqrt{m}} = \mathcal{L}_4 + \mathcal{L}_0. \tag{5.5.1}$$

This rescaling gives a model which can be interpreted as a Skyrme-Faddeev model which has an infinite coupling to a potential term. A model comprising only of a Skyrme term and a potential term has been addressed before [63]. In [63] this model was derived by setting a constant to zero. This effectively removes the sigma term in the Skyrme-Faddeev coupled to a potential model. Soliton solutions of this model are commonly refereed to as compactons [63]. This is because they reach their vacuum value in finite distance and therefore have no asymptotic tails. Hence they are effectively BPS for large separation. This compact nature of the minimum energy solutions gives a stronger correspondence with the string ansatz, which assumes no self interaction of the Hopfion loop. Also the string ansatz is derived by assuming the Hopfion is a compacton. In order to numerically find minimum energy solutions of (5.5.1) it is computationally easier to work with a modified model of the form

$$\mathcal{L}_{\text{Modified}} = \frac{\partial_0\boldsymbol{\phi}\cdot\partial_0\boldsymbol{\phi}}{32\pi^2\sqrt{2}} + \mathcal{L}_{m\to\infty}|_{\partial_t\boldsymbol{\phi}=0}. \tag{5.5.2}$$

This modified model can be simulated by a trivial extension of the previous Skyrme-Faddeev model. The equation of motion and the energy density of (5.5.2) will converge with the infinite mass case, (5.5.1), in the static limit. This model, (5.5.2), also allows for time evolution, by the second order dynamics of the purely kinetic sigma term. Again we use the rational map ansatz, (5.4.5), to give non-trivial knotted initial

conditions. For this infinite mass compacton model, (5.5.1), we find the topological charge-specific minimum energy candidates in Table 5.3. The numerical scheme is fundamentally the same as the one used in the finite mass case. But now due to this model having a different scale we found $\Delta x = 0.1$ to be a suitable lattice spacing. The results and initial conditions of this investigation are shown in Table 5.3. Also, for topological charge $1 \leqslant Q \leqslant 5$ the Hopfion location curves are shown in Figure 5.8. We find, in this infinite mass model, that the minimum energy solutions, for $1 \leqslant Q \leqslant 5$, are the same as the $m = 5$ and $m = 0$ models. The compact nature of this model can be seen in Figure 5.9; which show ϕ_3 along a radius that is in the same plane as the planar, $Q = 1$, Hopfion. This shows how the compact Hopfion field attains the vacuum value in finite distance. This shows that in the $m = \infty$ model two well-separated static Hopfions do not attract or repel each other. This is due to there being no overlap of the Hopfion tails. Therefore, the string self-interaction of this $m = \infty$ model is much less than in the finite mass model. Also the shape of ϕ_3, in Figure 5.9, is more symmetric about its minimum than the plots of ϕ_3 in the finite mass model, Figure 5.3. This shows that in the $m = \infty$ limit the string cross-section is much more symmetric. Again, in this infinite mass case, we have found new local minimum energy solutions for $Q = 4$; both of which have location curves described as a very twisted $A_{4,1}$. A point worth noting is that for these solutions the boundary of the numerical lattice is very far from the Hopfion.

	E	$E/Q^{3/4}$
$Q = 1$		
$A_{1,1} \to A_{1,1}$	0.86	0.86
$Q = 2$		
$A_{2,1} \to A_{2,1}$	1.37	0.82
$Q = 3$		
$K_{2,1} \to \tilde{A}_{3,1}$	1.90	0.83
$A_{3,1} \to A_{3,1}$	2.02	0.90
$Q = 4$		
$A_{2,2} \to A_{2,2}$	2.50	0.88
$A_{4,1} \to A_{4,1}$	2.56	0.91
$K_{2,1} \to \tilde{A}_{4,1}$	3.19	1.13
$L^{1,1}_{1,1} \to L^{1,1}_{1,1}$	3.38	1.20 (not shown)
$K_{4,1} \to A_{4,1}$	4.22	1.50
$Q = 5$		
$L^{1,1}_{2,1} \to L^{1,1}_{2,1}$	3.00	0.90
$A_{5,1} \to A_{5,1}$,	3.23	0.97
$K_{3,2} \to K_{3,2}$	3.88	1.16
$Q = 7$		
$k_{3,2} \to K_{3,2}$	3.97	0.92

Table 5.3: Table of the infinite mass Hopfions initial and final configurations, with their respective energies.

Table 5.3 shows that in this $m = \infty$ model the initial and final minimised location curves rarely differ. A good example of this is the $Q = 5$ $K_{3,2}$ trefoil knot; under minimization in this model it remains as a $K_{3,2}$ trefoil knot, but in the $m = 5$ and $m = 0$ models it minimises to a $L^{1,1}_{2,1}$. The $Q = 5$, $L^{1,1}_{2,1}$, is also a lower energy solution for this charge in the $m = \infty$ model. This reluctance to deform from one location curve to another is due to the reduced self interaction of this compact Hopfion model.

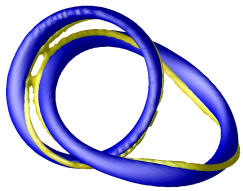

$5L^{1,1}_{2,1} \to L^{1,1}_{2,1}$

$5A_{5,1} \to A_{5,1}$

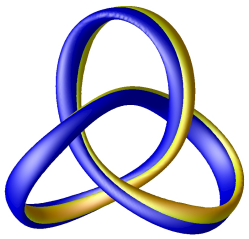

$5K_{3,2} \to K_{3,2}$

$4A_{2,2} \to A_{2,2}$

$4A_{4,1} \to A_{4,1}$

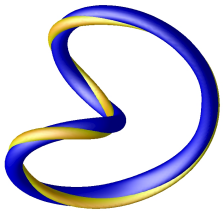

$4K_{2,1} \to \tilde{A}_{4,1}$

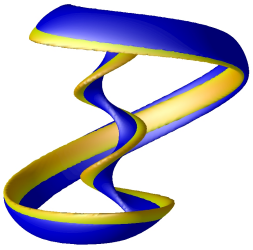

$4K_{4,1} \to \tilde{A}_{4,1}$

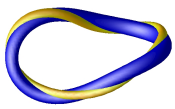

$3K_{2,1} \to \tilde{A}_{3,1}$

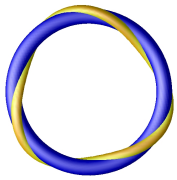

$3A_{3,1} \to A_{3,1}$

$2A_{2,1} \to A_{2,1}$

$1A_{1,1} \to A_{1,1}$

Figure 5.8: Minimum energy solutions for $m = \infty$. For topological charges $1 \leqslant Q \leqslant 5$. The upper most left plot represents the lowest energy solutions for each topological charge sector.

We have also found a topological charge seven trefoil knot, in the $m = \infty$ model, which is shown in Figure 5.10. For the range of topological charges we

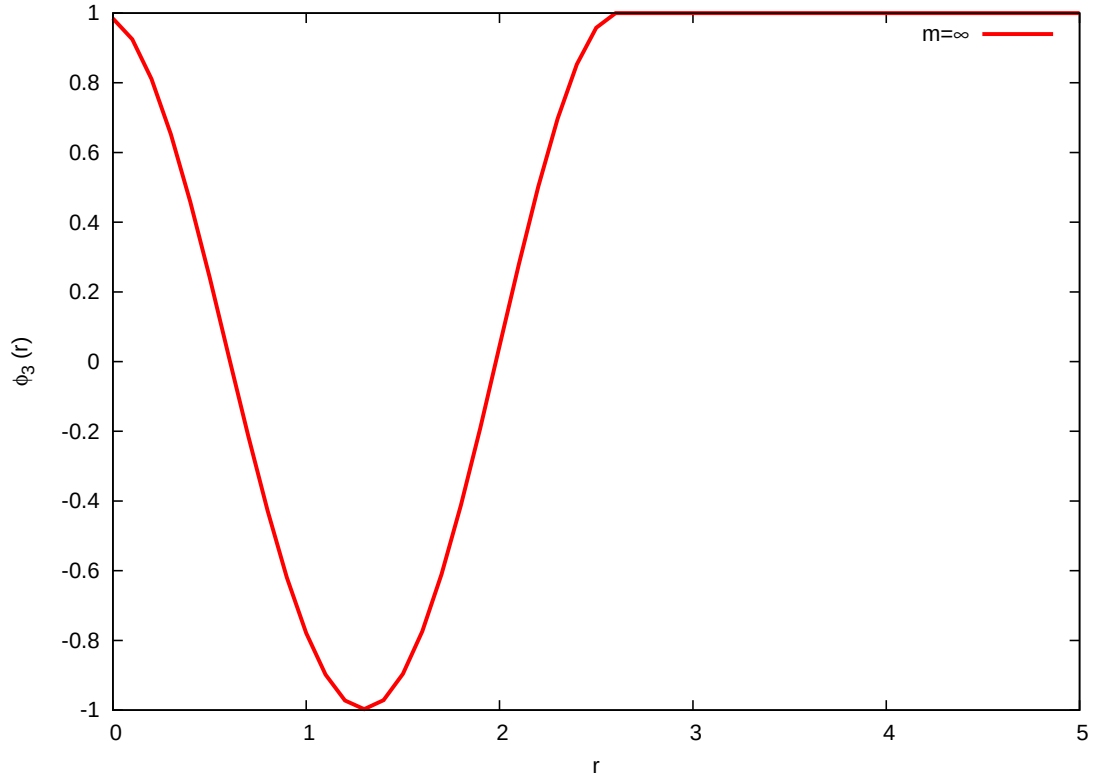

Figure 5.9: ϕ_3 along a radius of a $Q = 1$ Hopfion in the infinite mass case.

have investigated, in this $m = \infty$ model, we have found that the charge-specific lowest energy solutions are the same as in the $m = 0$ and $m = 5$ models. But as in the $m = 5$ model we have discovered more local minima or saddle point solutions.

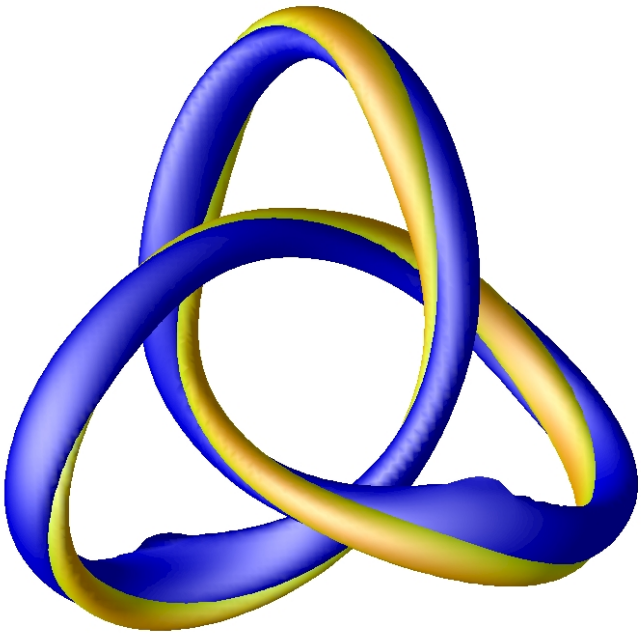

Figure 5.10: The $Q = 7$ trefoil knot minimum energy solution for the $m = \infty$ Skyrme-Faddeev model plus a potential.

5.6 Conclusion.

In this chapter we explored the Skyrme-Faddeev model with a potential term included. We found that including a potential in the model makes the Hopf solitons exponentially decay to their vacuum value. Increasing the coupling makes the Hopf solitons string cross-section increasingly exponentially localized. We found for $m = 5$ the minimum energy solutions are described by the same linking curves as the, $m = 0$, Skyrme-Faddeev model. Using a spatial rescaling we were able to formulate an infinite mass model. This infinite mass model is known to yield compact Hopfions [63]. For this infinite mass, compact, model we have presented a number of topologically charged solutions. We showed that the minimum energy compact solutions have the same location curves as in the usual, $m = 0$, Skyrme-Faddeev model and the $m = 5$, massive, model. In both $m = 5$ and $m = \infty$ models we found new local minimum, or

stationary point energetic solutions. The increasing localization of the strings in the two massive models reduces the string self interaction. Therefore, it is not surprising that these models possess solutions stabilised by symmetry. This chapter contains my results which complement an ongoing collaboration, which is concerned with creating a synthetic Hopfion ansatz. The infinite mass compact Hopfion model is especially applicable to this ansatz. There has been some recent success in predicting the energy and radius of the $Q = 1, 2, 3$ solutions, of this infinite mass model, using the string ansatz.

Bibliography

[1] D. Foster and P. Sutcliffe, *Phys. Rev.* **D79**, 125026 (2009).

[2] P. Bowcock, D. Foster and P.M. Sutcliffe, *J. Phys.* **A42**, 085403 (2009).

[3] D. Foster,*Nonlinearity* **23**, 465 (2010).

[4] S. Coleman, *Nucl. Phys.* **B262**, 263 (1985).

[5] P. A. M. Dirac, *Proc. Roy. Soc.* **A133**, 60 (1931).

[6] X. Z. Yu et al, *Nature* **465**, 901 (2010).

[7] T.H.R Skyrme, *Proc. R. Soc. Lond.* **A133**, 60 (1931).

[8] E. Witten, *Nucl. Phys.* **B223**, 433 (1983).

[9] R.A.Battye and P.M. Sutcliffe, *Rev. Math. Phys.* **14**, 29 (2002).

[10] M. J. Esteban, *Commun. Math. Phys.* **105**, 571 (1986).

[11] A.D. Jackson and M. Rho, *Phys. Rev. Lett.* **51**, 751 (1983).

[12] B. J. Schroers, *Z. Phys.* **C61**, 479 (1994).

[13] R. A. Battye, N. S. Manton, P. M. Sutcliffe and S. W. Wood, *Phys. Rev.* **C80**, 034323 (2009).

[14] M.F. Atiyah and N.S. Manton, *Phys. Lett.* **B222**, 438 (1989).

[15] M.F. Atiyah and N.S. Manton, *Commun. Math. Phys.* **153**, 391 (1993).

[16] N.S. Manton, *Commun. Math. Phys.* **111**, 469 (1987).

[17] R.A. Battye, N.S. Manton and P.M. Sutcliffe, *Proc. Roy. Soc.* **A463**, 261 (2007).

[18] C. Barnes, K. Baskerville and N. Turok, *Phys. Rev. Lett.* **79**, 367 (1997).

[19] C. Barnes, K. Baskerville and N. Turok, *Phys. Lett.* **B411**, 180 (1997).

[20] C.J. Houghton, N.S. Manton and P.M. Sutcliffe, *Nucl. Phys.* **B510**, 507 (1998).

[21] G.H. Derrick, *J. Math. Phys.* **5**, 1252 (1964).

[22] Alexander Kusenko, *Nucl.Phys.Proc. Suppl.* **62A-C**, 248 (1998).

[23] Alexander Kusenko. 'Cosmology of SUSY Q-balls.' arXiv:hep-ph/0001173v1, (2000).

[24] A. Kusenko and M. Shaposhnikov, *Phys.Lett.* **B418**, 46 (1998).

[25] M.Gleiser, J.Thorarinson, *Phys.Rev.* **D73**, 065008 (2006).

[26] R. Friedberg, T.D. Lee and A.Sirlin, *Phys. Rev.* **D13**, 2739 (1976).

[27] T.D. Lee, Y. Pang, *Phys. Rept.* **221**, 251 (1992).

[28] M. Tsumagari, E.J. Copeland and P.M. Saffin *Phys. Rev.* **D78**, 065021 (2008).

[29] P.Bowcock, G.Tzamtzis, *JHEP* **03-047** (2007).

[30] B.S.Getmanov, *Theor.Math.Phys.* **48**, 572 (1982).

[31] B.S.Getmanov, *Pisma Zh.Eksp.Teor.Fiz.* **25**, 132 (1977).

[32] J.L. Miramontes, *Nucl. Phys.* **B702**, 419 (2004).

[33] R.A Battye and P.M Sutcliffe, *Nucl. Phys.* **B590**, 329 (2000).

[34] M. Axenides, et al. *Phys.Rev.* **D61**,085006 (2000).

[35] Y.Brihaye, B.Hartmann, *Nonlinearity* **21**, 1937 (2008).

[36] *Bäcklund and Darboux Transformations.* C. Rogers, W. K. Schief. Cambridge University Press. 2002.

[37] Q-Han Park and H.j. Shin, *Phys. Letts.* **B359**, 125 (1995).

[38] B.M.A.G. Piette, B.J. Schroers and W.J. Zakrzewski, *Z. Phys.* **C65**, 165 (1995)

[39] S.L. Sondhi, A. Karlheda, S.A. Kivelson and E.H. Rezayi, *Phys. Rev.* **B47**, 16419 (1993).

[40] T. Weidig, *Nonlinearity* **12**, 1489 (1999).

[41] P.E. Eslami, M. Sarbishaei and W.J. Zakrzewski, *Nonlinearity* **13**, 1876 (2000)

[42] I. Hen and M. Karliner, *Phys.Rev.* **D77**, 054009 (2008).

[43] D. Harland and R.S. Ward, *Phys. Rev.* **D77**, 045009 (2007).

[44] I. Hen and M. Karliner, *Phys.Rev.* **D77**, 054009 (2008).

[45] R.A. Battye and P.M. Sutcliffe, *Phys. Lett.* **B416**, 385 (1998).

[46] R.A. Battye, N.S. Manton and P.M. Sutcliffe, *Proc.Roy.Soc.* **463**, 261 (2007)

[47] G.S. Adkins and C.R. Nappi, *Phys.Letts.* **B137**, 251 (1984).

[48] P.M. Sutcliffe, *Phys. Rev.* **D79**, 085014 (2009).

[49] R. S. Palais, *Commun. Math. Phys.* **69**, 19 (1979).

[50] R.A. Battye and P.M. Sutcliffe, *Phys. Rev. Letts.* **88**, 22 (1998).

[51] P.M. Sutcliffe, *Proc. Roy. Soc.* **A 463**, 3001 (2007).

[52] R.S. Ward, *Phys. Lett.* **B473**, 291 (2000)

[53] J. Hietarinta and P. Salo, *Phys. Rev.* **D62**, 081701(R) (2000).

[54] L. Faddeev and A.J. Niemi, *Nature* **58**, 387 (1997).

[55] *Geometry, Topology and Physics.* M. Nacahara. Adam Hilger (1990).

[56] *Graduate Texts in Mathematics Differential Forms in Algebraic Topology.* R. Bott and L.W. Tu. Springer-Verlag (1995).

[57] R.S. Ward, *Nonlinearity* **12**, 241 (1999).

[58] F. Lin and Y. Yang, *Commun. Math. Phys.* **249**, 273 (2004).

[59] A. Kundu and Y. P. Rybakov, *J. Phys.* **A15**, 269 (1982).

[60] R.S. Ward, *J.Phys.* **A39**, 105 (2006).

[61] J. Gladikowski and M. Hellmund, *Phys. Rev.* **D56**, 5194 (1997).

[62] E. Brieskorn and H. Knörrer, *Plane Algebraic Curves.* Birkhäuser Verlag (1986).

[63] C. Adam and J. Sanchez-Guillen, *J.Phys.* **A43**, 345402 (2010).

[64] *Topological Solitons*, N. Manton and P. Sutcliffe, Cambridge University press (2004).

[65] B.M.A.G. Piette, B.J. Schroers and W.J. Zakrzewski, *Z. Phys.* **C65**, 165 (1995).

[66] P.M. Sutcliffe, *Phys. Rev.* **D79**, 085014 (2009).

[67] P.M. Sutcliffe, *Proc. Roy. Soc.* **463**, 3001 (2007).